DNA 2825F

Final Report

December 1971

CORRELATION OF RADAR ECHOES FROM THE AURORA WITH SATELLITE-MEASURED AURORAL PARTICLE PRECIPITATION

By: W. G. CHESNUT J. C. HODGES R. L. LEADABRAND

Prepared for:

DEFENSE NUCLEAR AGENCY
WASHINGTON, D.C. 20301

CONTRACT DASA01-67-C-0066

STANFORD RESEARCH INSTITUTE
Menlo Park, California 94025 · U.S.A.

UNCLASSIFIED

Security Classification

DOCUMENT CONTROL DATA - R & D

Security classification of title, body of abstract and indexing annotation must be entered when the overall report is classified)

1 ORIGINATING ACTIVITY (Corporate author)	2a. REPORT SECURITY CLASSIFICATION
Stanford Research Institute Menlo Park, California 94025	Unclassified
	2b. GROUP N/A

3 REPORT TITLE

CORRELATION OF RADAR ECHOES FROM THE AURORA WITH SATELLITE-MEASURED AURORAL PARTICLE PRECIPITATION

4. DESCRIPTIVE NOTES (Type of report and inclusive dates)

Final Report Covering the period March 1969 to December 1971

5 AUTHOR(S) (First name, middle initial, last name)

Walter G. Chesnut James C. Hodges Ray L. Leadabrand

6 REPORT DATE	7a. TOTAL NO OF PAGES	7b. NO OF REFS
December 1971	172	11

8a CONTRACT OR GRANT NO	9a. ORIGINATOR'S REPORT NUMBER(S)
Contract DASA-01-67-C-0066	Final Report SRI Project 6548
b. PROJECT NO. NWET K11BAXH	
c. Task and Subtask X532	9b. OTHER REPORT NO(S) (Any other numbers that may be assigned this report)
d. Work Order 01	DNA 2825F

10. DISTRIBUTION STATEMENT

Approved for public release; distribution unlimited.

11 SUPPLEMENTARY NOTES	12 SPONSORING MILITARY ACTIVITY
	Defense Nuclear Agency Washington, D.C.

13 ABSTRACT

The characteristics of auroral particle precipitation as measured during 14 passes by the Lockheed OV1-18 satellite over Alaska have been compared with radar aurora simultaneously detected at 139 and 398 MHz beneath the satellite orbit. The radar aurora were measured using the SRI auroral radar located at Homer in southern Alaska. The satellite measured precipitation of protons with energies above 10 keV and precipitation of electrons with energies above 800 eV. All measurements were made near local midnight while the E-region was in darkness. The study has revealed the following:

(1) Protons with energies above 10 keV regularly precipitate to the south of electrons with energies above 800 eV.

(2) Electron precipitation in regions of radar aurora seems sufficiently intense to produce the E-region ionization needed to explain the observed radar scattering.

(3) Radar aurora (on 11 of 14 passes) was not associated with regions of intense proton precipitation.

(4) No obvious relationship existed between regions of radar aurora and regions of most intense flux of electron precipitation power (number flux times average electron energy), though there may be a tendency for these to be spatially anticorrelated.

(5) There seems to be a tendency for the electrons incident into regions of radar aurora to have a slightly lower average energy (order of 80%) than electrons precipitating elsewhere.

DD FORM 1 NOV 68 1473 (PAGE 1)

S/N 0101-807-6801

UNCLASSIFIED

Security Classification

14 KEY WORDS	LINK A		LINK B		LINK C	
	ROLE	WT	ROLE	WT	ROLE	WT
Aurora						
Aurora correlation						
Auroral radar						
Satellite-measured auroral precipitation						

Item 13 ABSTRACT (continued)

(6) There is a tendency for the average electron precipitation power to be less in regions of radar aurora than in other precipitation regions.

There does not seem to be a deterministic relationship between the character of precipitating electrons and radar aurora--only subtle, statistical tendencies were found.

STANFORD RESEARCH INSTITUTE
Menlo Park, California 94025 · U.S.A.

Final Report

DNA 2825F

December 1971

CORRELATION OF RADAR ECHOES FROM THE AURORA WITH SATELLITE-MEASURED AURORAL PARTICLE PRECIPITATION

By: W. G. CHESNUT J. C. HODGES R. L. LEADABRAND

Prepared for:

DEFENSE NUCLEAR AGENCY
WASHINGTON, D.C. 20301

CONTRACT DASA01-67-C-0066

This work sponsored by the Defense Nuclear Agency under NWET Subtask K11BAXHX532.

SRI Project 6548

Approved by:

DAVID A. JOHNSON, *Director*
Radio Physics Laboratory

RAY L. LEADABRAND, *Executive Director*
Electronics and Radio Sciences Division

Copy No. .....5.

ABSTRACT

The characteristics of auroral particle precipitation as measured during 14 passes by the Lockheed OV1-18 satellite over Alaska have been compared with radar aurora simultaneously detected at 139 and 398 MHz beneath the satellite orbit. The radar aurora were measured using the SRI auroral radar located at Homer in southern Alaska. The satellite measured precipitation of protons with energies above 10 keV and precipitation of electrons with energies above 800 eV. All measurements were made near local midnight while the E-region was in darkness. The study has revealed the following:

(1) Protons with energies above 10 keV regularly precipitate to the south of electrons with energies above 800 eV.

(2) Electron precipitation in regions of radar aurora seems sufficiently intense to produce the E-region ionization needed to explain the observed radar scattering.

(3) Radar aurora (on 11 of 14 passes) was <u>not</u> associated with regions of intense proton precipitation.

(4) No obvious relationship existed between regions of radar aurora and regions of most intense flux of electron precipitation power (number flux times average electron energy), though there may be a tendency for these to be spatially anticorrelated.

(5) There seems to be a tendency for the electrons incident into regions of radar aurora to have a slightly lower average energy (order of 80%) than electrons precipitating elsewhere.

(6) There is a tendency for the average electron precipitation power to be less in regions of radar aurora than in other precipitation regions.

There does not seem to be a deterministic relationship between the character of precipitating electrons and radar aurora--only subtle, statistical tendencies were found.

CONTENTS

ILLUSTRATIONS

TABLES

ACKNOWLEDGMENTS

We wish to thank Mr. Ronald Presnell of our Laboratory for the assistance provided to this program in a number of ways. In particular, Mr. Presnell has continued to modernize the Homer radar system and has provided guidance on the operation of the instrument.

Miss Judy Moore provided computer programming necessary for the reduction and presentation of the satellite data as it is found in this report.

Dr. Richard Sharp and Dr. Richard Johnson of the Lockheed Space Sciences Laboratory of Palo Alto, California, furnished the satellite electron and proton precipitation data. We appreciate their guidance and suggestions concerning the use of their data.

We appreciate the continued guidance and interest shown by Mr. Dow Evelyn of the Defense Nuclear Agency.

The Geophysical Institute, College, Alaska, furnished all-sky photographs. The U.S. Coast and Geodetic Survey, College, Alaska, furnished magnetograms.

The 1969 Radar Data Collection Program was supported both by the Defense Nuclear Agency and by the National Science Foundation (Grant GA-1061).

1. INTRODUCTION

This report describes the research performed by the Radio Physics Laboratory of Stanford Research Institute for the Defense Nuclear Agency on Contract DASA01-67-C-0066. The program compares Alaskan auroral radar echoes with the OVI-18 satellite data gathered by Lockheed Space Sciences Laboratory.

The experiment is referred to as an input-output experiment. The input to the ionosphere is measured by the satellite, and the resulting effects (the output) are simultaneously measured by the Homer radar. The program is a continuation of work started in 1965 under DNA sponsorship.[1]* The earlier experiment produced only one pass during which radar aurora were present before the satellite orbit decayed.

The data used in this report were obtained under DNA sponsorship between 24 March 1969 and 8 May 1969, and under NSF sponsorship from 3 September to 17 October 1969. These periods were near the maximum of the 11-year solar sunspot activity cycle. The data from 14 of approximately 60 satellite passes were made available for SRI by Lockheed late in March 1971. Five hours of magnetic data supplied by the Coast and Geodetic Survey, College, Alaska, and five days of all-sky-camera data furnished by the Geophysical Institute of the University of Alaska are correlated with radar data in this report.

Although radar echoes have been observed from the aurora for approximately 20 years the mechanism that produces these radar echoes is still

*References are listed at the end of the report.

not well understood. Earlier studies of radar data correlation with other radio data, visual data, magnetic-field-fluctuation data, and data from other geophysical phenomena have not always shown clear-cut relationships. In particular, comparisons of visual aurora and radar aurora have shown that the radar aurora is usually much broader geographically and usually occupies a somewhat different position in space than the visual aurora.[2]

Correlating satellite-measured particle precipitation with radar aurora seems to be a fruitful technique to better investigate the underlying physics. The OV1-18 satellite that was used in this experiment measured electron and proton precipitation at an altitude of 500 km over Alaska. The Homer radar collected data magnetically below the satellite during the time of the pass.

A report comparing precipitation during one daytime pass with radar echoes obtained at 1300 MHz by the Millstone Hill radar has been reported by Hagfors et al.[3] Their comparison also used the OV1-18 satellite. For this one daytime pass they find that the radar aurora was located in a region of proton precipitation. We find, and shall show later, that on the night side radar aurora and proton precipitation tend to take place at different latitudes.

This report is organized as follows. Section 2 discusses the experiment geometry. The geometrical constraints on collection of radar data and the geometric considerations relevant to radar/satellite comparisons are presented.

Section 3 describes the characteristics of the Homer radar in sufficient detail to understand this report. The characteristics of the counters that were carried on the OV1-18 satellite are also described. Section 3 also describes the operation of the equipment and the data-collecting schedule.

Section 4 is a data compilation of satellite and radar data for 14 satellite passes for which satellite particle-counter measurements were provided to SRI by the Lockheed Corporation. The correlations that are made have to do with the spatial location of radar and precipitating particles.

Section 5 provides a comparison of some of our radar data with magnetometer measurements made underneath the radar auroral scattering. Section 5 also presents a comparison of the geometry of visual auroral arcs with radar aurora obtained at the same time.

Section 6 is a study of the satellite data and correlations made between the satellite and radar data in an attempt to understand the nature of the phenomena that are being observed. In particular, we concern ourselves with production of ionization in the nighttime E-region, since this ionization is necessary for the existence of radar scattering. We also concern ourselves with the location of radar aurora and the character of the particle precipitation.

Section 7 presents the conclusions that have been reached as a result of this research effort.

Section 8 indicates additional work that should be done in order to better understand the data that have already been collected.

2. EXPERIMENT GEOMETRY

A variety of geometric considerations affect the interpretation of the data correlations covered in this report. In this section we describe some of these constraints so that the reader can view our data in better perspective.

2.1 Geometry Constraints on Radar Data

As is well known, radar aurora is only obtained when the radar beam line is nearly perpendicular to the earth's magnetic field in the scattering volume. The signal strength depends on the magnetic aspect angle; this angle is the difference between the angle exactly perpendicular to the magnetic field and the actual angle between the radar beam line. The Homer radar was located in order that this magnetic geometry constraint could permit as wide a coverage of radar aurora over the state of Alaska as possible. Figure 2.1* presents a plot of the magnetic aspect angle for aurora scattering at an altitude of 110 km as observed from the Homer radar site. Homer is located near the bottom of the map. As a practical matter, radar auroras are usually detectable only when they occur within the 3° contour shown in Figure 2.1.

Figure 2.2 presents an elevation view, which is another way to demonstrate the magnetic geometry. This view shows that the 0° magnetic aspect angle is a function of altitude when the radar views directly North.

Figure 2.3 presents a map of Alaska showing the 3° magnetic aspect angle as seen from the Homer radar site for scattering at 110 km

---

*Figures are grouped at the end of each major section.

altitude. Also shown on the map is the area covered by an all-sky camera located at Fairbanks. The figure shows overlapping coverage. Another all-sky camera, located at Ft. Yukon, extends photographic coverage another 200 km north.

Figure 2.3 presents in a qualitative way the area of Alaska and Canada that can be surveyed by the Homer radar in a practical sense. During very strong radar auroras, echoes can be obtained from outside this contour, but such reception is rare.

2.2 Geometric Constraints on Satellite Data

Figure 2.4 shows the way in which satellite precipitation data were geometrically related to the radar data. This figure represents an elevation view along a meridian through Homer and College, Alaska. The figure shows various magnetic field lines. We show schematically how satellite measurements of precipitation are projected down magnetic field lines to the earth's surface. The radar aurora are also projected down magnetic field lines to the earth's surface. Therefore, comparisons that will be seen later will be between precipitation and radar aurora as both are projected to the earth's surface.

There are three other geometry considerations concerning satellite data that must be borne in mind. First, we project electron-precipitation effects to the earth's surface as described by Figure 2.4. In fact, ionization will be produced along magnetic field lines where the electrons are precipitating. Therefore, there will be a real, geometrical relationship in the radar scattering region, between electrons and radar aurora. This is not the case for protons. Satellite-measured proton precipitation is made at altitudes above 400 kilometers. Protons that precipitate to lower altitudes where the atmosphere is more dense will suffer charge exchange. As a result, a very localized proton flux at

satellite altitude may be spatially spread by several hundred kilometers by the time the protons reach altitudes between 100 and 110 kilometers. Therefore, relationships between regions of peak proton precipitation, as measured by the satellite, and regions of radar aurora do not necessarily relate to overlap of E-region ionization produced by the protons. The relationship, if one does exist, is then between the mechanism that causes proton dumping and that which causes spatial structuring of E-region ionization that leads to radar aurora.

There is a third geometry consideration regarding correlations between radar aurora and precipitation. This relationship has to do with the production of the E-region ionization that is necessary for radar aurora. Since radar aurora most often occurs at an altitude on the order of 110 kilometers, precipitating particles must have sufficiently high energy to penetrate to this altitude if they are going to contribute to the E-region ionization.

2.3 Simultaneity of Radar and Satellite Measurements

When we perform correlation studies between radar aurora and satellite precipitation, it is essential, of course, that the measurements be made at the same time. Since radar aurora can move large distances in a time of several tens of seconds, one surmises that the simultaneity accuracy ought to be within 10 or 20 seconds. Pre-pass ephemeris data were used in our analyses. Pre-pass ephemeris data was sometimes in error. Four cases were particularly poor in their simultaneity. These four cases were passes A388, A431, A513, and A641. The simultaneity for the last two cases was in error by 7 and 15 minutes, respectively.

Satellite precipitation data are output and recorded once per second. During this time period the satellite moves about 7-1/2 km.

Satellite data are referenced to "satellite times." The post-pass satellite ephemeris is also related to this time. It is therefore very important that the ephemeris geographical error be less than this; otherwise our radar/satellite comparisons will not spatially overlap properly. We assume Lockheed data are this accurate.

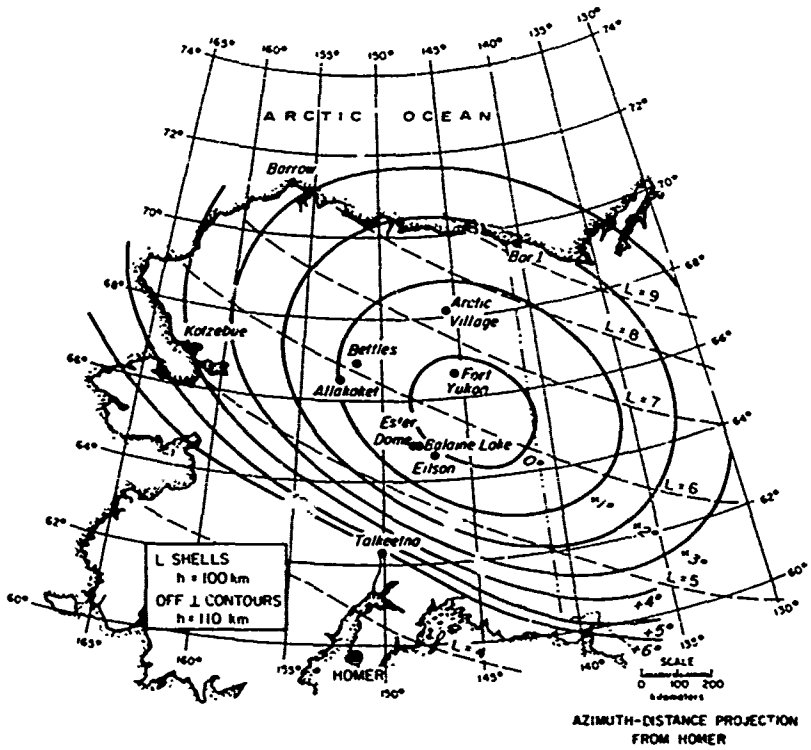

FIGURE 2.1 MAP OF ALASKA SHOWING MAGNETIC-ASPECT ANGLES FOR THE HOMER RADAR MAGNETIC L SHELLS

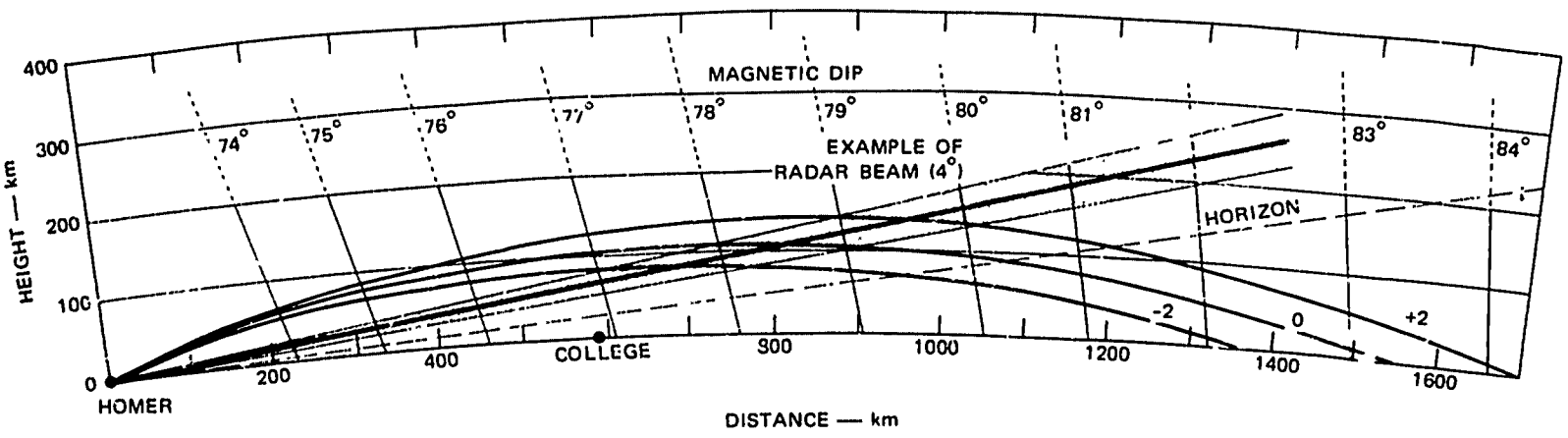

FIGURE 2.2 ELEVATION VIEW OF MAGNETIC GEOMETRY IN PLANE CONTAINING HOMER AND COLLEGE, ALASKA

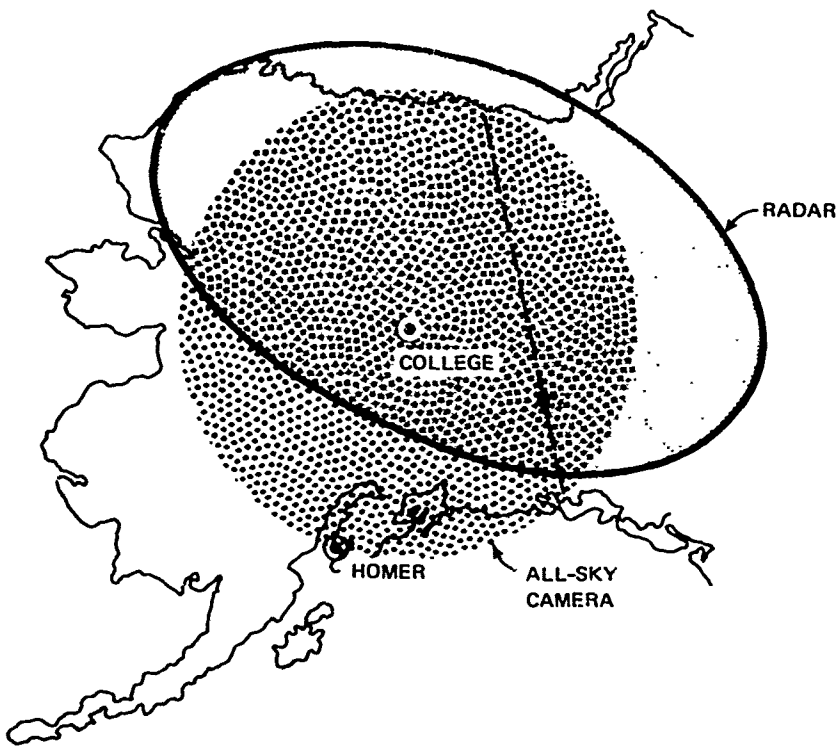

FIGURE 2.3 MAP OF ALASKA SHOWING OVERLAP OF RADAR AND ALL-SKY-CAMERA COVERAGE

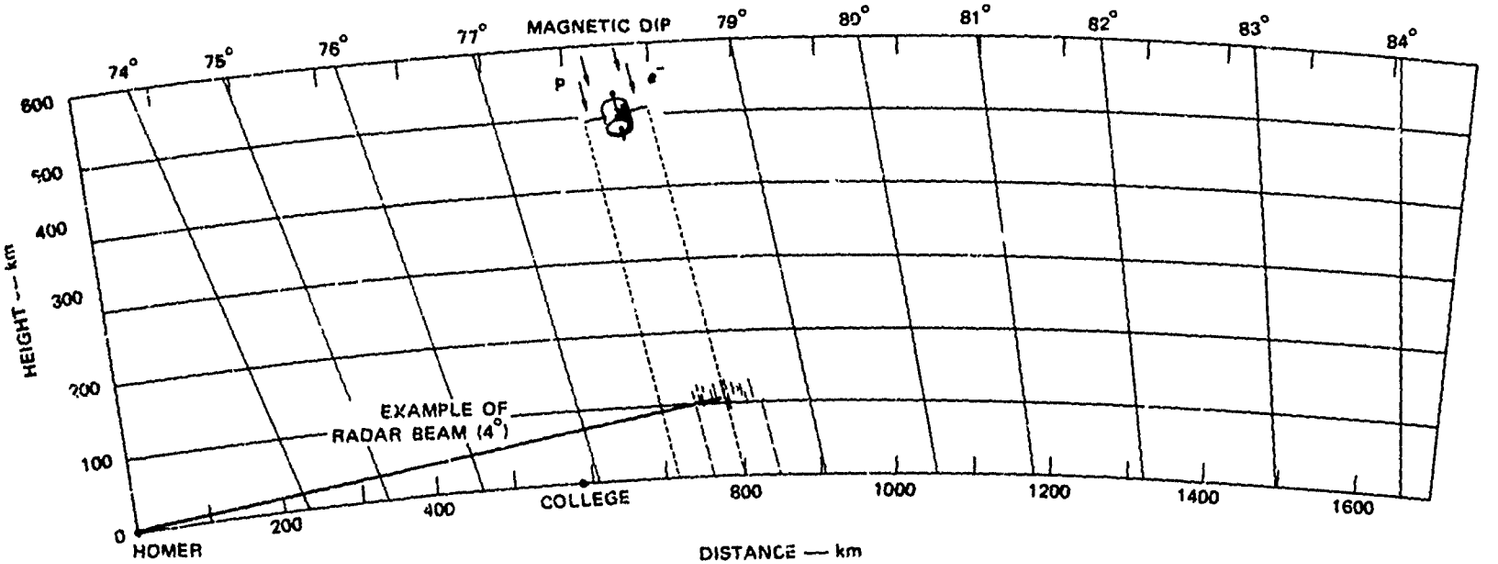

FIGURE 2.4 PROFILE VIEW SHOWING HOW SATELLITE DATA AND RADAR AURORA DATA ARE PROJECTED ALONG MAGNETIC FIELD LINES TO GROUND LEVEL FOR PURPOSES OF COMPARISON

3. EQUIPMENT, OPERATION, AND SCHEDULE

In this section we give pertinent details of the instrumentation that was used on this program. We also indicate the data-taking schedule for the satellite passes for which Lockheed has provided satellite data for our use.

3.1 Homer Radar

The Homer Radar is located on Ohlson Mountain about 13 miles from Homer, Alaska. Figure 3.1 is a photograph of the radar complex. The latitude and longitude of the radar are as follows: latitude 59.7142°N; longitude 151.5333°W. Table 3.1 provides a brief summary of the parameters of this radar. The six radar frequencies shown in the table are fed through the common 60-foot-diameter paraboloid. During satellite passes all radar frequencies were turned on, were operating, and data were recorded. In this work we have utilized only the data obtained at 139 and 398 MHz. A far more detailed distribution of the radar may be obtained from a number of references.[2] Figure 3.2 provides a block diagram of the 139- and 398-MHz radar systems as they were configured for these experiments.

3.2 OV1-18 Satellite

The OV1-18 satellite was instrumented by the Space Sciences Laboratory of the Lockheed Missile System Corporation. Details of the satellite may be found in Lockheed reports.[4,5] The satellite was launched into near polar orbit. The satellite gathered 48 channels of data. The data obtained by Lockheed were corrected for a variety of factors before

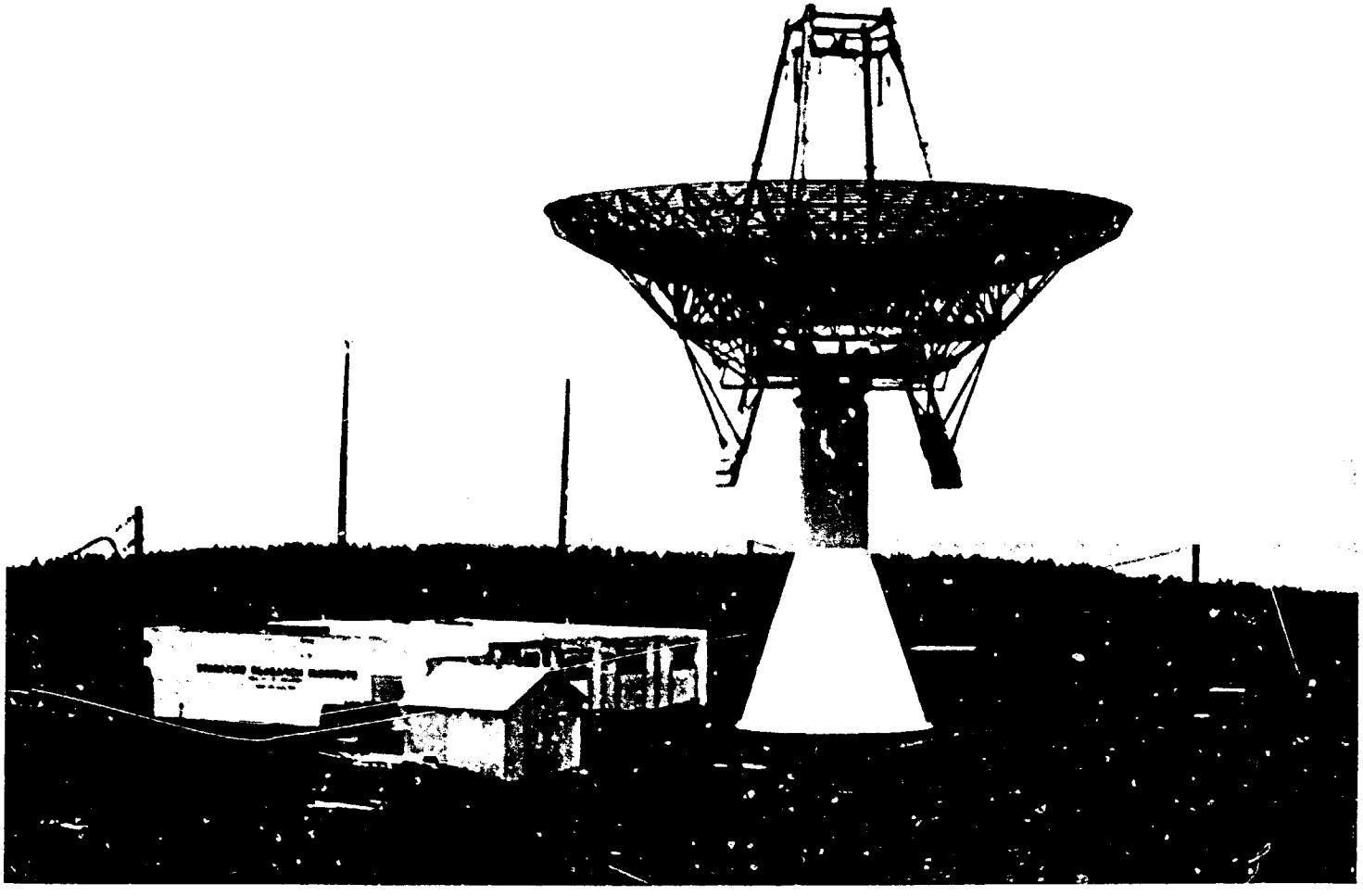

FIGURE 3.1 PHOTOGRAPH OF HOMER RADAR

Table 3.1

HOMER AURORAL RADAR PARAMETERS

Frequency (MHz)	50	139	398	850	1210	3000
Peak power (kW)	30	50	50	40	40	200
Pulse length (μs)	300	300	300	300	300	300
PRF (p/s)	37-1/2	37-1/2	37-1/2	37-1/2	37-1/2	37-1/2
Antenna	Steerable 60-ft-diameter paraboloid					
Antenna efficiency (%)	30	50	50	50	50	50
Antenna half-power beamwidth (deg)	25	9	3	1.5	1	0.4
Receiver bandwidth (kHz)	10	26	26	26	26	26
Two-way line loss (dB)	4	2	2	3	3	4
Receiver dynamic range	Approximately 80 dB					
Polarization (receive and transmit)	V	V	V	H	V	V

being sent to SRI. For instance, counting rates were converted to absolute particle flux; data were selected from many sets of counters according to the momentary satellite orientation (the satellite stabilization mechanisms failed to operate correctly); average electron energy was computed, etc.

Basically, the satellite recorded electron-precipitation flux over a range from 0.8 to 37.0 keV. These data were obtained by five channeltron electron counters, each of which selected electrons over a narrow energy range. Due to peculiarities of the satellite system, sometimes data were supplied from only the four lower-energy channeltron counters. These data covered the energy range from 0.8 to 16.3 keV. The electron-precipitation data were provided to SRI as TSUM or PSUM, which means the total electron flux in electrons per square centimeter per second per steradian. The TSUM included all 5 channels; the PSUM included the flux in the lower four energy channels. The electron-precipitation data supplied to SRI also contained the average electron energy obtained by computing the first moment of the energy spectrum; this is obtained by multiplying the energy of each counter times its particle flux in the five (or four) channeltron counters. This quantity we label EMN. The meaningful counting threshold for these counters was about 5×10^6 counts per second.

The proton-flux data that were transmitted to SRI by Lockheed gave the absolute proton fluxes as obtained by two proton counters. The first is labeled the B counter. The B-type counters measure absolute proton flux for protons with energies above approximately 10 keV. The data provided to SRI were given in protons per centimeter per second per steradian. Meaningful counting-rate threshold was between 1×10^5 and 4×10^5 per second, depending on which of the B counters was being used. Another type of proton counter was labeled the D counter. These proton counters measured absolute flux of protons with energies above 38 keV.

The flux provided SRI was in units of protons per square centimeter per steradian per second. Meaningful counting-rate thresholds were 1×10^5 to 4×10^5 counts per second, again depending on which counter was being used.

A table* presented in the data compilation of Section 4 provides a summary of these counter characteristics, along with other data that are pertinent to understanding the data presentations given there.

3.3 Operation and Schedule

The usual operational procedure was to receive satellite emphemeris data from Lockheed for expected satellite passes. These ephemeris data give predicted satellite position versus time. Accordingly, the Homer radar would provide a sweep of the appropriate regions of the sky during the satellite pass. Before and after the satellite pass the radar would survey the entire sky over Alaska in order to observe the larger picture of overall activity.

There were many occasions during which radar and satellite data were obtained simultaneously. For reasons beyond our control, Lockheed has provided data from only 14 of these satellite passes. These 14 passes were selected because radar aurora or satellite precipitation was measurable. Table 3.2 presents a detailed summary of the 14 passes.

Radar data were obtained over a period of time, from considerably before the expected satellite pass (usually several hours) to a time very late after the pass was expected to be completed (again, usually several hours). The radar data analyzed in this report are for the time period determined from the pre-pass ephemeris data. As a result, the simultaneity of data comparisons between radar and satellite is not always very close. Table 3.3 summarizes this simultaneity more concisely than is obvious

*Table 4.2.

Table 3.2

SUMMARY OF CHARACTERISTICS OF SATELLITE PASSES USED IN THIS STUDY

Date (1969)	Pass Number	Satellite Time (UT)†	Radar Data Time (UT)†	Satellite Altitude (km)	Particle Detector Angle (degrees)		SRI Radar Tape Number	College, Alaska 3-Hour K Index
					Electron	Proton		
28 March	A157	10:19:38 10:22:58	10:20 10:23	480	157-163	Same	144-7	1
2 April	A232	10:51:29 10:52:31	10:50 10:53	474	147-167	Same	144-8	2
11 April	A369	10:26:25 10:29:05	10:28 10:31	479	120-160	Different*	144-18	4
12 April	A388	10:12:43 10:15:33	10:15 10:18	480	160-170	Different*	144-18	1
15 April	A431	11:07:28 11:10:48	11:11 11:14	486	123-161	Different*	144-18	5
19 April	A518	10:13:12 10:15:52	10:20 10:23	494	143-175	Same	144-22	0
26 April	A624	10:12:41 10:14:20	10:12 10:15	515	143-174	Same	145-1	1
29 April	A641	11:04:47 11:07:16	11:19 11:22	522	38-108	No Proton Data Supplied	145-1	0
30 April	A657	10:50:54 10:53:43	10:51 10:54	526	54-145	Same	145-2	5
1 May	A676	10:37:33 10:39:50	10:37 10:40	530	120-180	Same	145-2	2
6 May	A751	11:02:15 11:03:55	11:01 11:04	546	94-158	Different*	145-9	3
29 Sept	A2964	12:27:20 12:30:10	12:27 12:29	548	36-156	Proton Data Below Threshold	146-23	6
30 Sept	A2979	12:09:54 12:12:49	12:10 12:13	545	55-151	No Early Proton Data	147-6	7
1 Oct	A2995	11:53:42 11:55:47	11:53 11:56	540	62-121	Same	147-8	7

*"Different", but we do not have the appropriate information.

†To convert to Alaska Standard Time (150° West time) subtract 10 hours.

Table 3.3

SIMULTANEITY OF DATA PERIODS
FOR SATELLITE PASS AND RADAR DATA

Satellite Pass Number	Percent of Time Radar Data Overlapped Satellite Data	Time Difference Between Middle of Satellite Data and Middle of Radar Data (minutes : seconds)	College, Alaska 3-Hour Magnetic K Index
A157	85	15	1
A232	100	30	2
A369	40	1 : 45	4
A388	20	2 : 20	1
A431	0	3 : 20	5
A518	0	7 : 0	0
A624	100	0	1
A641	0	14 : 25	0
A657	95	15	5
A676	100	10	2
A751	100	35	3
A2964	55	45	6
A2979	95	10	7
A2995	100	15	7

from Table 3.2. Simultaneity of passes A431, A518, and A641 was exceedingly poor. For passes A518 and A641 the poor time simultaneity probably does not matter since our experience shows that the low K indices imply geographically stable phenomena. Pass A431 occurred during high activity, so that lack of time simultaneity of the measurements makes our comparisons less valuable for this pass.

The data collection was near midnight local time in all cases except in October 1969. During October 1969 coordinated measurements were made on eight midday satellite passes. No radar aurora was observed during any of these daytime passes. We do not know if the Lockheed satellite recorded precipitation in these regions of the ionosphere during these passes.

The radar data that were obtained were tape recorded on a 14-channel analog instrument. The data were read back in analog fashion. The radar data were measured, geometrically corrected, and plotted on maps that will be presented later, in Section 4. The satellite data were reduced by computer before Lockheed delivered the data to SRI. At SRI a number of computations were made on the satellite data. The results of these computations are presented in Section 4.

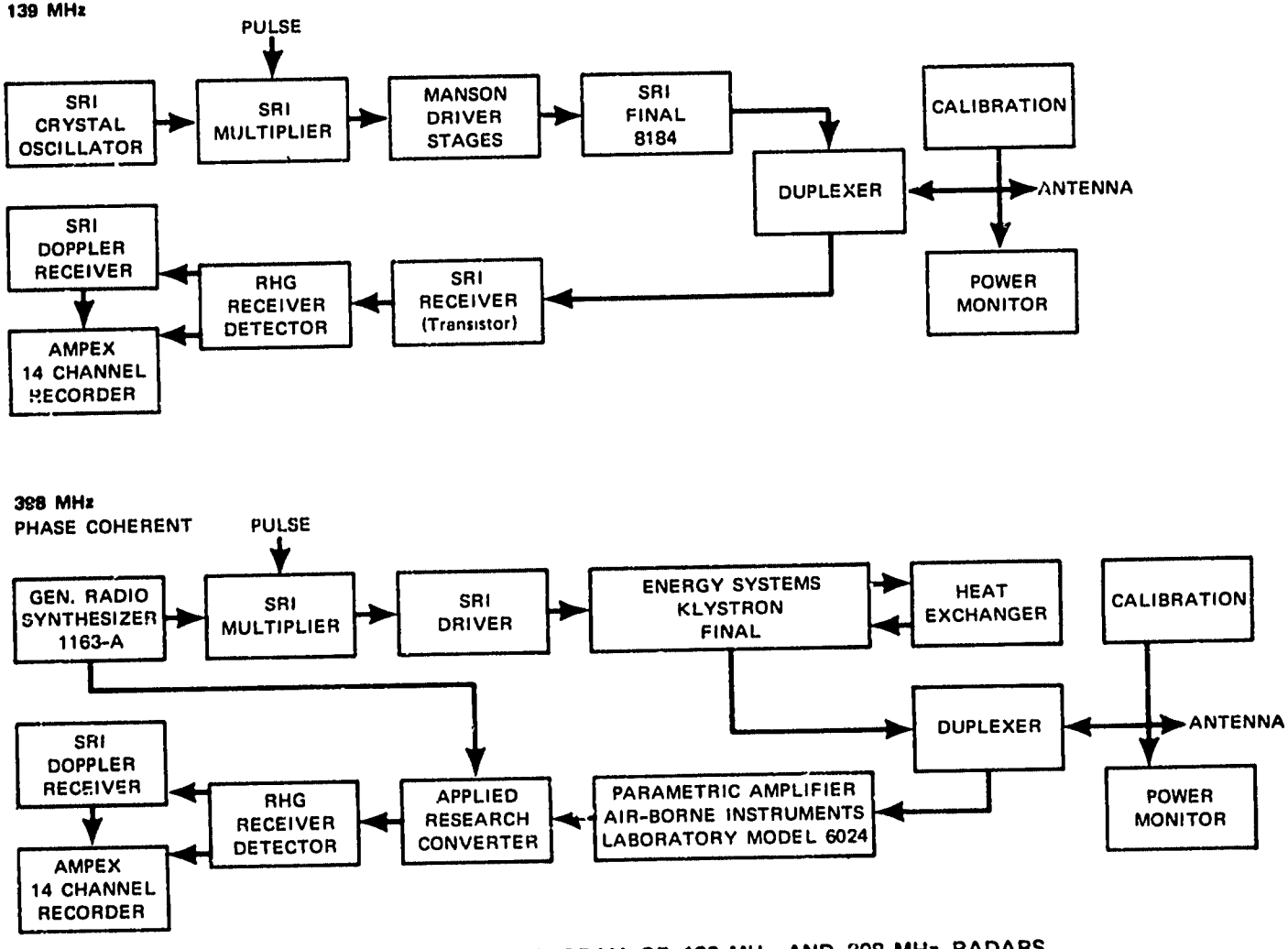

FIGURE 3.2 BLOCK DIAGRAM OF 139-MHz AND 398-MHz RADARS

4. SATELLITE RADAR-DATA COMPILATION

Satellite precipitation data were provided to SRI for 14 nighttime satellite passes during which measurable precipitation and radar aurora were simultaneously present. Note that radar aurora was not present when there was no precipitation. Also, recall that during October 1969 coordinated measurements were made on eight midday satellite passes. During these daytime passes, no radar aurora was observed, though at this writing we do not know whether the satellite observed any precipitation.

The data obtained are presented in this section in several ways. The main effort is to provide information that allows for a comparative study of the spatial locations of radar aurora and the simultaneously observed satellite precipitation measurements. There are five kinds of data presentations. They will be described in more detail below. Briefly, they are as follows:

- The first format is a map of Alaska with the projection of the satellite orbit down the earth's magnetic field lines onto the map. Also shown on the map are the areas in which radar aurora was found. The maps give an indication of where precipitation was occurring.
- The second data presentation is a series of A-scope photographs giving radar aurora intensity.
- The third and fourth formats provide various data concerning electron precipitation and proton precipitation versus orbital time.

- The fifth format provides histograms of occurrence of electron-number flux, electron-energy flux, and average electron energy for each of the 14 passes according to whether radar aurora was or was not present in the precipitation region. For easy identification, the figures in these five formats are designated by figure numbers containing the letters A, B, C, D, and E, respectively.

All data are labeled according to satellite orbit number. Data are presented in order of ascending three-hour magnetic index at College, Alaska. Table 3.2 provides a schedule of satellite passes and other pertinent information. The times shown on all figures are Universal Time (Greenwich Meridian Time). Subtract 10 hours to convert to Alaska Standard time. Thus it will be seen that all measurements reported here were made between midnight and 2 AM local time in Alaska. Note that because the Homer radar can observe aurora over a wide azimuth around magnetic north, radar aurora may be measured from areas that are experiencing significantly earlier or later local magnetic time than at the radar site itself. During all measurements reported here the E-region was in darkness. Table 4.1 lists satellite passes according to ascending K index. The table summarizes other pertinent information.

4.1 Maps of Alaska

In Figures 4.A.1 through 4.A.14 we present 14 maps of Alaska, one for each of 14 satellite passes. The maps show the location of the Homer radar facility near the bottom of each figure. Each map is labeled with the date of the satellite pass, the satellite orbit number, and the radar frequency for which clutter returns are shown. The satellite orbit as projected down the earth's magnetic field lines to the earth's surface is shown on the map. Tic marks indicate Universal Time along this orbital projection. The total energy precipitated as a function of orbital

Table 4.1

SUMMARY OF SATELLITE PASSES ORDERED ACCORDING TO MAGNETIC ACTIVITY

Sequence No.	Pass No.	3-Hour Magnetic Index-K	Time Simultaneity of Radar and Satellite Data (minutes:seconds)	Subjective Character of Precipitation (See Section 6 for description)	
				Electrons	Protons
1	A518	0	7:00 Poor	--	--
2	A641	0	14:25 Very poor	--	none
3	A624	1	0:00 Good	--	--
4	A157	1	0:15 Good	--	--
5	A388	1	2:20 Good	E	--
6	A232	2	0:30 Good	E	wp
7	A676	2	0:10 Good	E	--
8	A751	3	0:35 Good	E	--
9	A369	4	1:45 Fair	E	--
10	A657	5	0:15 Good	E	wp
11	A431	5	3:20 Poor	E	P
12	A2964	6	0:45 Fair	E	none
13	A2995	7	0:15 Good	E	P
14	A2979	7	0:10 Good	E	P

position along the orbit is shown by means of cross-hatched areas. The amplitude of the cross-hatching from the satellite orbit is linearly proportional to energy deposition. In an effort to make the presentation more legible, the cross-hatched areas are extended on both sides of the orbit.

Radar aurora are shown on the map by speckled areas. The region from which clutter was obtained, if it was well mapped by the radar, is also outlined with a heavy line. In other cases data are presented

only along the satellite orbit. In these cases the radar aurora is shown as speckled with heavy boundaries that are not closed.

On several satellite passes there are special considerations. These will be noted on the figures.

4.2 Radar-Aurora Signal-Intensity Plots

Radar auroral echo strength and location of radar echoes are determined in this report from A-scope photographic records. An A-scope record presents signal intensity or signal voltage as a function of range from the radar. The A-scope photographs presented are time-exposure photographs of approximately 30 seconds duration. The figures are annotated with radar frequency used, time duration of signal integration (Universal Time--subtract 10 hours for Alaska Standard time.), and antenna azimuth and elevation. The A-scope records provide approximate logarithm of signal amplitude (post-detection amplitude) versus range in kilometers. On some figures we have placed the symbol $\approx$, which indicates that during the integration time the radar aurora amplitude seemed to vary in amplitude in a significant way.

Figure 4.B.0 presents calibration signal amplitudes that may be used with the A-scope photographs. The calibrations are given in terms of power input into the receivers for both the 139- and 398-MHz radars. Calibration must be done in this way rather than as radar cross section because cross-section calibration would be a function of range, aurora geometry, antenna beam pattern, etc. A value of -100 dBm corresponds approximately to 10^{-11} m^2/m^3. This relationship assumes radar aurora is on the order of 10 kilometers in vertical thickness, at a range of about 800 kilometers, and is beam-filling in the azimuth direction. Figures are labeled according to three-hour magnetic index in ascending order. The radar signal amplitudes for 14 satellite passes are presented in Figures 4.B.1 through 4.B.14.

4.3 Satellite Data

The satellite data are presented in the form of computer-drawn graphs. Data are presented for electron precipitation and proton precipitation separately.

4.3.1 Electron-Precipitation Data

Electron-precipitation data versus orbital time (Universal Time--subtract 10 hours for Alaska Standard time) are presented in Figures 4.C.1 through 4.C.14. In each figure are shown plots of three separate quantities. The top part of each figure presents T-PSUM. The ordinate in the top figure is logarithmic in electrons per square centimeter per second per steradian. In regions where no data points are shown, the counting rates were low; at the suggestion of Lockheed personnel we have imposed a threshold at a value near to or just equal to the on-board, radioactive-calibration-source counting rate. In some cases, through oversight, the amount of time for which data were supplied to us was less than we required.

The middle part of each figure presents as ordinate the quantity EMN. This quantity is the mean energy of the precipitating electrons as determined by the five (or four) energy-selecting electron counters. The units are linear from 0 to 10 kV. The bottom part of each figure presents as its ordinate the logarithm of the product of the T-PSUM times EMN. The units are electron-keV per square centimeter per second per steradian. This curve provides a measure of energy flux (power) as a function of position along the satellite orbit. We have indicated on the figures, by cross-hatched regions along the trajectory, where radar aurora simultaneously existed. Table 4.2 provides a summary description of the quantities given in Figures 4.C.1 through 4.C.14.

Table 4.2

SUMMARY OF DEFINITIONS
OF VARIOUS SATELLITE DATA QUANTITIES

Electrons	
TSUM	Total electron flux between 0.8 and 37 keV as measured by five energy-selecting channeltron counters. Meaningful threshold: 5.10^6 counts/s. Units: el/cm^2-s-ster.
PSUM	Total electron flux between 0.8 and 16.3 keV as measured by four energy-selecting channeltron counters. Meaningful threshold: 5.10^6 counts/s. Units: el/cm^2-s-ster.
EMN	Average electron energy determined from counting-rate distribution in five (four) channeltron counters.
ELE	Total electron energy flux (power density): (TSUM × EMN, or PSUM × EMN).
Protons	
B	Proton flux, protons/cm^2-s-ster. Approximately 10-keV threshold, no upper limit. Meaningful counting-rate threshold: 1×10^5 to 4×10^5 counts/s, depending on the counter.
D	Proton flux, protons/cm^2-s-ster, 38-keV threshold, no upper limit. Meaningful counting-rate threshold: 1×10^5 to 4×10^5 counts/s, depending on the counter.
$\bar{E}$	Average proton energy under the assumption that the proton energy spectrum is exponential. This quantity is determined from the relative counting rates in the B and D counters.
$\Delta\bar{E}$	Approximate fractional statistical error in proton average energy
PAV	Total proton energy flux (power density)--(B counter flux rate times $\bar{E}$).
ΔPAV	Approximate fractional statistical error in total energy flux.

As an aid in data-correlation work, an arrow has been placed at the bottom of these figures. A vertical line carries the position of the arrow across all of the subfigures. The arrow shows the point in time when the satellite crossed the L-shell that goes through College, Alaska. Also indicated is a distance in kilometers--east or west of College--where this transit took place. The 3-hour magnetic K index from the College magnetic observatory of the U.S. Coastal and Geodetic Survey is also indicated.

All satellite paths for which data are used in this report were north-to-south transits. We have indicated on the figures that the left-hand side is north and the right-hand side is south as a reminder of this fact.

4.3.2 Proton-Precipitation Data

Figures 4.D.1 through 4.D.14 present proton-precipitation data as a function of orbital position. There are five subfigures in these figure sets. The top subfigure provides as ordinate the logarithm of the proton flux in the B counters. The B counters provide flux measurements for protons with energies greater than 10 keV. The units are protons per square centimeter per second per steradian. Regions in which there are no data plotted are regions where the counting rate dropped to a value to be expected from radioactive calibration sources alone. At Lockheed's suggestion we have imposed a threshold below which no data points were plotted.

The second subfigure from the top provides as ordinate the logarithm of the average proton energy versus orbital position. The ordinate is labeled $\bar{E}$. The average energy is computed in kilovolts. The average proton energy is estimated using the assumption that the proton-energy spectrum is exponential in energy. Under this assumption the

relative counting rates in counters B and D can be used to estimate the average energy. Note that for an exponential energy distribution the average energy and the e-folding energy are the same.

The B counters and the D counters are independent of one another. Each counter, measuring proton flux over a short time period, provides statistically independent samples. Therefore, each value is subject to statistical fluctuations; when the proton mean energy becomes large, or the absolute counting rate becomes small, the determination of the average proton energy, $\bar{E}$, becomes statistically uncertain. Based on information provided to us by Lockheed, we have produced in the third subfigure an estimate of the statistical accuracy of the $\bar{E}$ estimate. In fact, the way data are handled on board the satellite does not allow for good statistical estimation of data accuracy; it is believed though that $\Delta\bar{E}$ provides an approximate fractional, statistical error in our estimate of proton average energy. This is a linear scale of fractional error from 0 to 1. Certainly when our estimate of this error is close to one, the estimate of $\bar{E}$ is quite uncertain. When the estimated error is near 0, then our estimate of average proton energy is liable to be statistically accurate; however, the reader must remember that the derivation of $\bar{E}$ assumes an exponential form for the proton spectrum. We do not know whether this analytical form is a good fit to the real precipitation spectrum.

The fourth subfigure from the top presents the logarithm of the total proton energy flux as ordinate. The ordinate is labeled PAV. This quantity, PAV, is the flux in Counter B times the average proton energy; hopefully, PAV is proportional to the incident power density of protons impinging on the top side of the ionosphere.

The estimate of PAV includes the statistically uncertain estimate of $\bar{E}$. We have therefore provided in the bottom subfigure an

estimate of the fractional error in the total proton energy flux. This fractional, statistic error varies linearly from 0 to 1. The ordinate is labeled ΔPAV. As with our estimate of the fractional error in $\bar{E}$, when our estimate of the fractional error in PAV is large, our estimate of PAV is clearly very poor. When the fractional error, ΔPAV, is near 0, the accuracy of the statistical estimation of PAV will be quite good; however, the reader must remain cognizant of the fact that the quantity PAV includes an assumption of an exponential proton energy spectrum. As indicated above, we do not know how valid this assumption is. Table 4.2 summarizes the quantities in Figures 4.D.1 through 4.D.14.

As with the electron plots, the location of the satellite transit of the College, Alaska L-shell is indicated, as is the College three-hour magnetic index. Satellite transit is from north to south. This is also indicated on the figure.

4.3.3 Histograms of Electron-Precipitation Data

In order to seek a definitive correlation between radar aurora and electron precipitation a series of histograms has been prepared. Data have been organized so that two histograms appear on each subfigure. Each histogram presents the number of measurements of a particular quantity from regions of the satellite pass where no radar echoes were observed (i.e., regions where they could have been observed if the environment had given rise to scattering). On the same subfigure another histogram presents the same quantity for regions where radar echoes were observed. The histogram sets are given in Figures 4.E.1 through 4.E.14.

The top subfigure gives two histograms of the electron number flux--TSUM--according to presence or absence of radar aurora. Note that both the abscissa and the histogram interval widths are logarithmic. For greater ease of display the ordinate is also logarithmic--with a place provided for zero cases. Satellite data are read once per

second. Therefore the number of cases plotted corresponds to the number of seconds of data that were obtained, subject to other constraints. The particle-flux threshold value of 5×10^6 was applied in order to eliminate data dominated by the radioactive calibration source.

The middle subfigure gives two histograms of the electron-energy flux (ELE) according to presence or absence of radar aurora. Note that the abscissa and ordinate are logarithmic.

The bottom subfigure gives two histograms of average electron energy (EMN) according to presence or absence of radar aurora. Only the ordinate is logarithmic in this plot.

4.4 Comments on Specific Satellite Passes

In this subsection we discuss features of several of the satellite passes that may help the reader to better understand the limitations of this experiment. Some of these comments relate to work that is presented later, in Section 6 of this report.

4.4.1 Satellite Pass A388

If electron precipitation in the area of Bar 1 (see Figure 4.A.5) produces radar clutter, then it probably would not be seen by the radar since the usual clutter altitude of 110 km is just beyond the radar horizon. Furthermore, the magnetic aspect is 3°, further discriminating against observing clutter. The area of weak clutter shown is bounded in the north by the southern boundary of detectable electron precipitation (threshold taken to be 5×10^6 el/cm^2-s-ster). There is no evidence of proton precipitation in the area. An undetected electron precipitation flux in this area with a flux just below 5×10^6 could produce 6×10^4 el/cm^3. This density might be enough to allow auroral radar echoes to be obtained should this ionization become structured into irregularities.

4.4.2 Satellite Pass A431

The maps of Pass A431 (Figure 4.A.11) show that the observed radar clutter does not coincide with regions of maximum energy deposition. The plots of the B-counter (proton) and the TSUM (electron) count show that, in regions where clutter is observed, there is precipitation of both protons and electrons. The E-region was not illuminated by the sun. A monoenergetic electron beam of 3 or 4 keV, the average energy indicated by EMN, would not penetrate to the appropriate altitude. We presume that the actual spectrum is spread in energy. The proton average energy exceeded 10 keV in this same area of the sky; this average energy can produce ionization in the relevant regions of the ionosphere.

The electron flux in the main clutter region varies between 10^7 and 3×10^7 el/cm^2-s-ster. The proton flux is approximately 3×10^6. The data of Figures 6.2 and 6.5 (see Section 6) suggest production of steady-state E-region densities of from 8×10^4 to 1.5×10^5 due to electron precipitation, and $\sim 8 \times 10^4$ due to proton ionization. The steady-state electron density due to both electrons and protons would therefore be likely to exceed 10^5. This background ionization is probably sufficient to produce observable auroral radar clutter.

We note that the electron-precipitation flux is very much greater, by a factor of 10 to 30, in regions where no clutter is obtained, though time simultaneity of measurement is not very good. Most observers believe that the electron-density irregularities that cause radar scattering from E-region ionization are caused by electric fields. This single satellite pass may suggest that regions of higher precipitation levels produce higher conductivities that cause "short-circuiting" of the ionospheric electric fields.

The region of intense electron precipitation between 64° and 65° north latitude lies in an area where the magnetic aspect angle

from the radar exceeds 3°. Therefore, the radar cannot well monitor the clutter environment in that region of the sky.

4.4.3 Satellite Passes A2979 and A2995

These two passes occurred during a high-energy proton aurora. The proton flux into the B counters was not extraordinarily large, being in the neighborhood of 10^6 protons/cm^2-s-ster. But the energies of the protons were so large that the determination of average energy--assuming an exponential spectrum--was jeopardized by statistical errors. That is, the B- and D-counter counting rates were nearly equal; this means that most protons had energies above the 38-keV threshold of the D counters. The ratio of the B to D counting rate would be nearly 1.0. The logarithm of this ratio is divided into a constant to determine $\bar{E}$. Any statistical fluctuation in counting rate of either counter could bring the ratio to 1.0, thereby driving the logarithm to zero and causing us to compute an infinite average energy. The proton energies are so high that an "average energy" determination from the counting ratio of B to D is statistically meaningless.

Electron precipitation was taking place nearly everywhere on Pass A2979. On Pass A2995 the electron precipitation was also widespread. The average electron energy was high on Pass A2979, being about 6 keV. On Pass A2995 the electron energy was somewhat less.

Radar aurora was intense and very widespread during Pass A2979. The clutter was weaker and contained spatial gaps on Pass A2995. We could characterize both events as occurring during intense aurora, though A2979 was stronger. In spite of the apparent tendency of regions of peak precipitation intensity and radar aurora to anti-correlate (not overlap) during satellite passes when auroral activity is weaker, there seems to be good overlap in the locations of the two phenomena for these two passes.

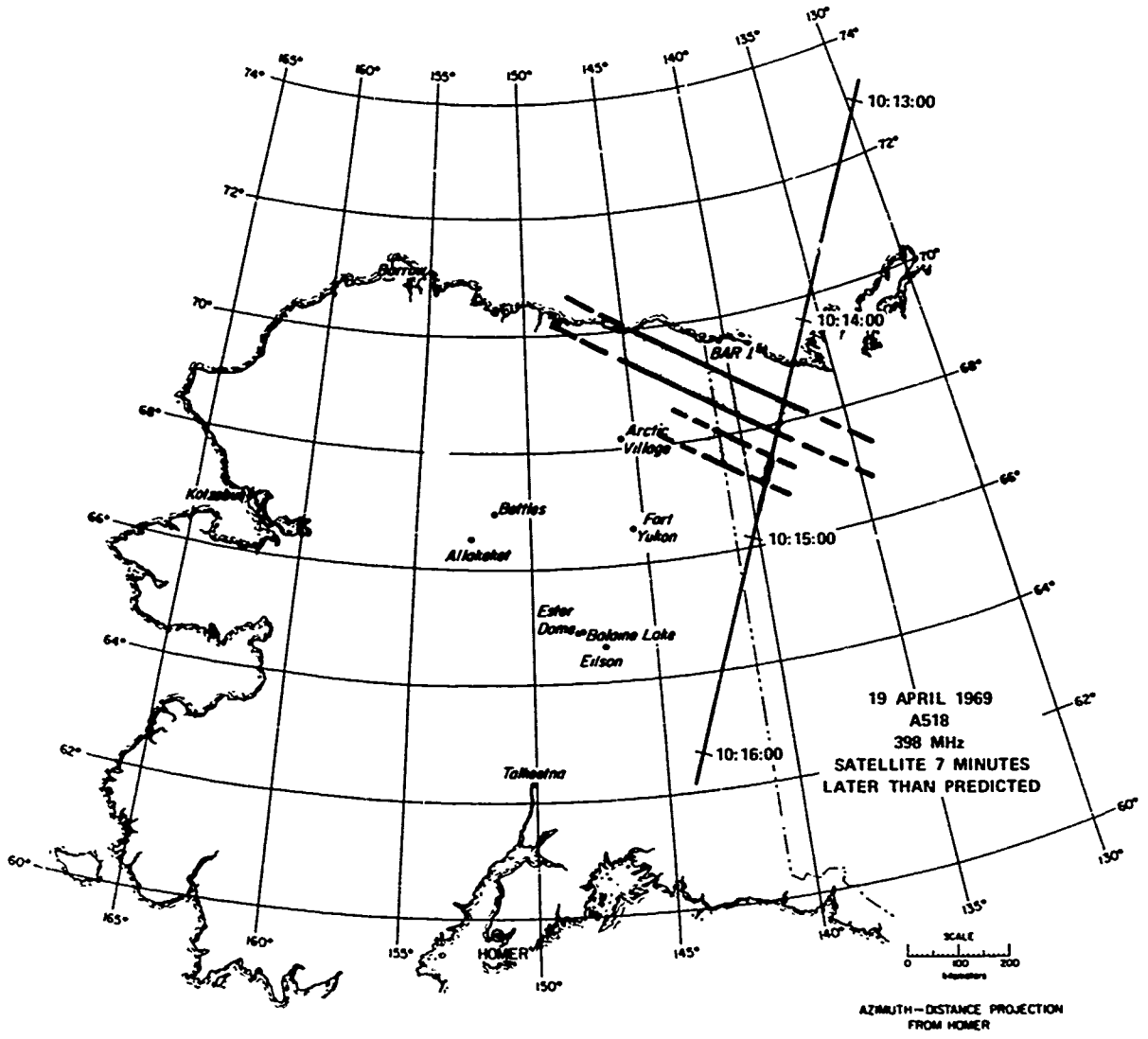

FIGURE 4.A.1 MAP OF ALASKA SHOWING GROUND PROJECTION OF SATELLITE ORBIT, PRECIPITATING ELECTRON ENERGY FLUX ALONG THE ORBIT, AND RADAR AURORAL DISTRIBUTIONS DURING PASS A518

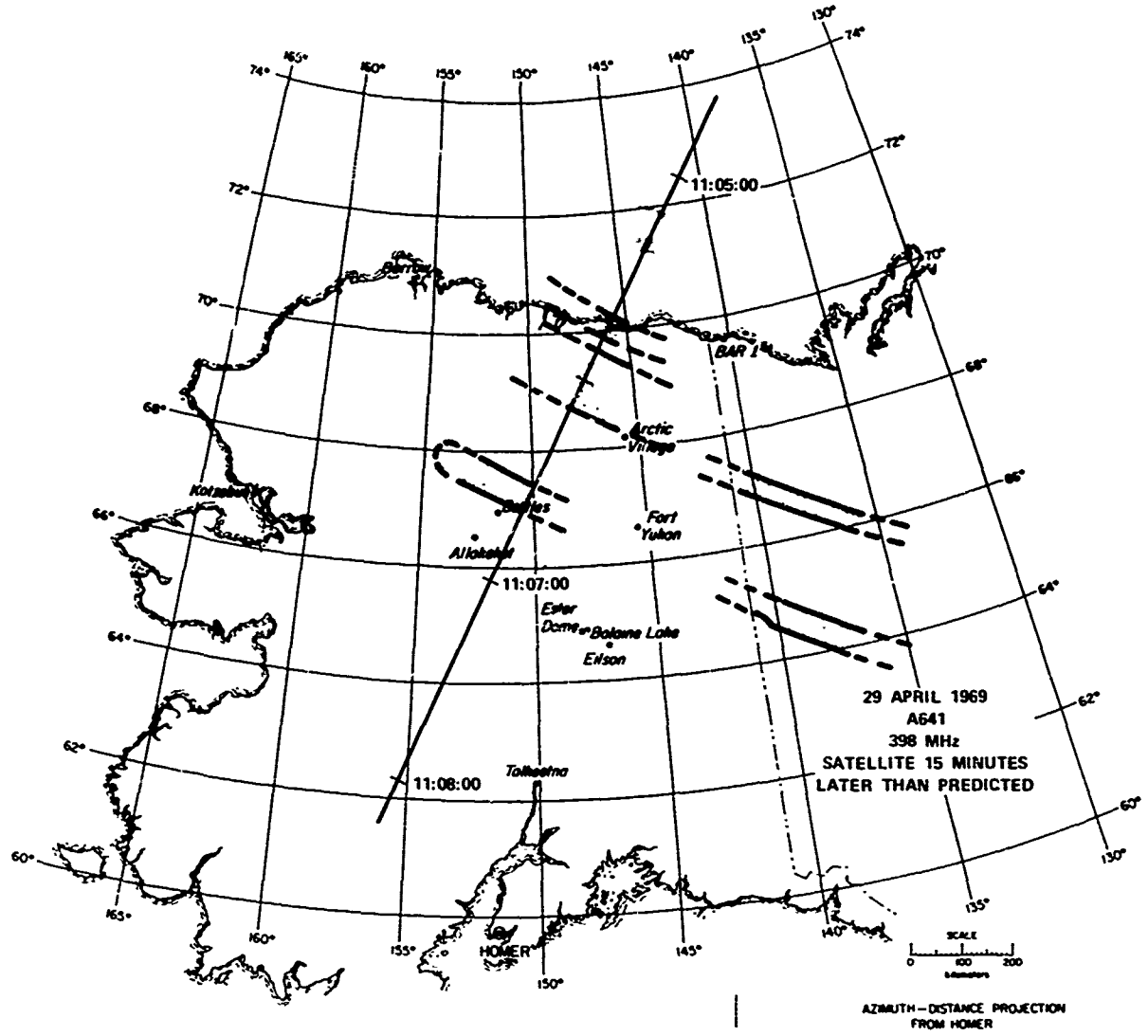

FIGURE 4.A.2 MAP OF ALASKA SHOWING GROUND PROJECTION OF SATELLITE ORBIT, PRECIPITATING ELECTRON ENERGY FLUX ALONG THE ORBIT, AND RADAR AURORAL DISTRIBUTIONS DURING PASS A641

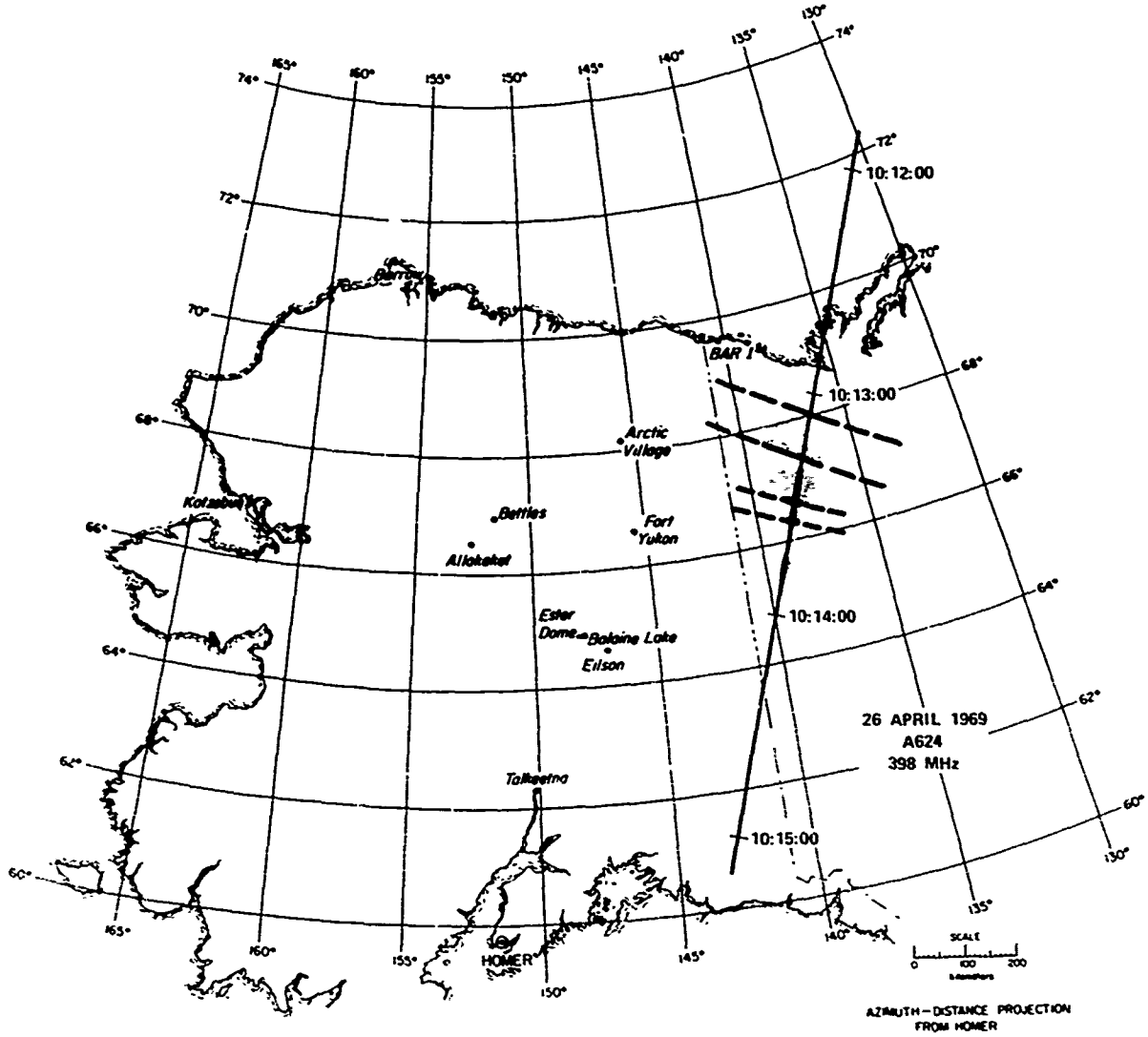

FIGURE 4.A.3 MAP OF ALASKA SHOWING GROUND PROJECTION OF SATELLITE ORBIT, PRECIPITATING ELECTRON ENERGY FLUX ALONG THE ORBIT, AND RADAR AURORAL DISTRIBUTIONS DURING PASS A624

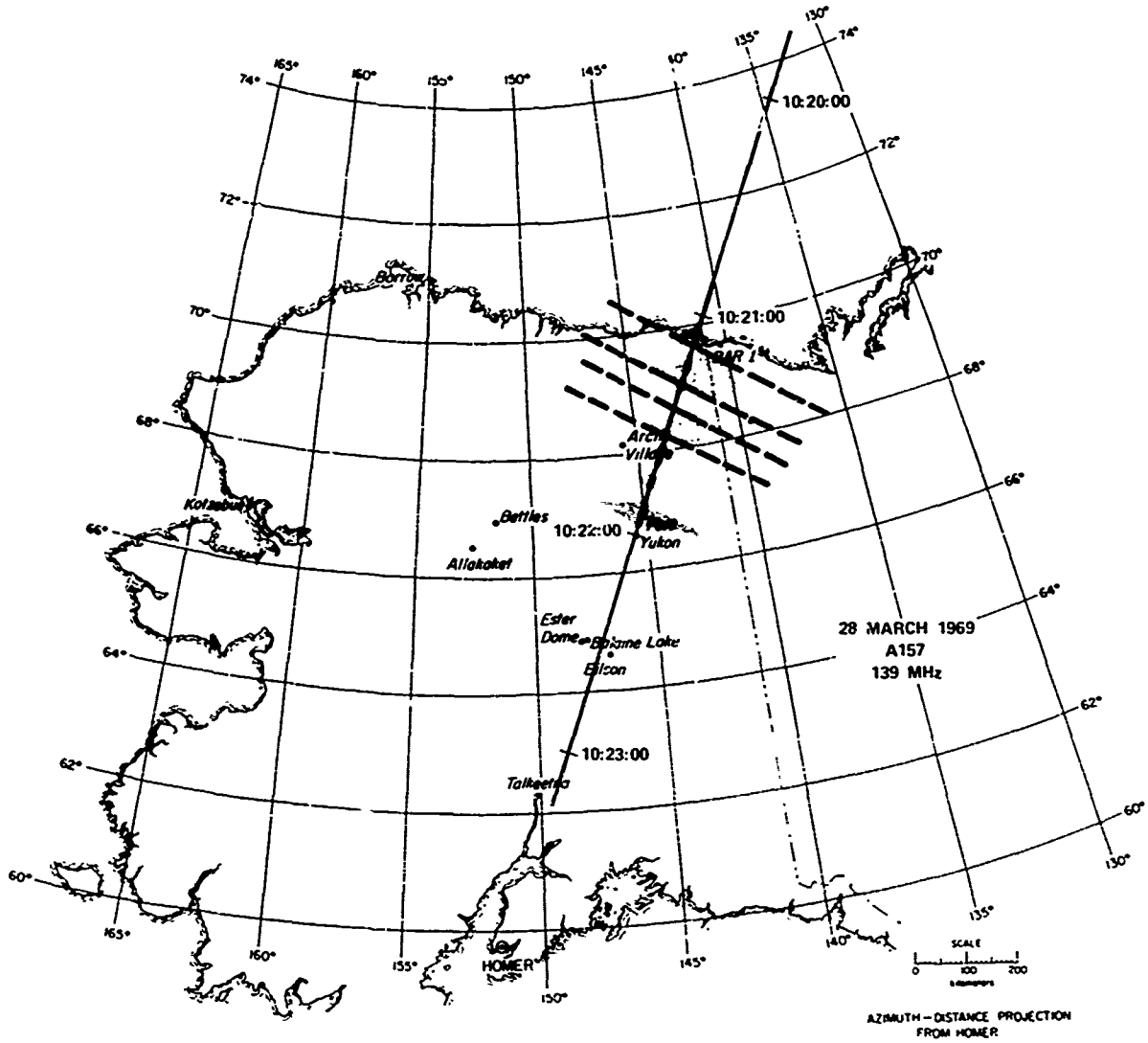

FIGURE 4.A.4 MAP OF ALASKA SHOWING GROUND PROJECTION OF SATELLITE ORBIT, PRECIPITATING ELECTRON ENERGY FLUX ALONG THE ORBIT, AND RADAR AURORAL DISTRIBUTIONS DURING PASS A157

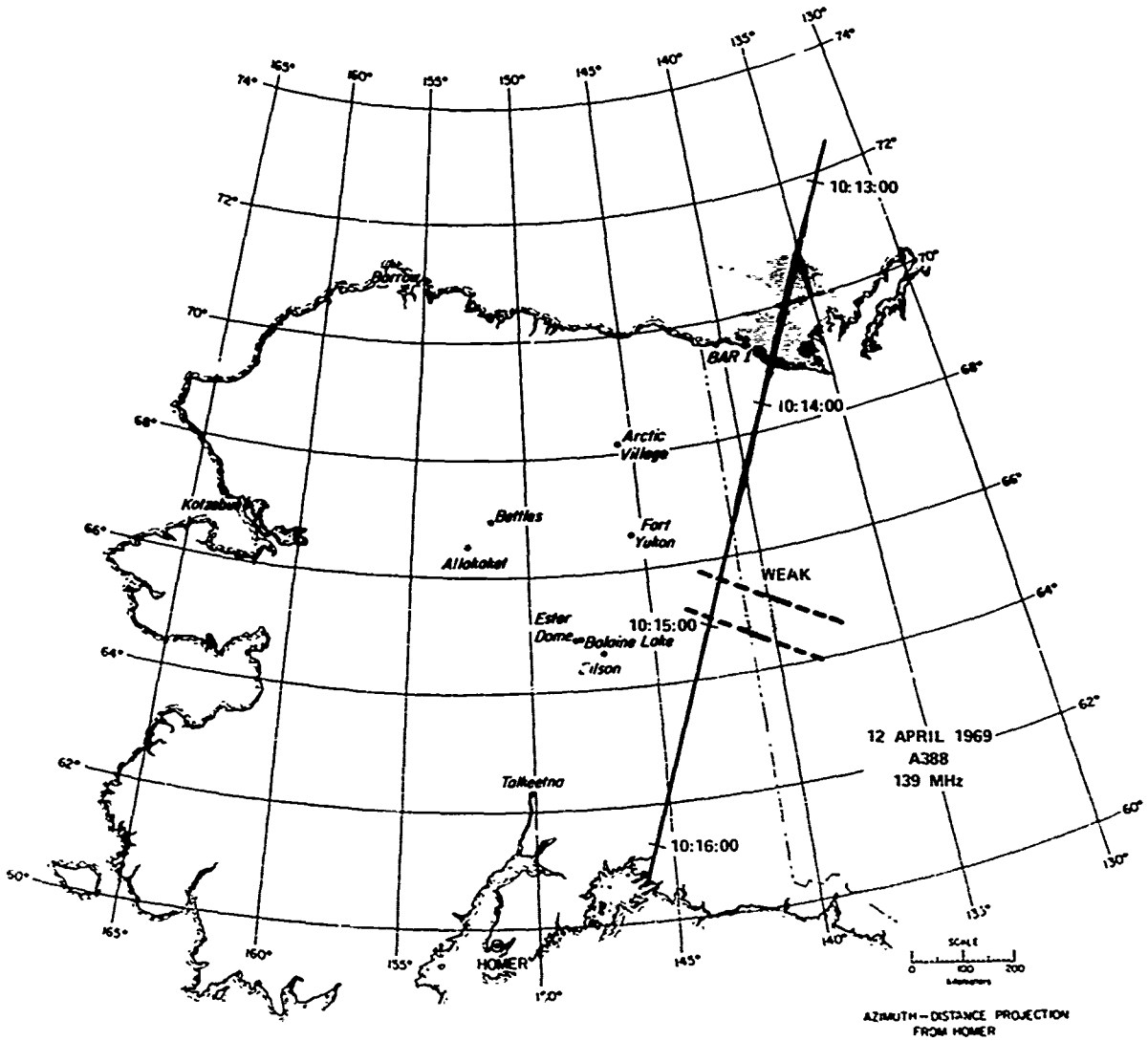

FIGURE 4.A.5 MAP OF ALASKA SHOWING GROUND PROJECTION OF SATELLITE ORBIT, PRECIPITATING ELECTRON ENERGY FLUX ALONG THE ORBIT, AND RADAR AURORAL DISTRIBUTIONS DURING PASS A388

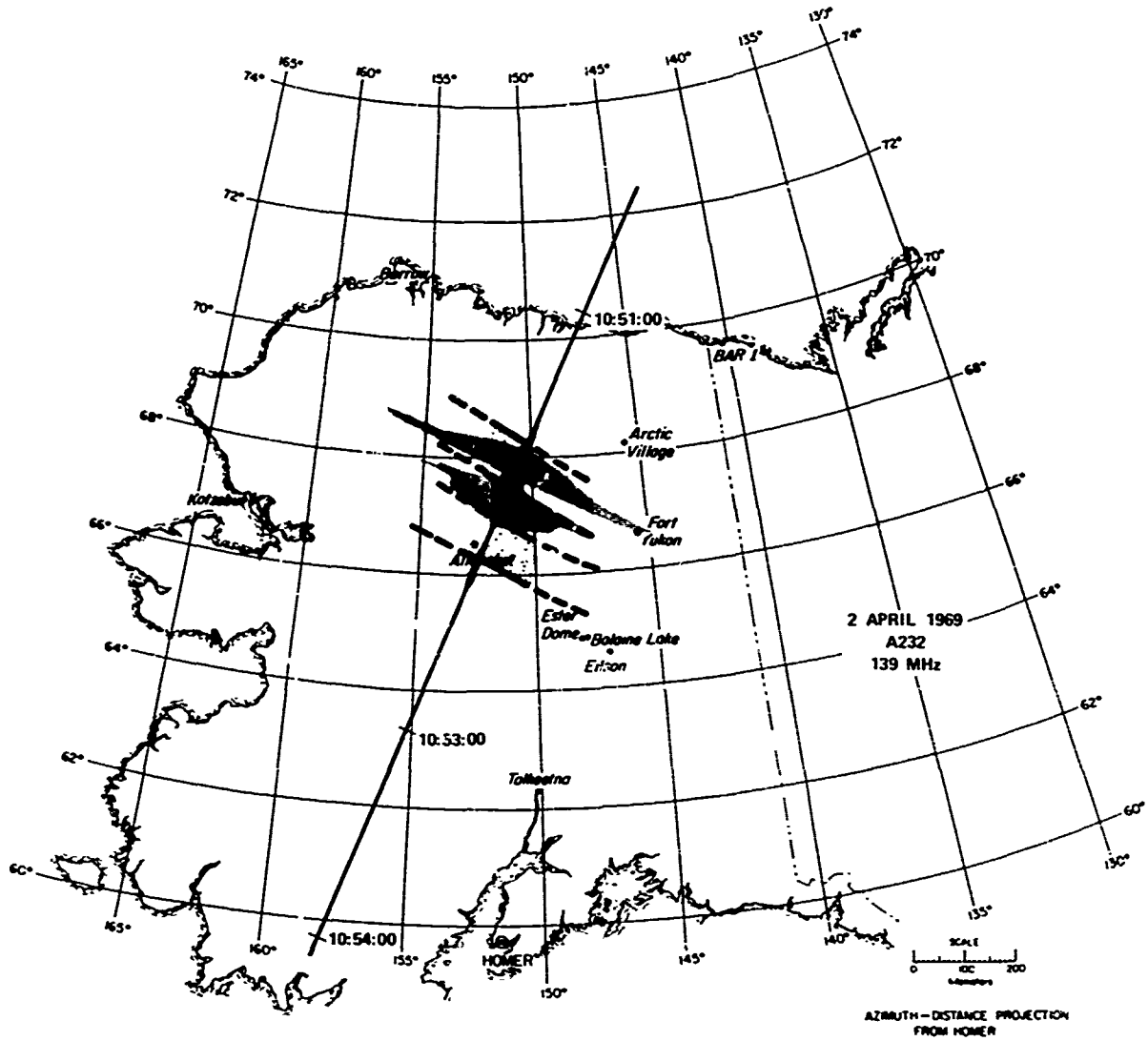

FIGURE 4.A.6 MAP OF ALASKA SHOWING GROUND PROJECTION OF SATELLITE ORBIT, PRECIPITATING ELECTRON ENERGY FLUX ALONG THE ORBIT, AND RADAR AURORAL DISTRIBUTIONS DURING PASS A232

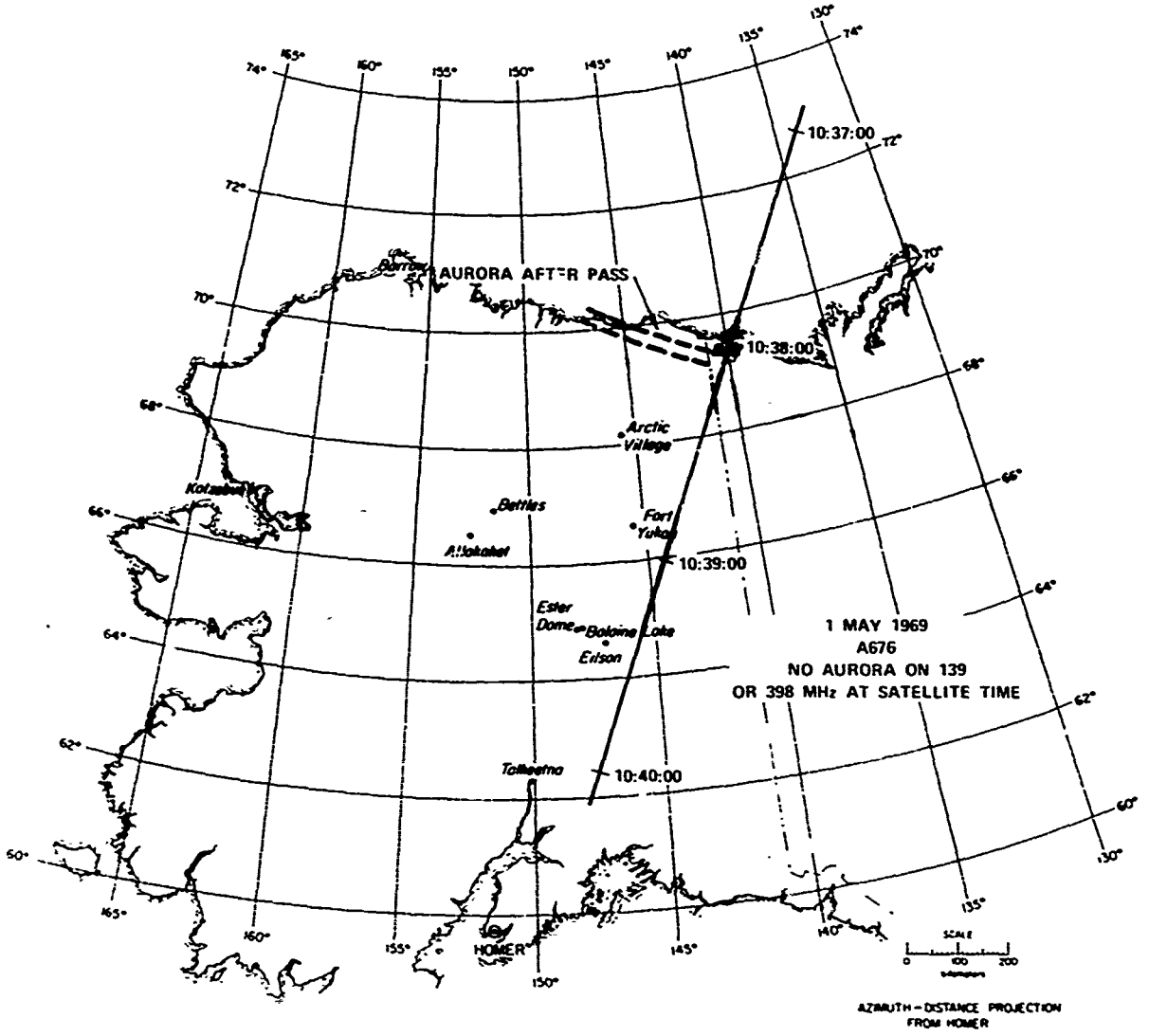

FIGURE 4.A.7 MAP OF ALASKA SHOWING GROUND PROJECTION OF SATELLITE ORBIT, PRECIPITATING ELECTRON ENERGY FLUX ALONG THE ORBIT, AND RADAR AURORAL DISTRIBUTIONS DURING PASS A676

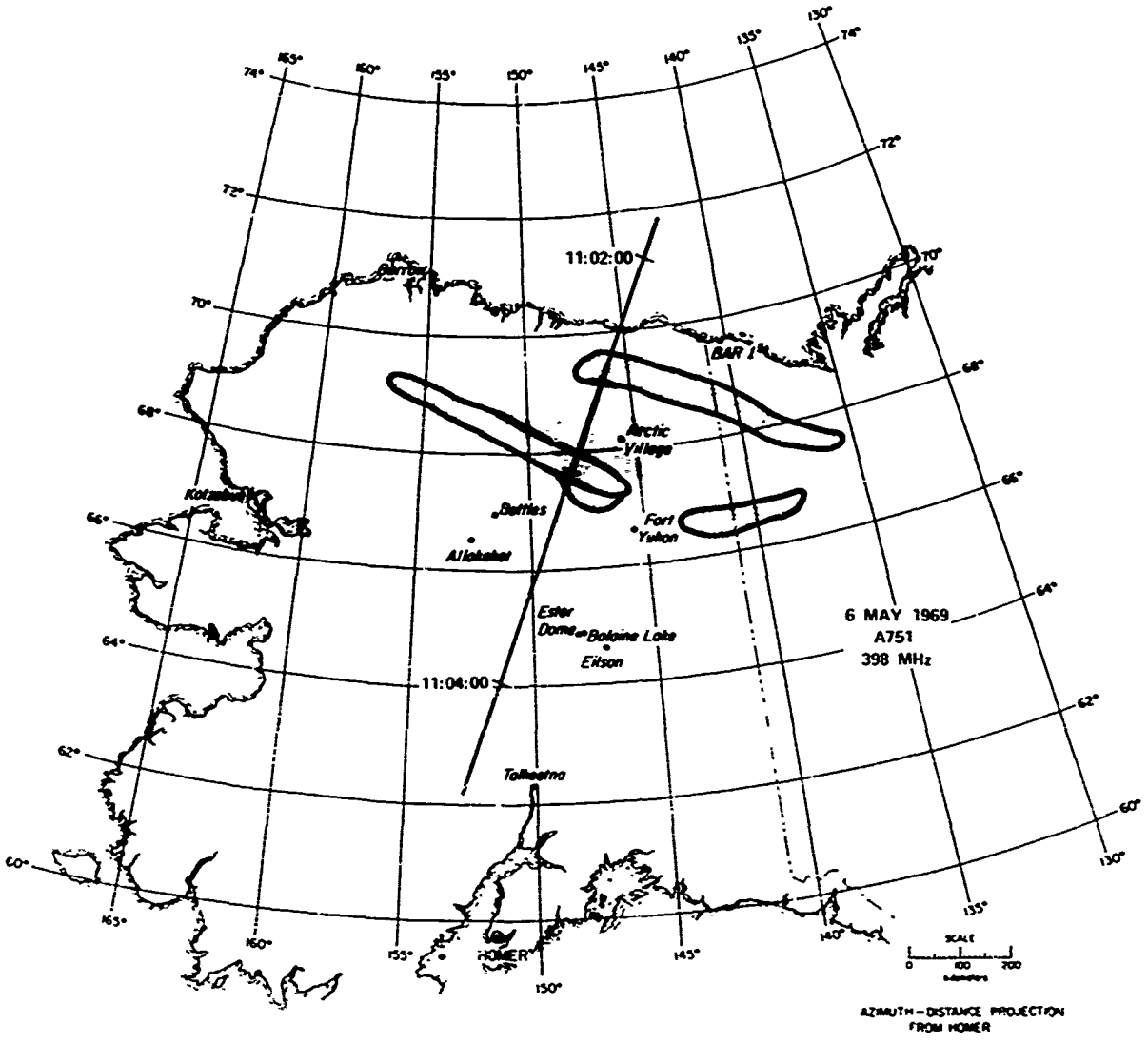

FIGURE 4.A.8 MAP OF ALASKA SHOWING GROUND PROJECTION OF SATELLITE ORBIT, PRECIPITATING ELECTRON ENERGY FLUX ALONG THE ORBIT, AND RADAR AURORAL DISTRIBUTIONS DURING PASS A751

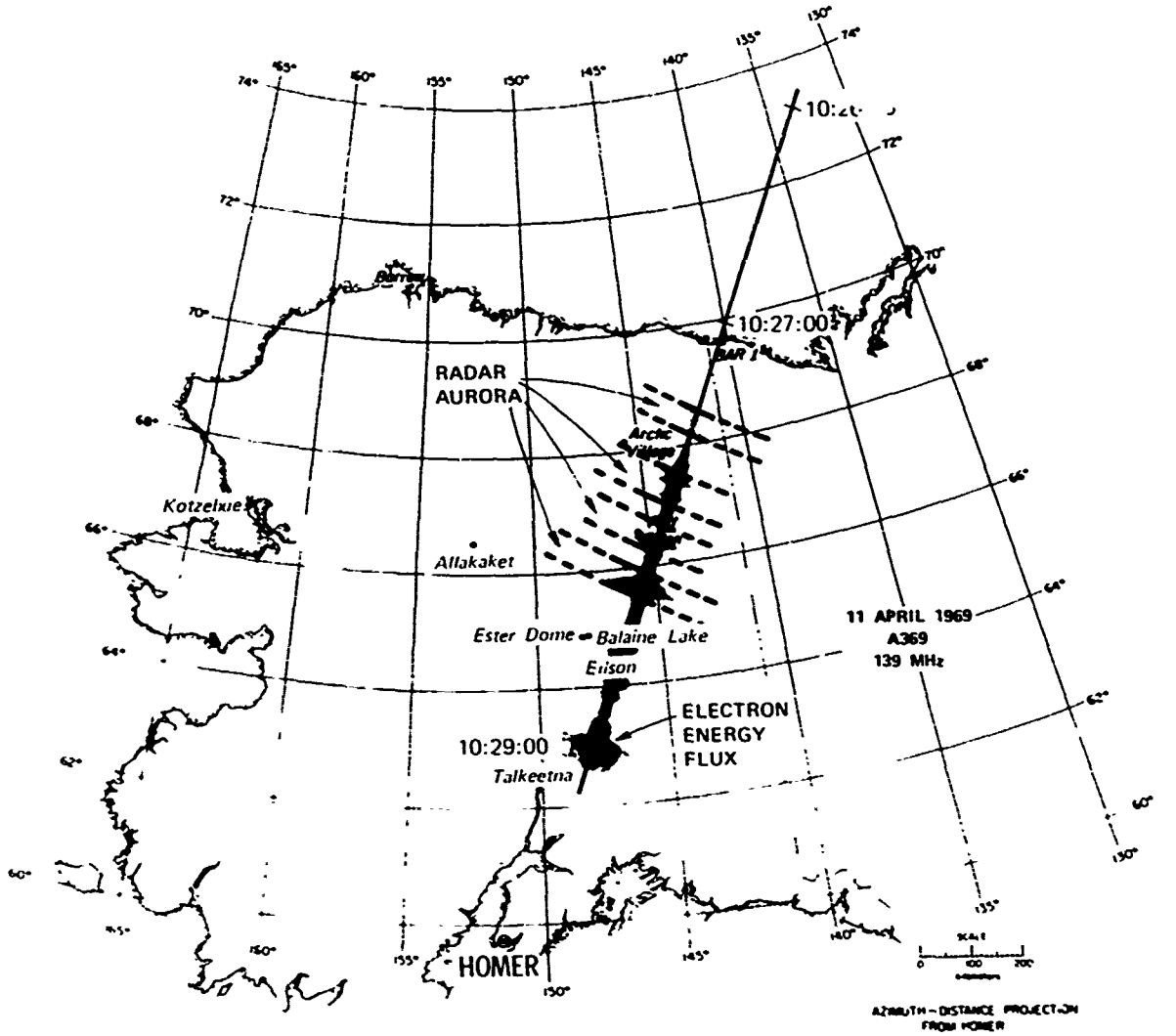

FIGURE 4.A.9 MAP OF ALASKA SHOWING GROUND PROJECTION OF SATELLITE ORBIT, PRECIPITATING ELECTRON ENERGY FLUX ALONG THE ORBIT, AND RADAR AURORAL DISTRIBUTIONS DURING PASS A369

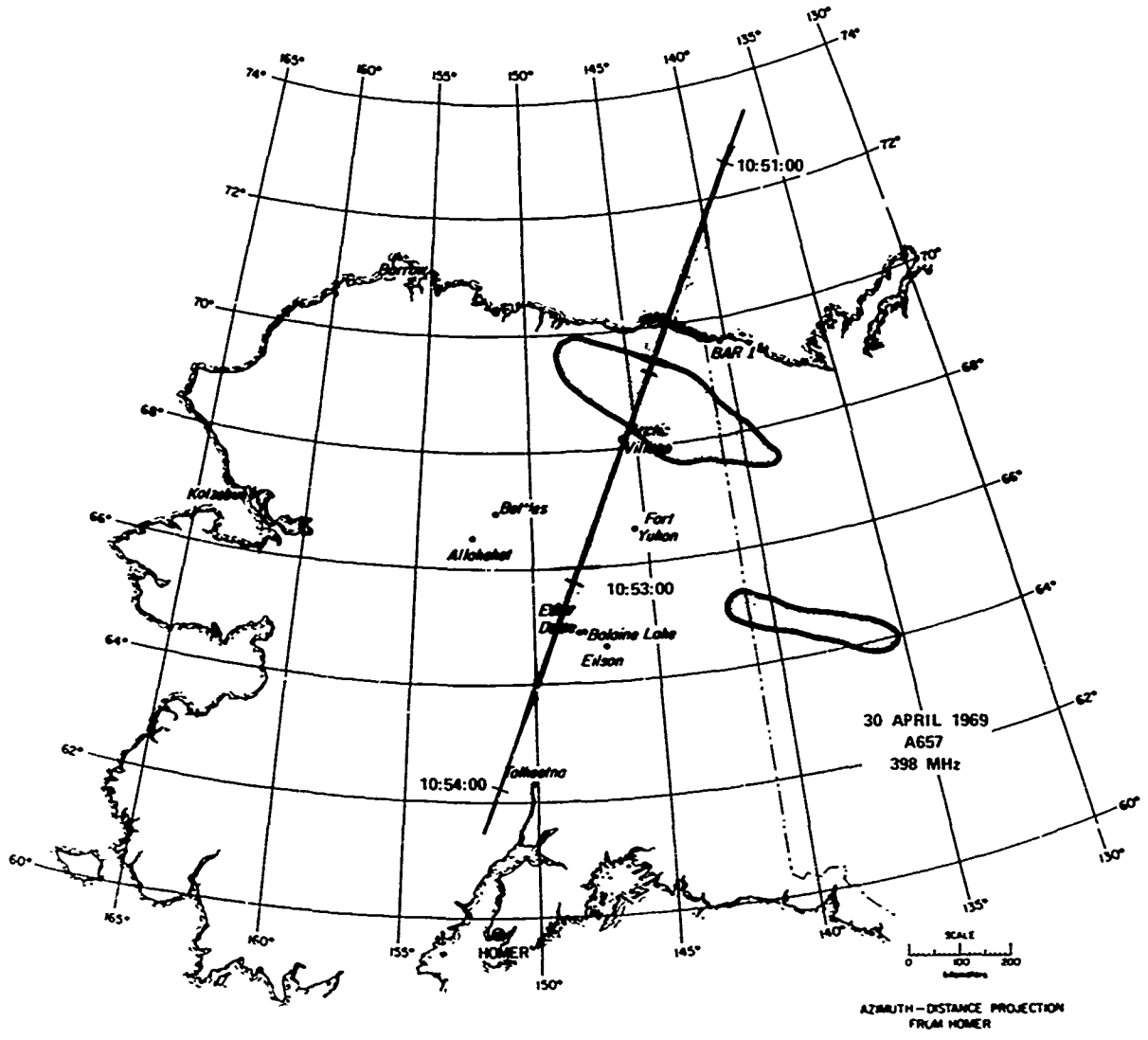

FIGURE 4.A.10 MAP OF ALASKA SHOWING GROUND PROJECTION OF SATELLITE ORBIT, PRECIPITATING ELECTRON ENERGY FLUX ALONG THE ORBIT, AND RADAR AURORAL DISTRIBUTIONS DURING PASS A657

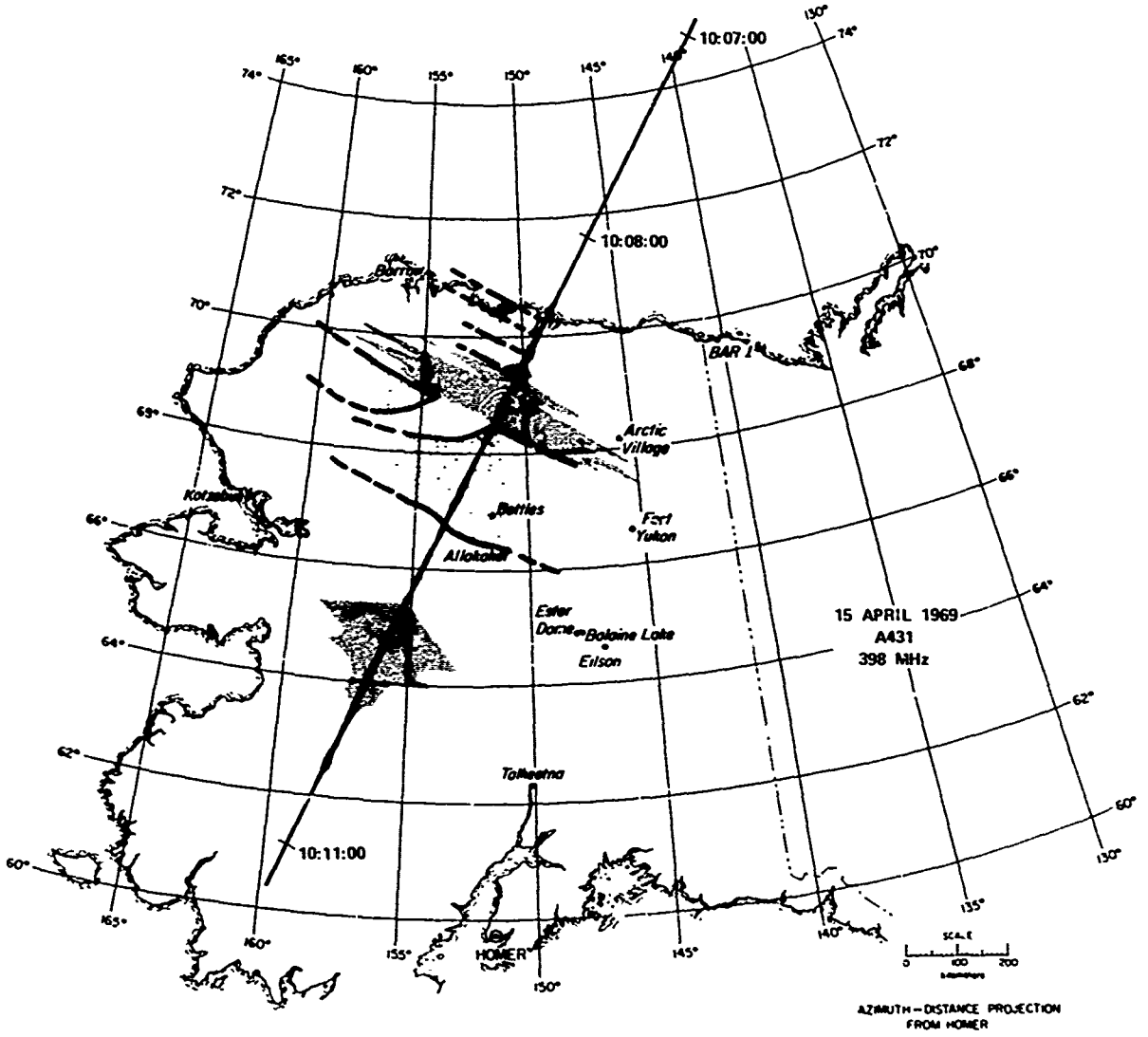

FIGURE 4.A.11 MAP OF ALASKA SHOWING GROUND PROJECTION OF SATELLITE ORBIT, PRECIPITATING ELECTRON ENERGY FLUX ALONG THE ORBIT, AND RADAR AURORAL DISTRIBUTIONS DURING PASS A431

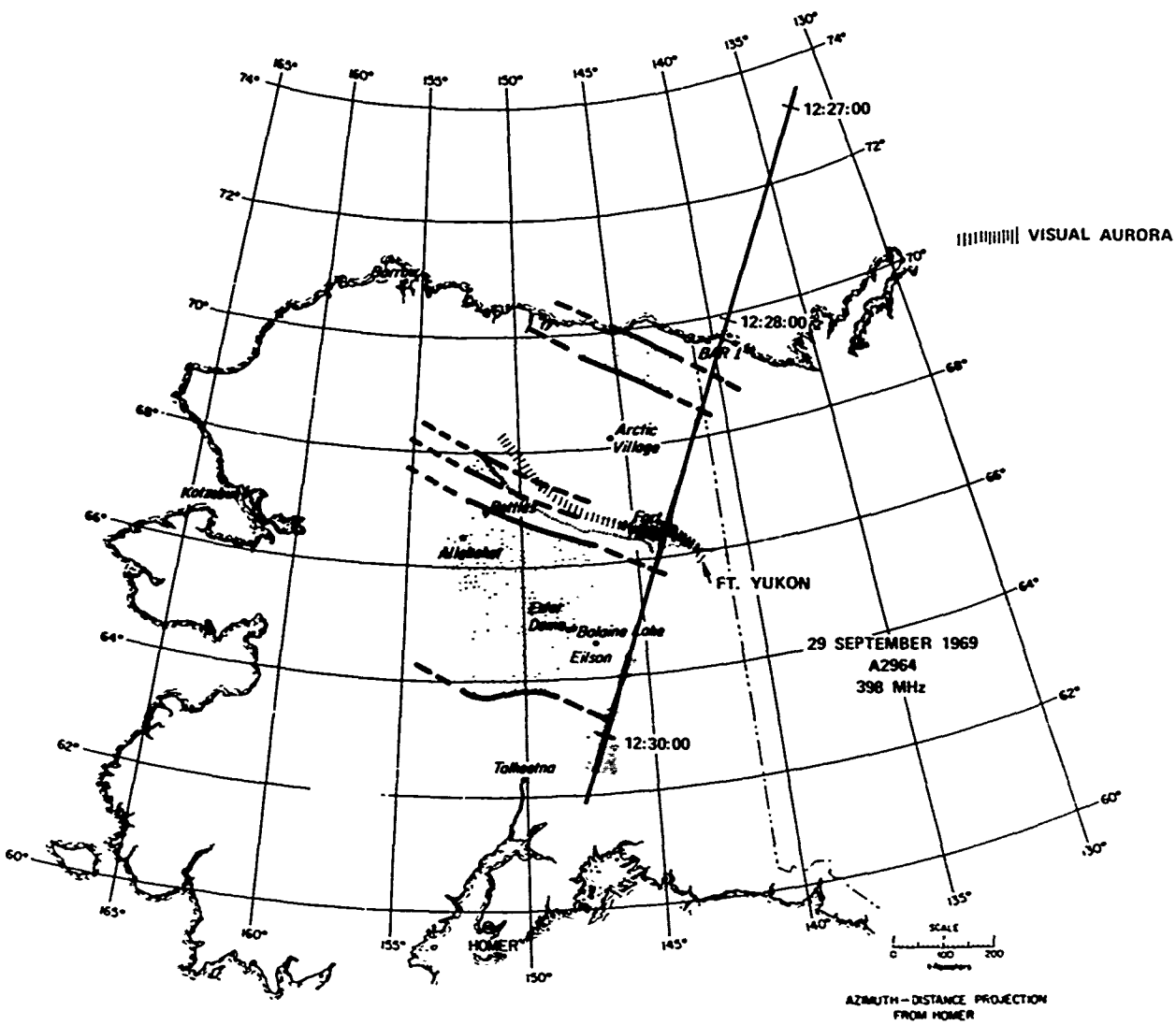

FIGURE 4.A.12 MAP OF ALASKA SHOWING GROUND PROJECTION OF SATELLITE ORBIT. PRECIPITATING ELECTRON ENERGY FLUX ALONG THE ORBIT, AND RADAR AURORAL DISTRIBUTIONS DURING PASS A2964

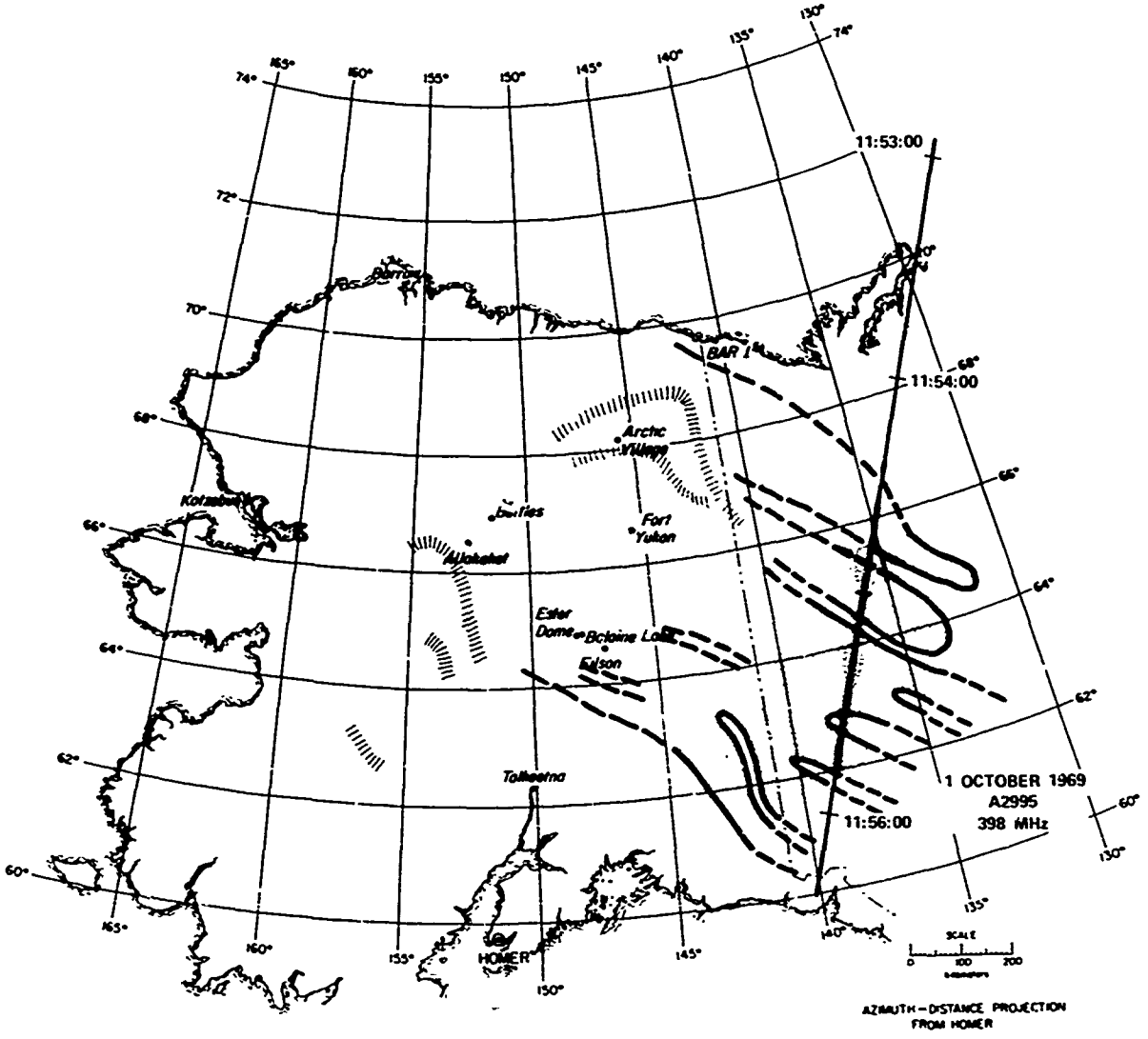

FIGURE 4.A.13 MAP OF ALASKA SHOWING GROUND PROJECTION OF SATELLITE ORBIT, PRECIPITATING ELECTRON ENERGY FLUX ALONG THE ORBIT, AND RADAR AURORAL DISTRIBUTIONS DURING PASS A2995

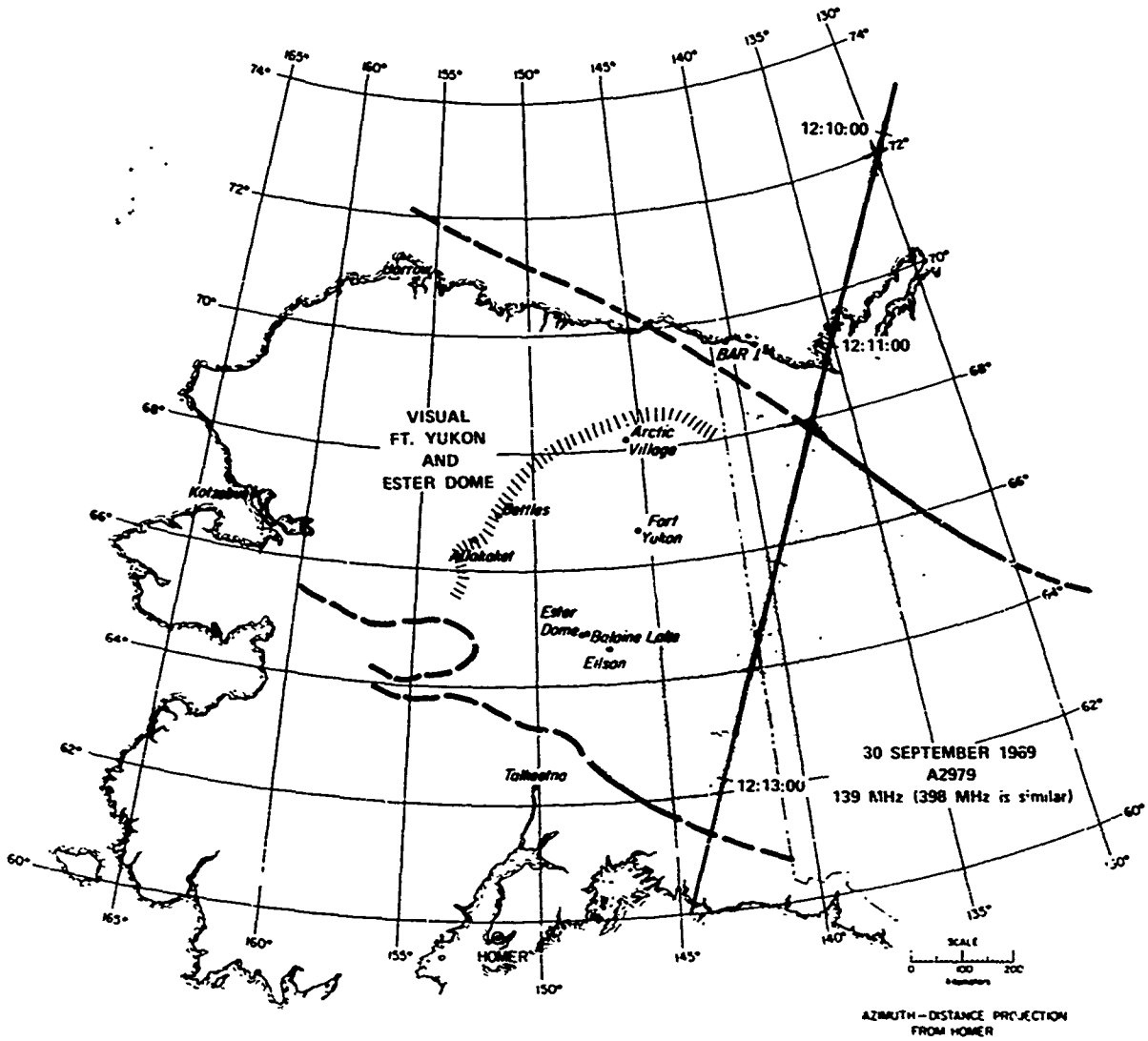

FIGURE 4.4.14 MAP OF ALASKA SHOWING GROUND PROJECTION OF SATELLITE ORBIT, PRECIPITATING ELECTRON ENERGY FLUX ALONG THE ORBIT, AND RADAR AURORAL DISTRIBUTIONS DURING PASS A2979

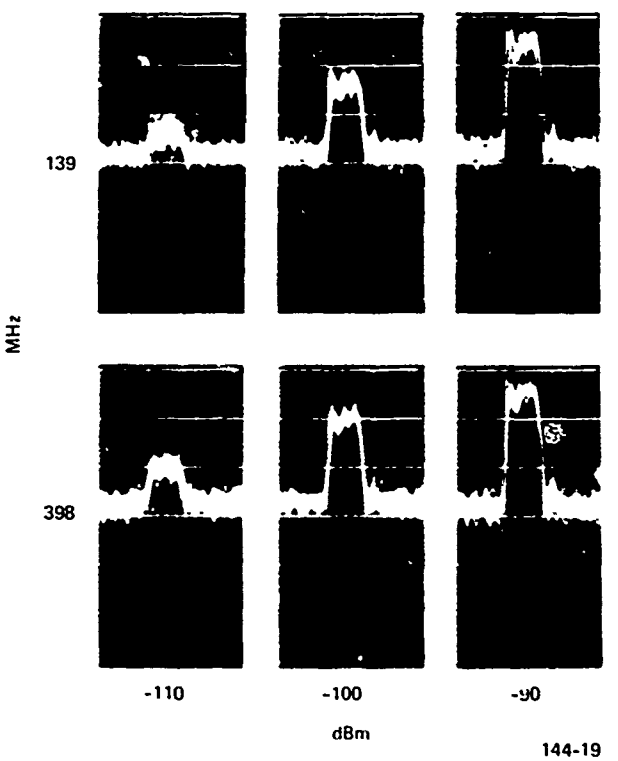

FIGURE 4.B.0 CALIBRATION OF RADAR A-SCOPE TRACES FOR USE WITH FIGURES 4.B.1 THROUGH 4.B.14

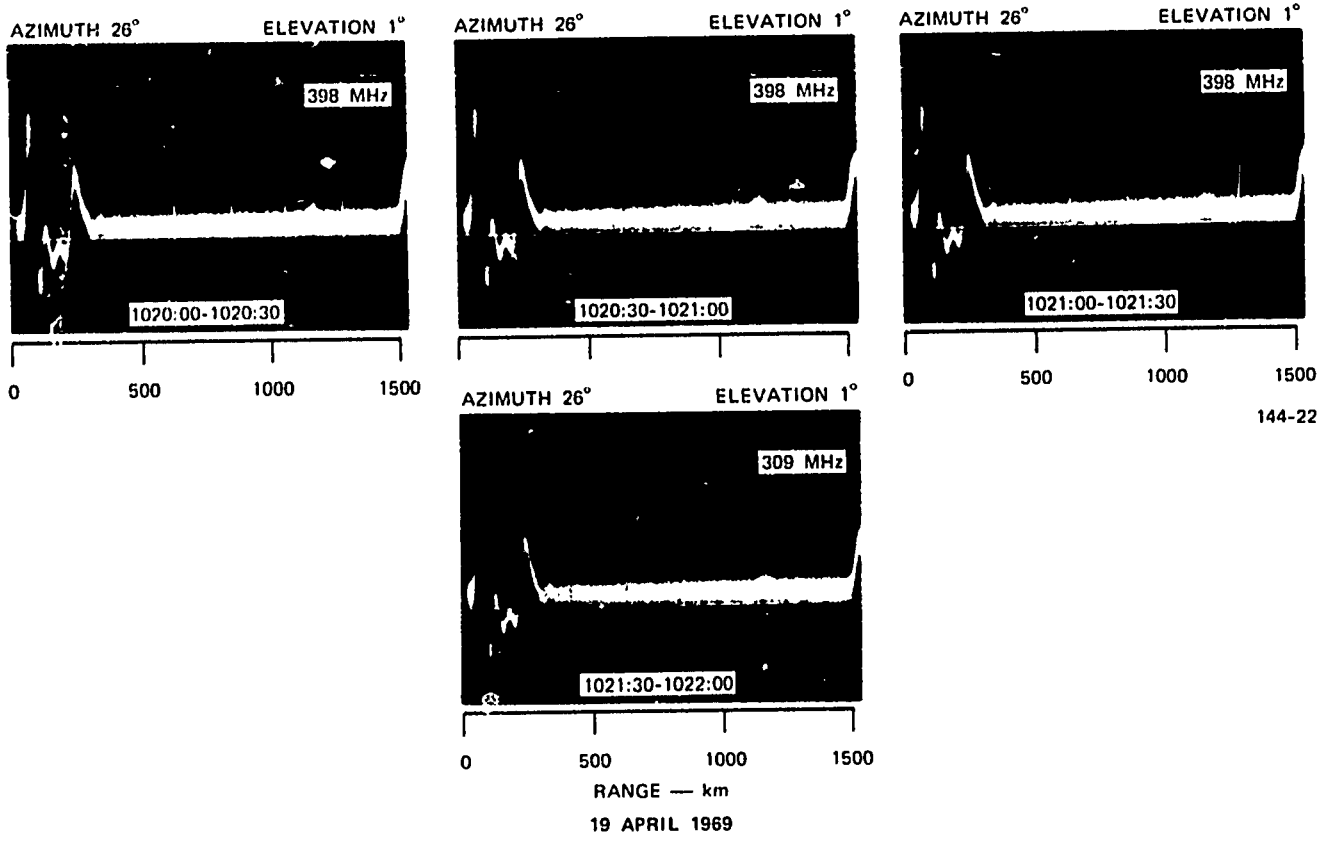

FIGURE 4.B.1 RADAR A-SCOPE RECORDS FOR SATELLITE PASS A518

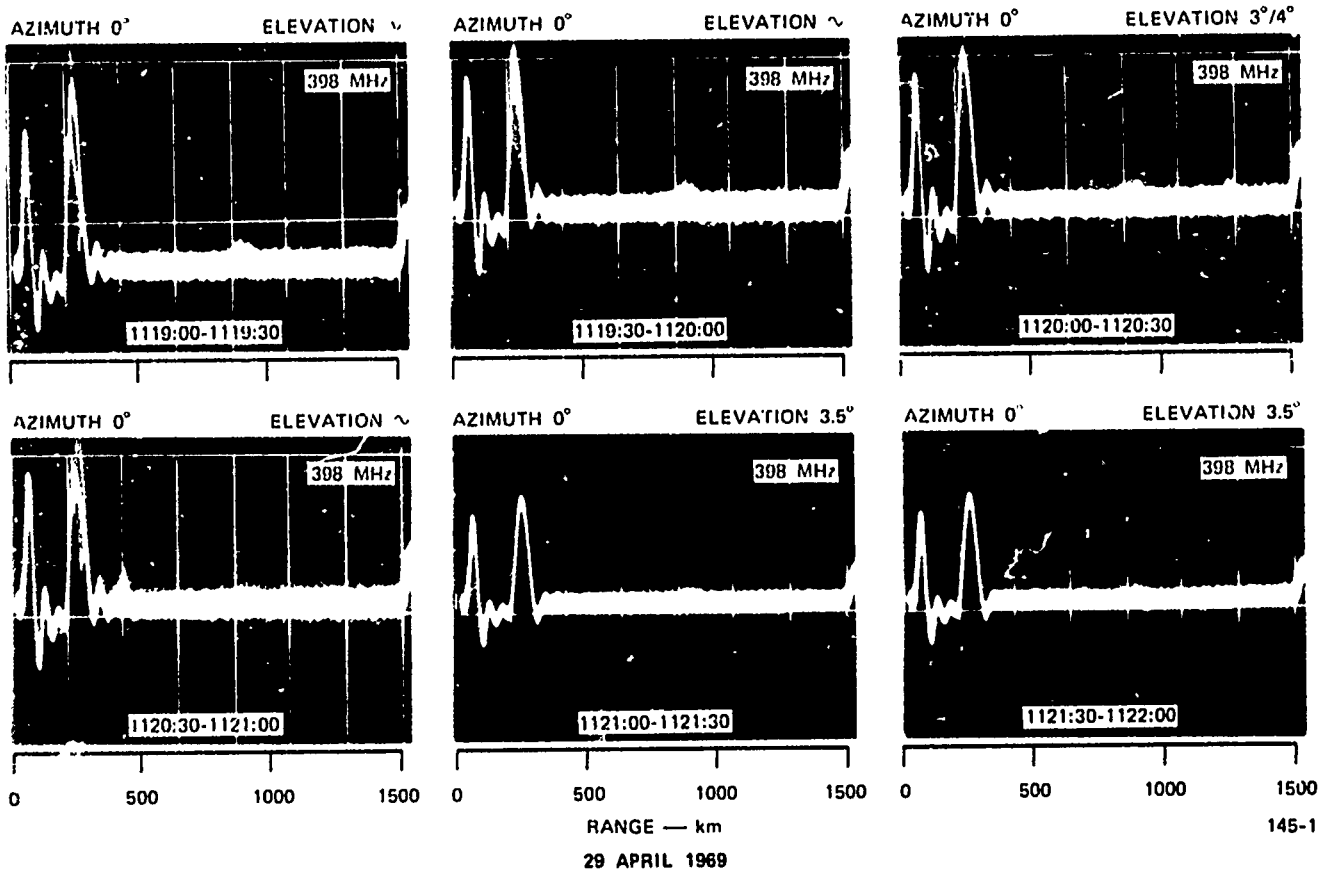

FIGURE 4.B.2 RADAR A-SCOPE RECORDS FOR SATELLITE PASS A641

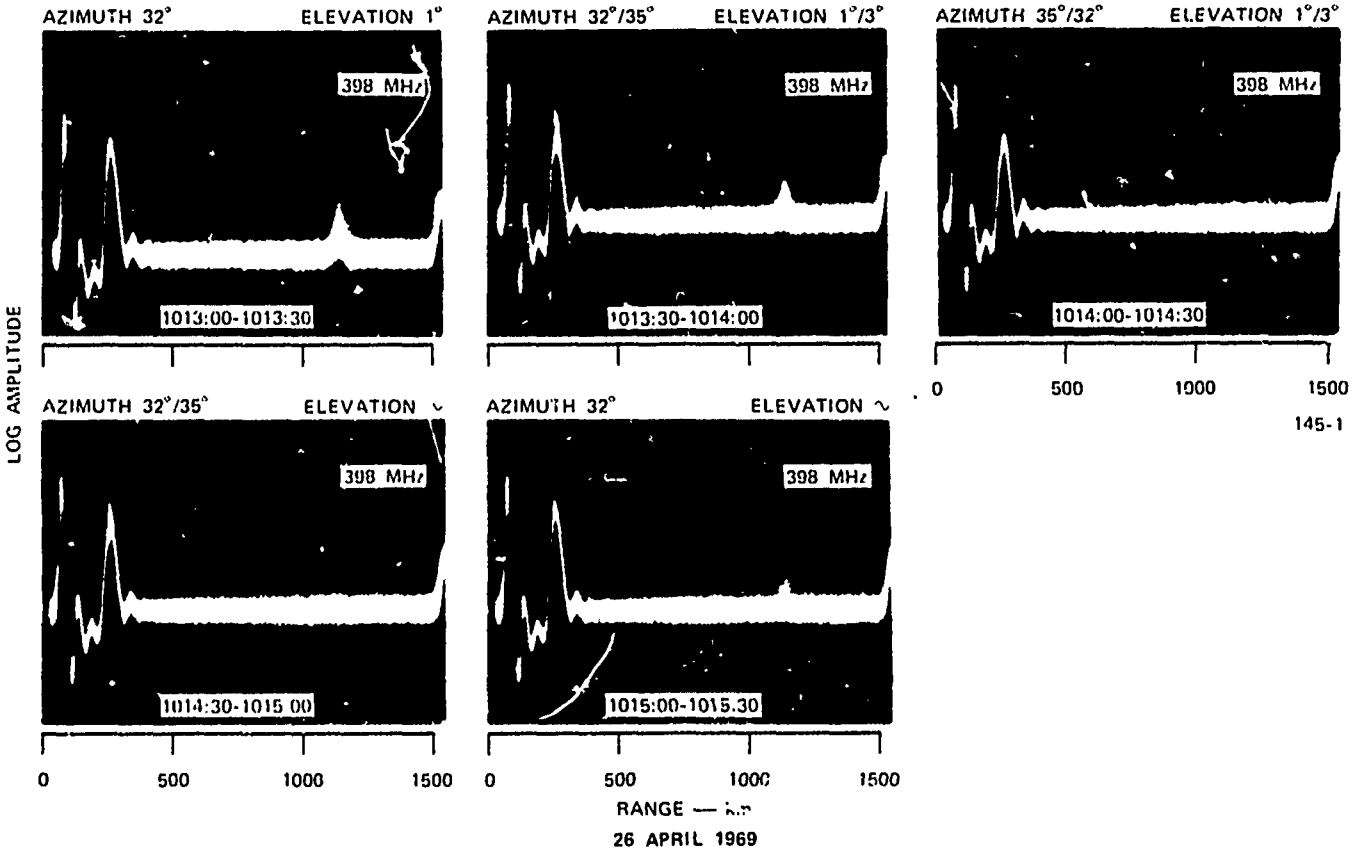

FIGURE 4.8.3 RADAR A-SCOPE RECORDS FOR SATELLITE PASS A624

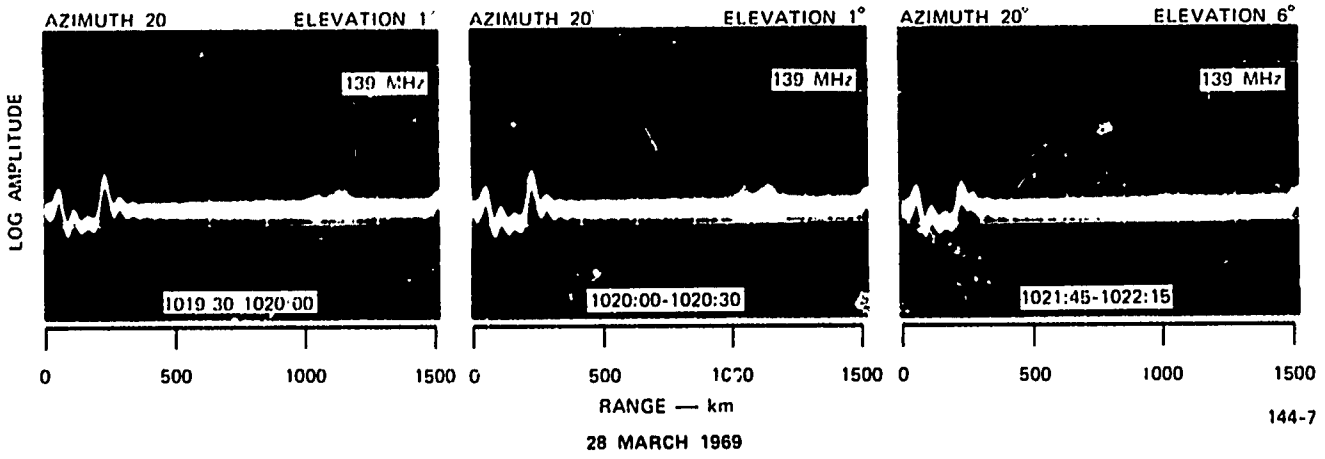

FIGURE 4.B.4 RADAR A-SCOPE RECORDS FOR SATELLITE PASS A157

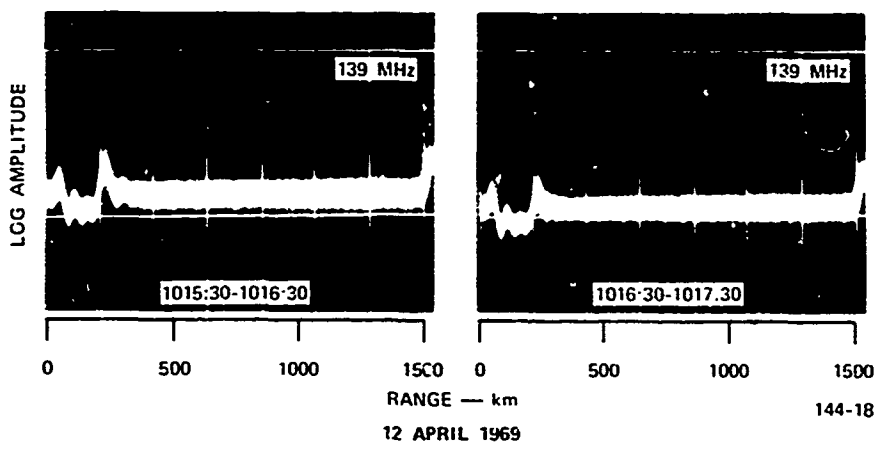

FIGURE 4.B.5 RADAR A-SCOPE RECORDS FOR SATELLITE PASS A388

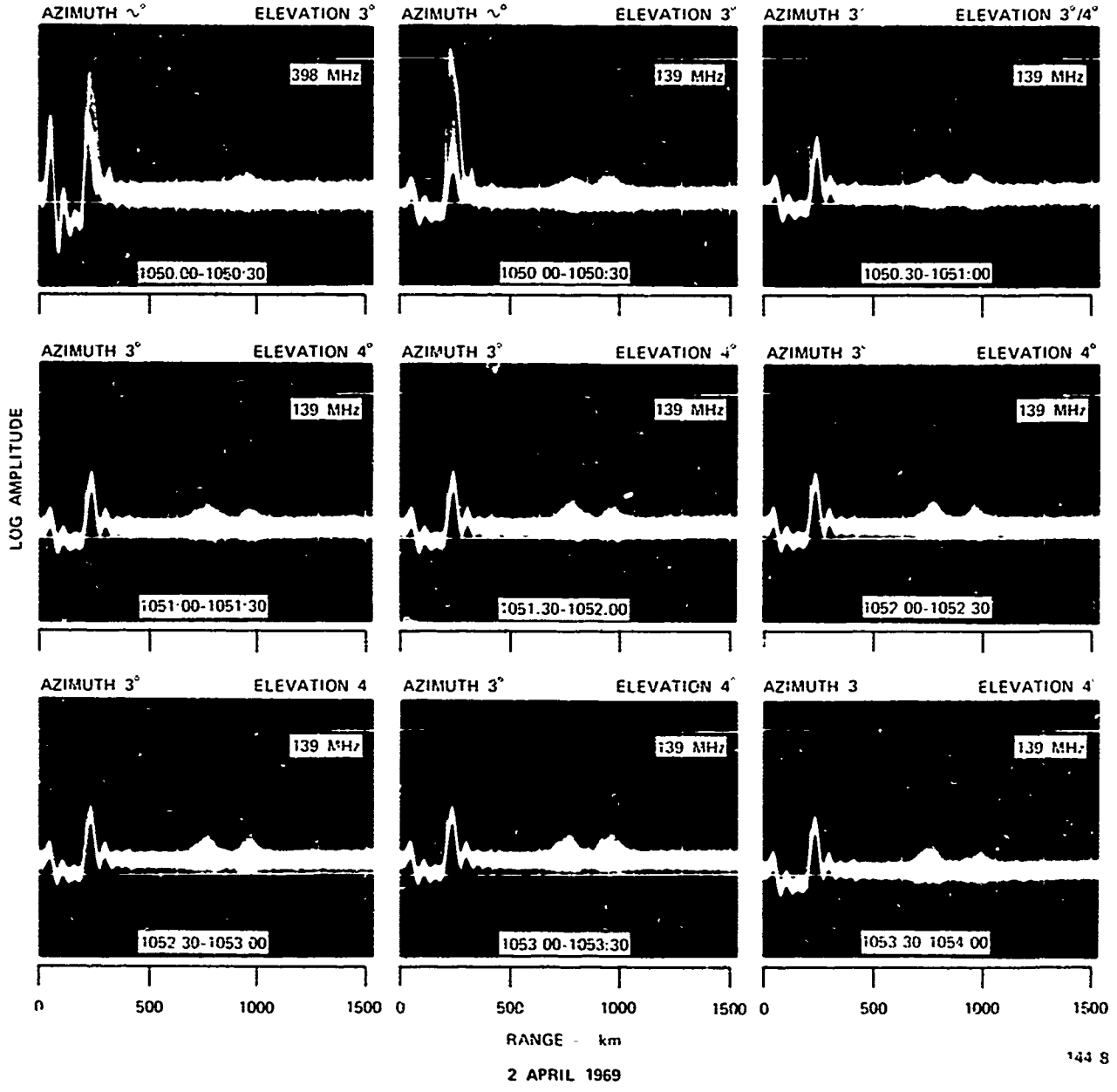

FIGURE 4.B.6 RADAR A-SCOPE RECORDS FOR SATELLITE PASS A232

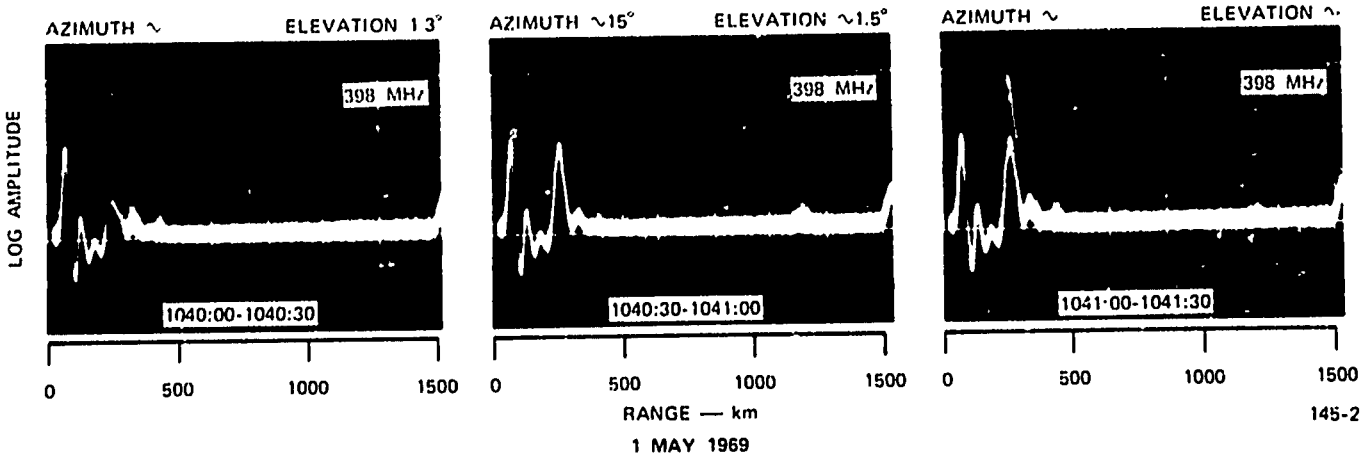

FIGURE 4.B.7 RADAR A-SCOPE RECORDS FOR SATELLITE PASS A676

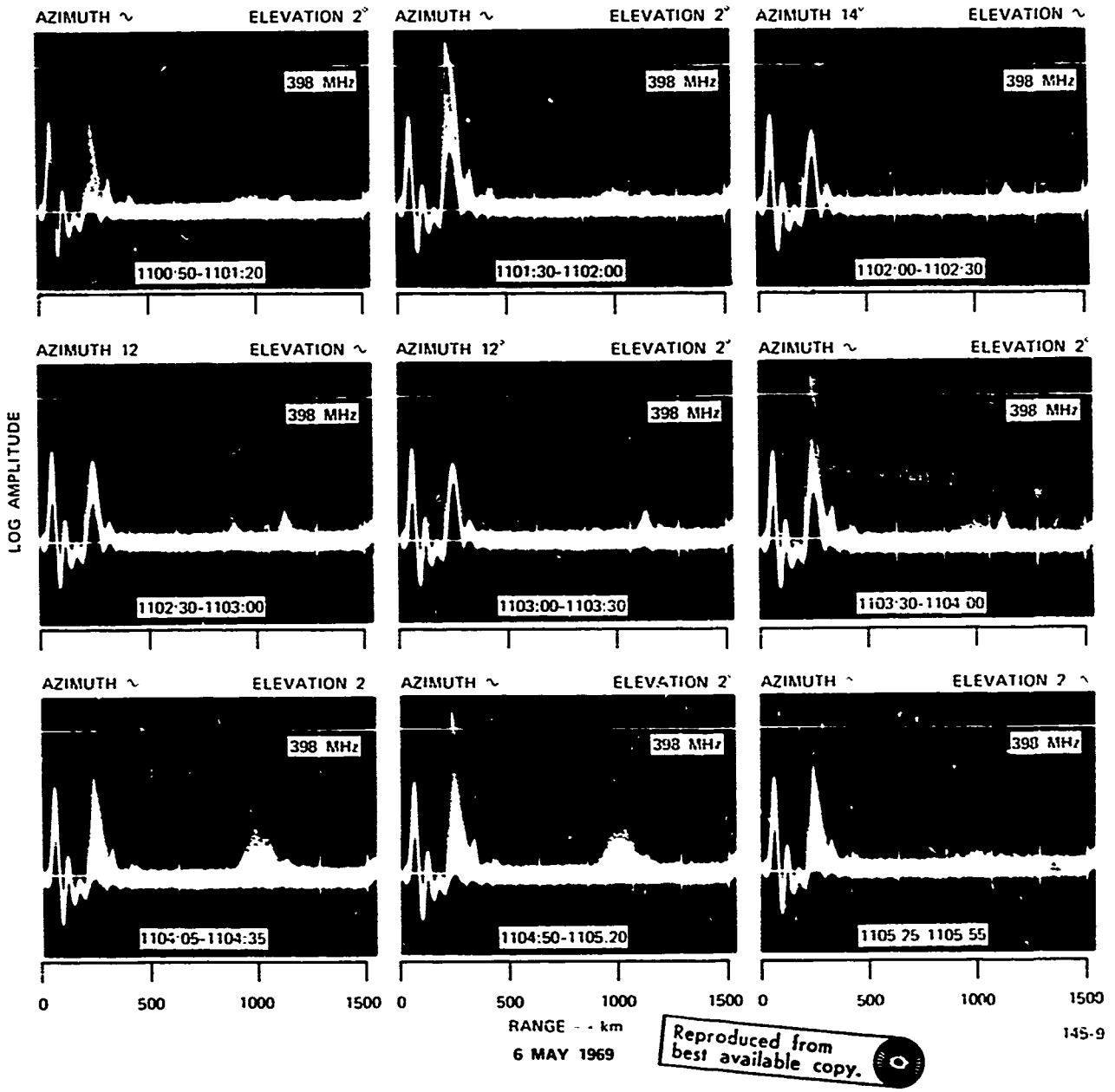

FIGURE 4.B.8 RADAR A-SCOPE RECORDS FOR SATELLITE PASS A751

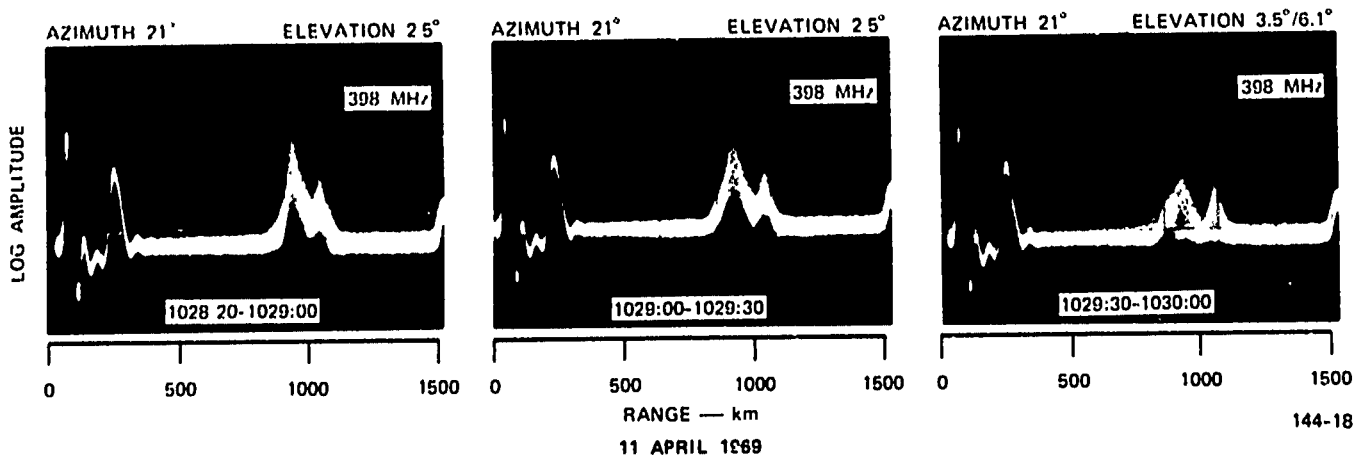

FIGURE 4.B.9 RADAR A-SCOPE RECORDS FOR SATELLITE PASS A369

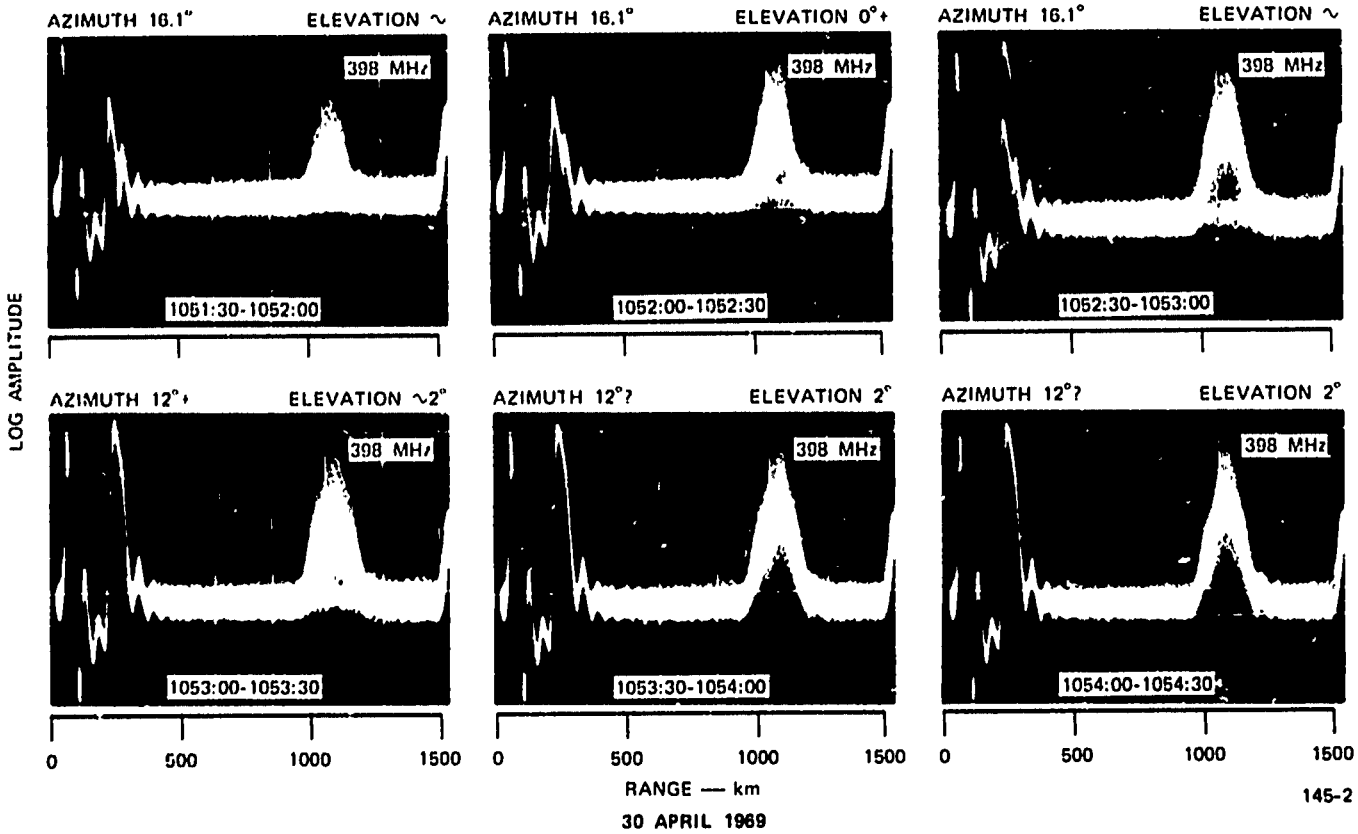

FIGURE 4.B.10 RADAR A-SCOPE RECORDS FOR SATELLITE PASS A657

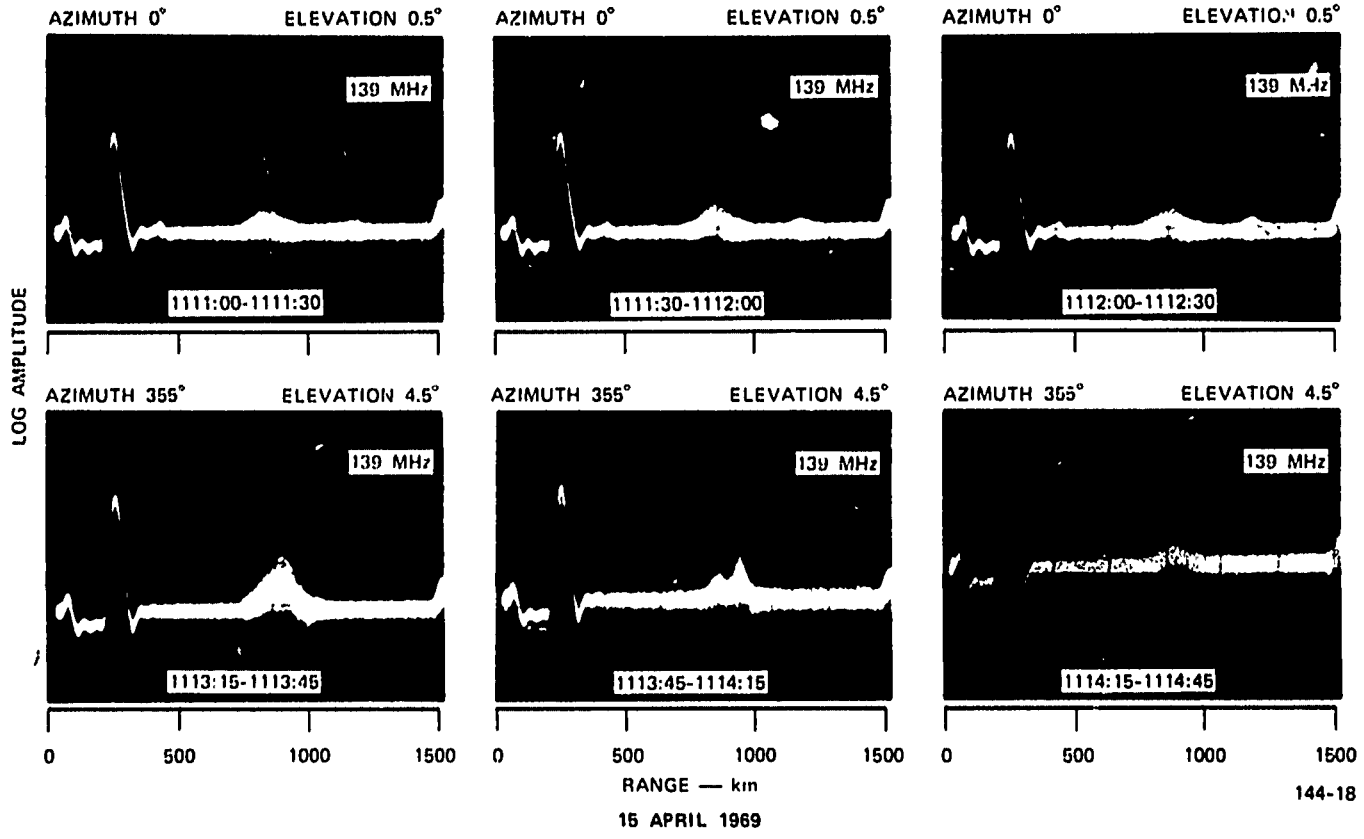

FIGURE 4.B.11 RADAR A-SCOPE RECORDS FOR SATELLITE PASS A431

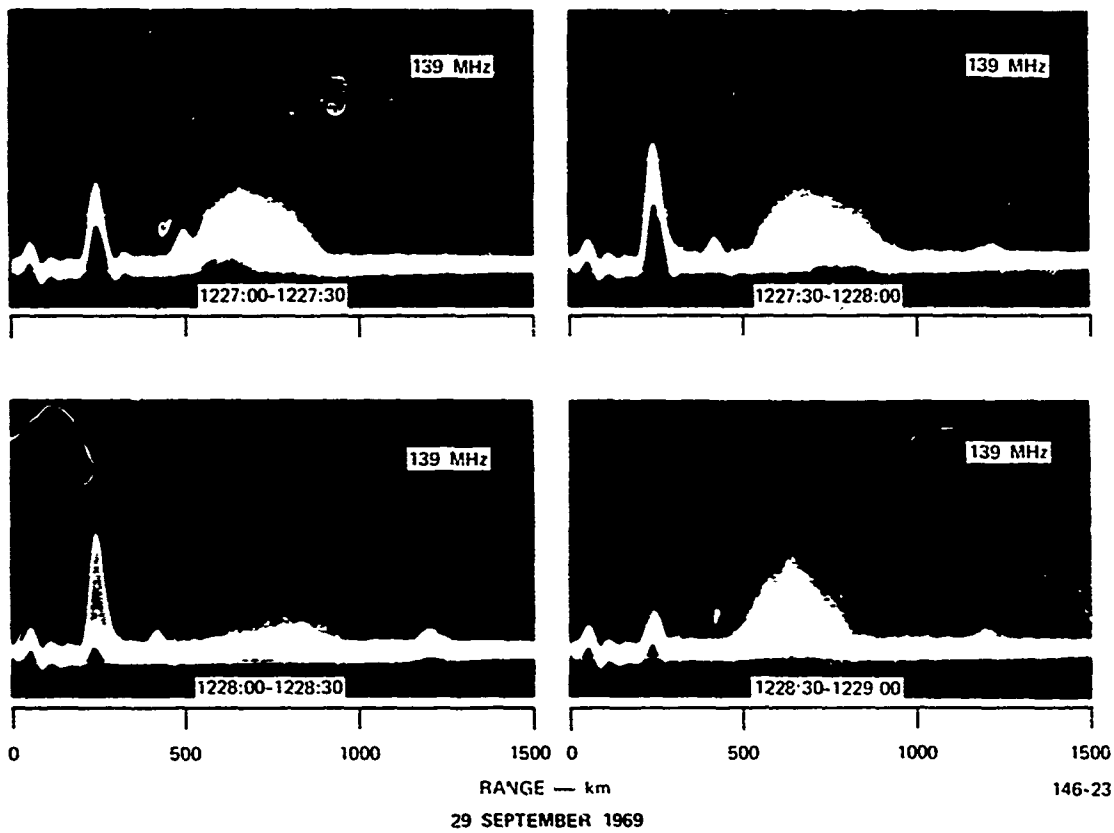

FIGURE 4.B.12 RADAR A-SCOPE RECORDS FOR SATELLITE PASS A2964

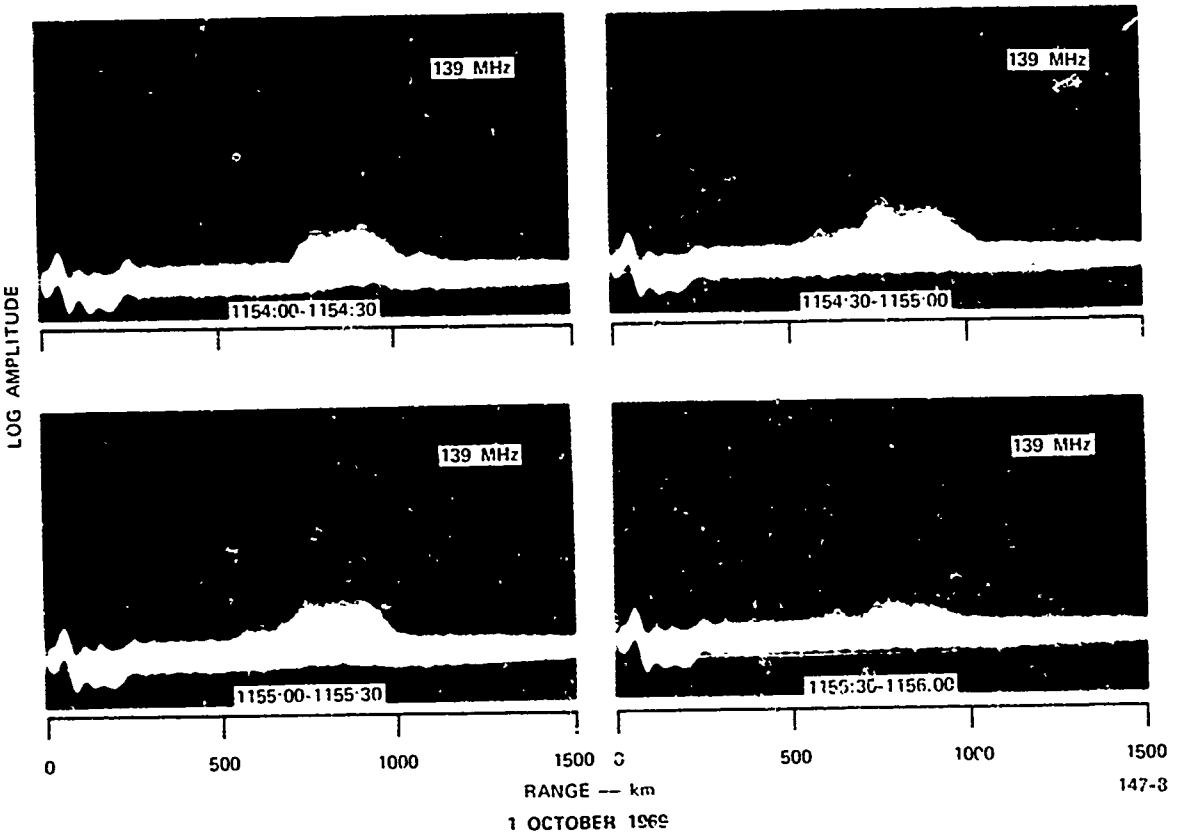

FIGURE 4.B.13 RADAR A-SCOPE RECORDS FOR SATELLITE PASS A2995

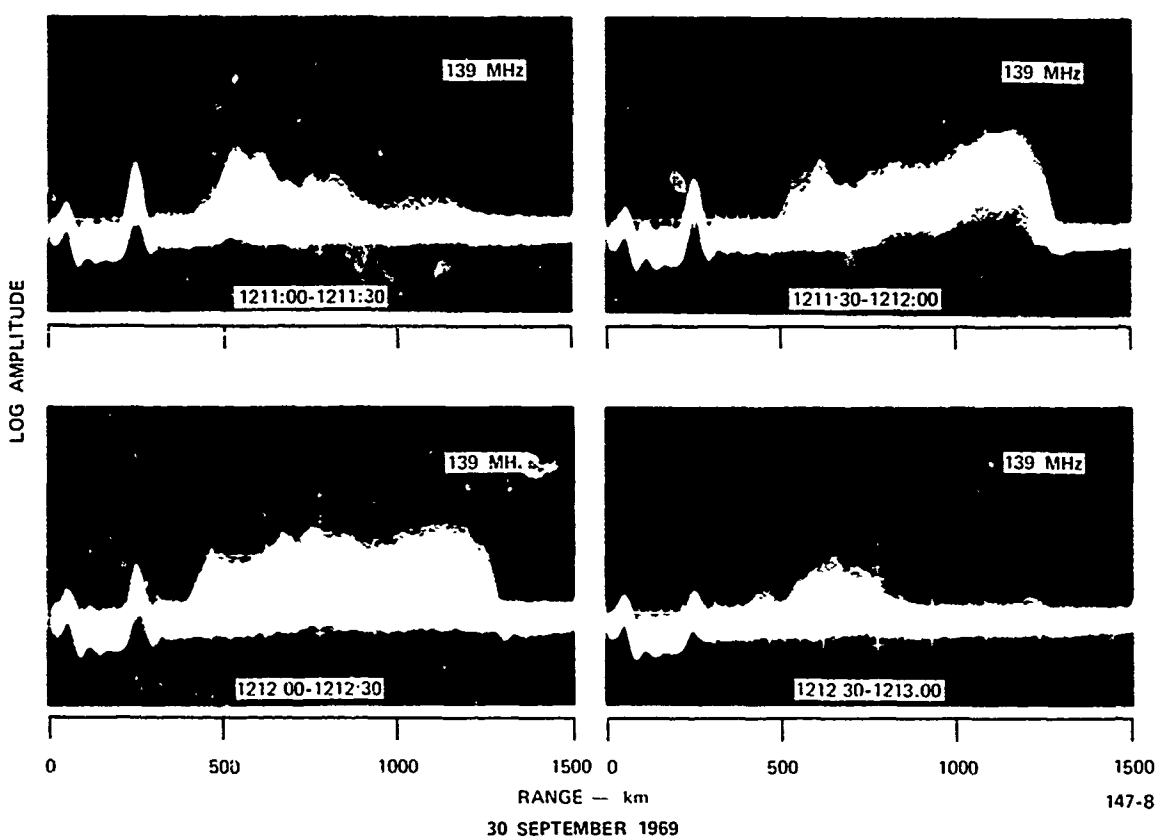

FIGURE 4.B.14 RADAR A-SCOPE RECORDS FOR SATELLITE PASS A2979

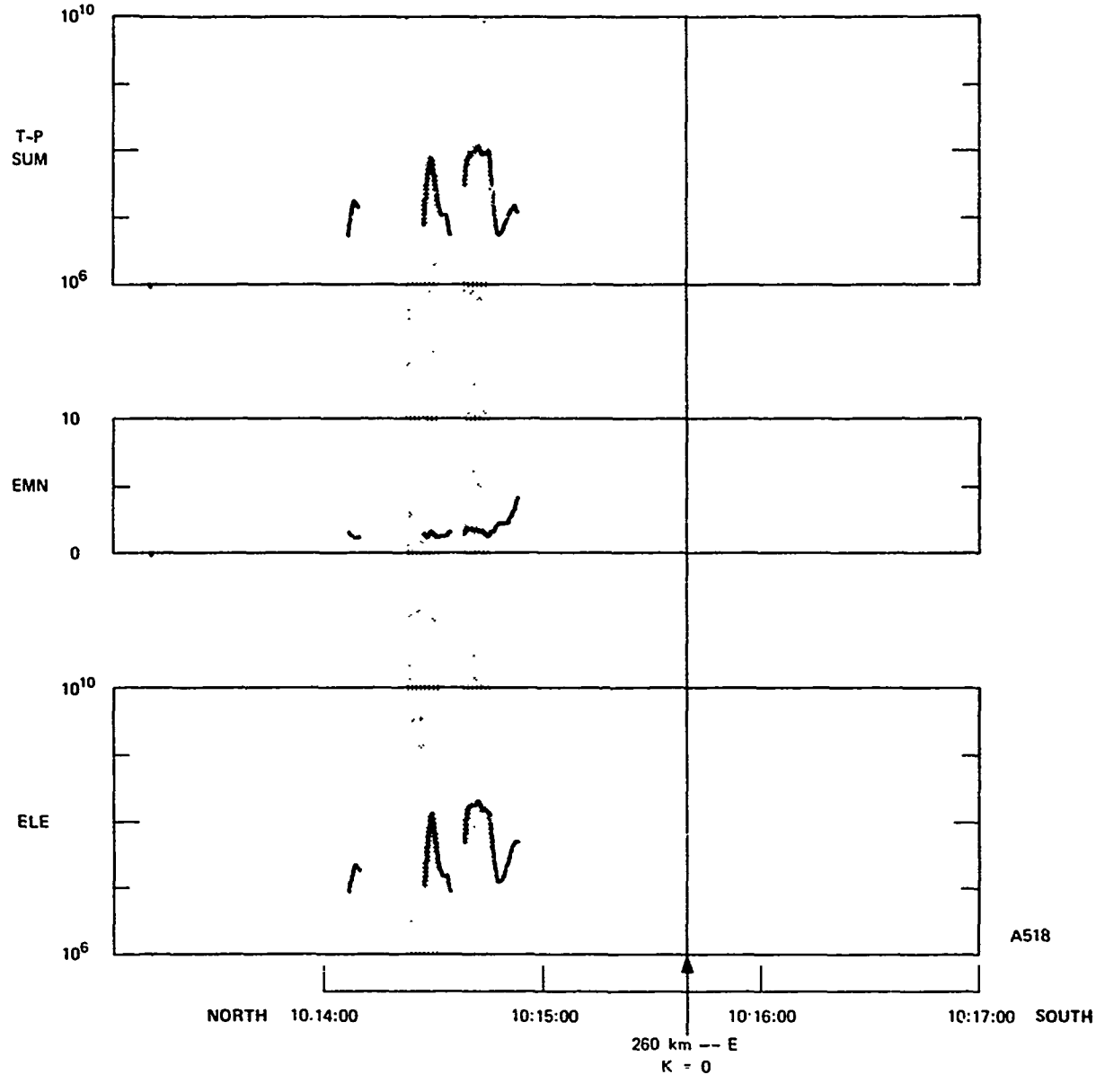

FIGURE 4.C.1 PRECIPITATING ELECTRON NUMBER FLUX (TSUM), AVERAGE ENERGY (EMN), AND ENERGY FLUX (ELE) versus UNIVERSAL TIME FOR SATELLITE PASS A518

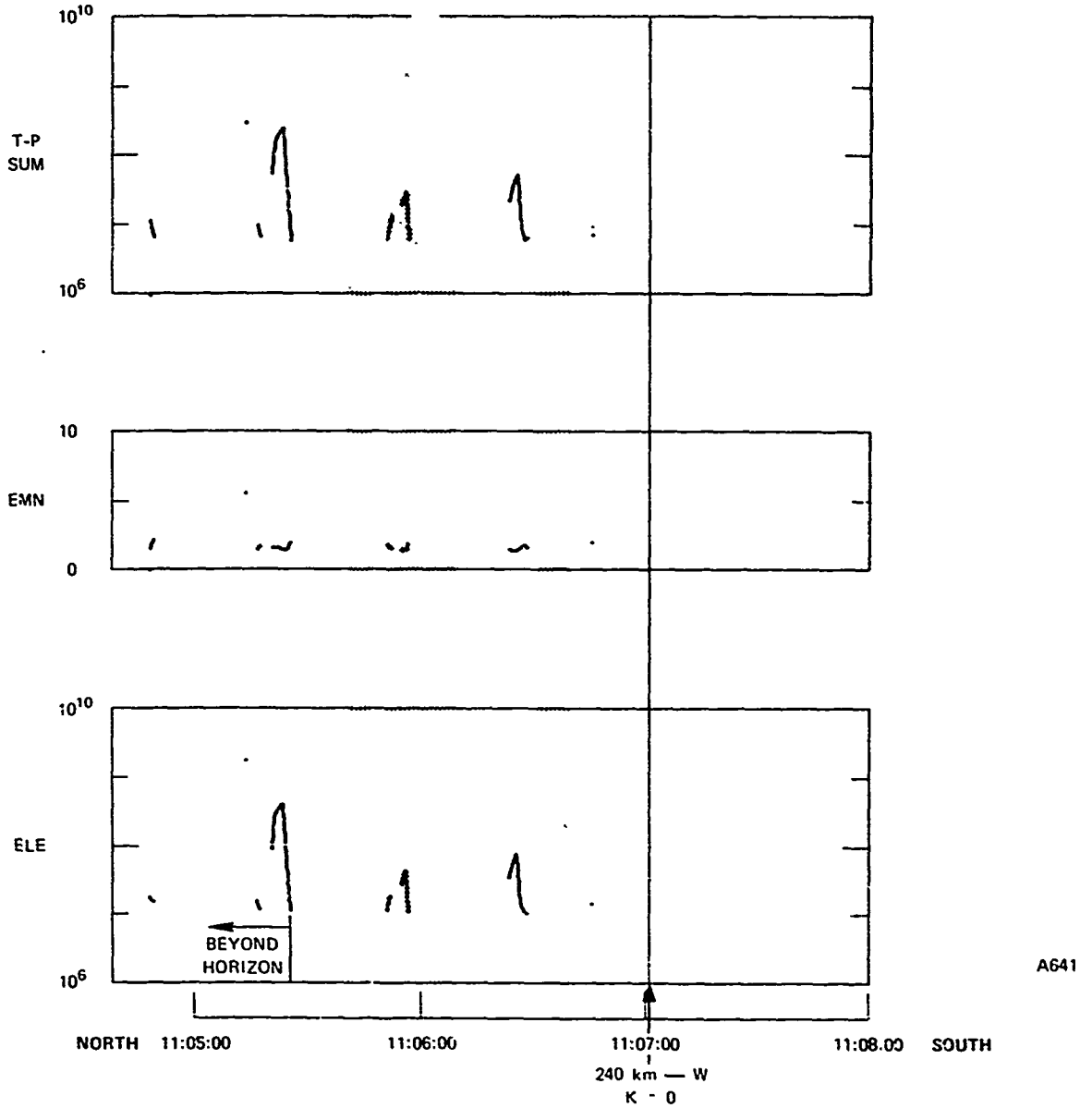

FIGURE 4.C.2 PRECIPITATING ELECTRON NUMBER FLUX (TSUM), AVERAGE ENERGY (EMN), AND ENERGY FLUX (ELE) versus UNIVERSAL TIME FOR SATELLITE PASS A641

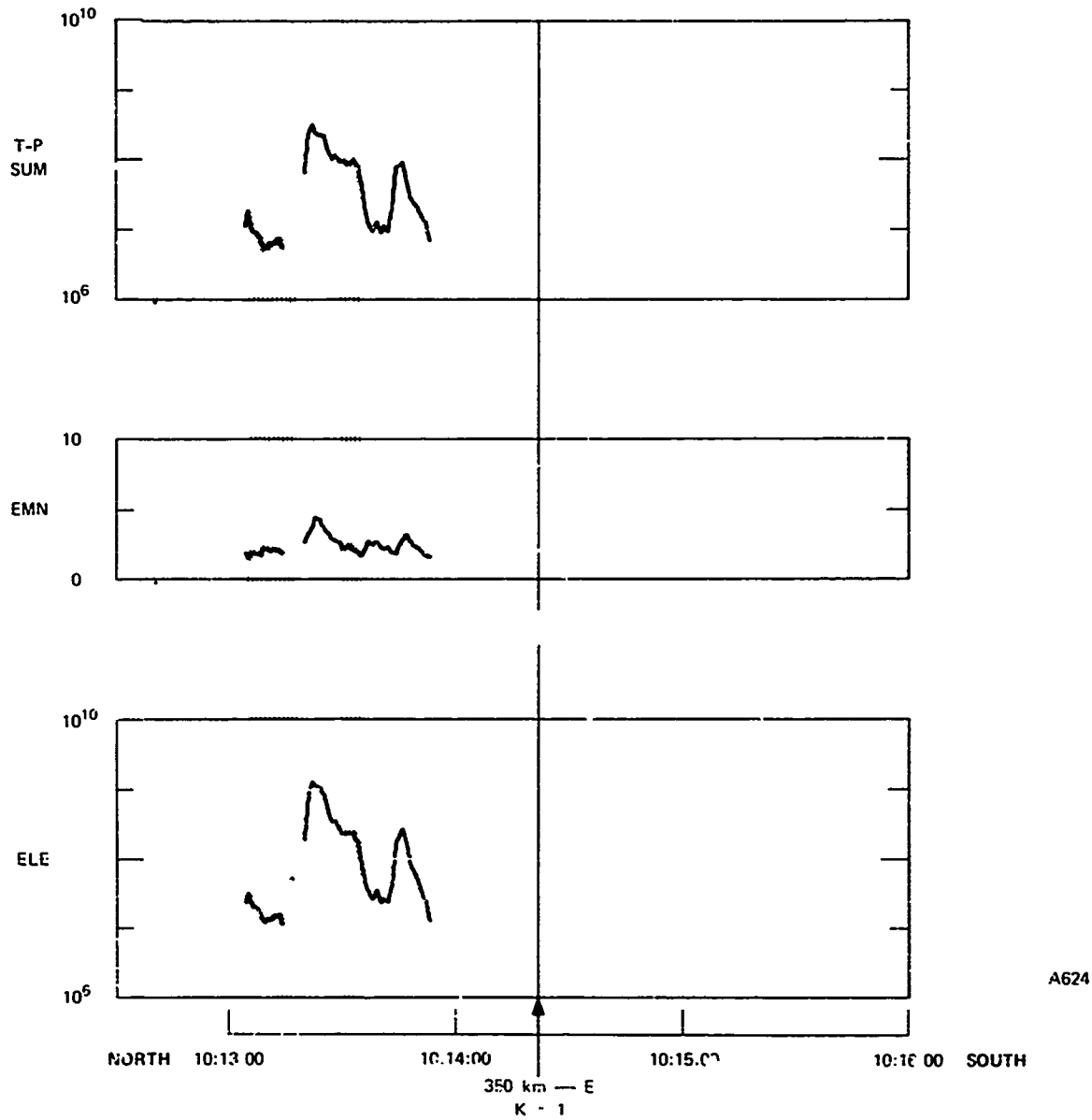

FIGURE 4.C.3 PRECIPITATING ELECTRON NUMBER FLUX (TSUM), AVERAGE ENERGY (EMN), AND ENERGY FLUX (ELE) versus UNIVERSAL TIME FOR SATELLITE PASS A624

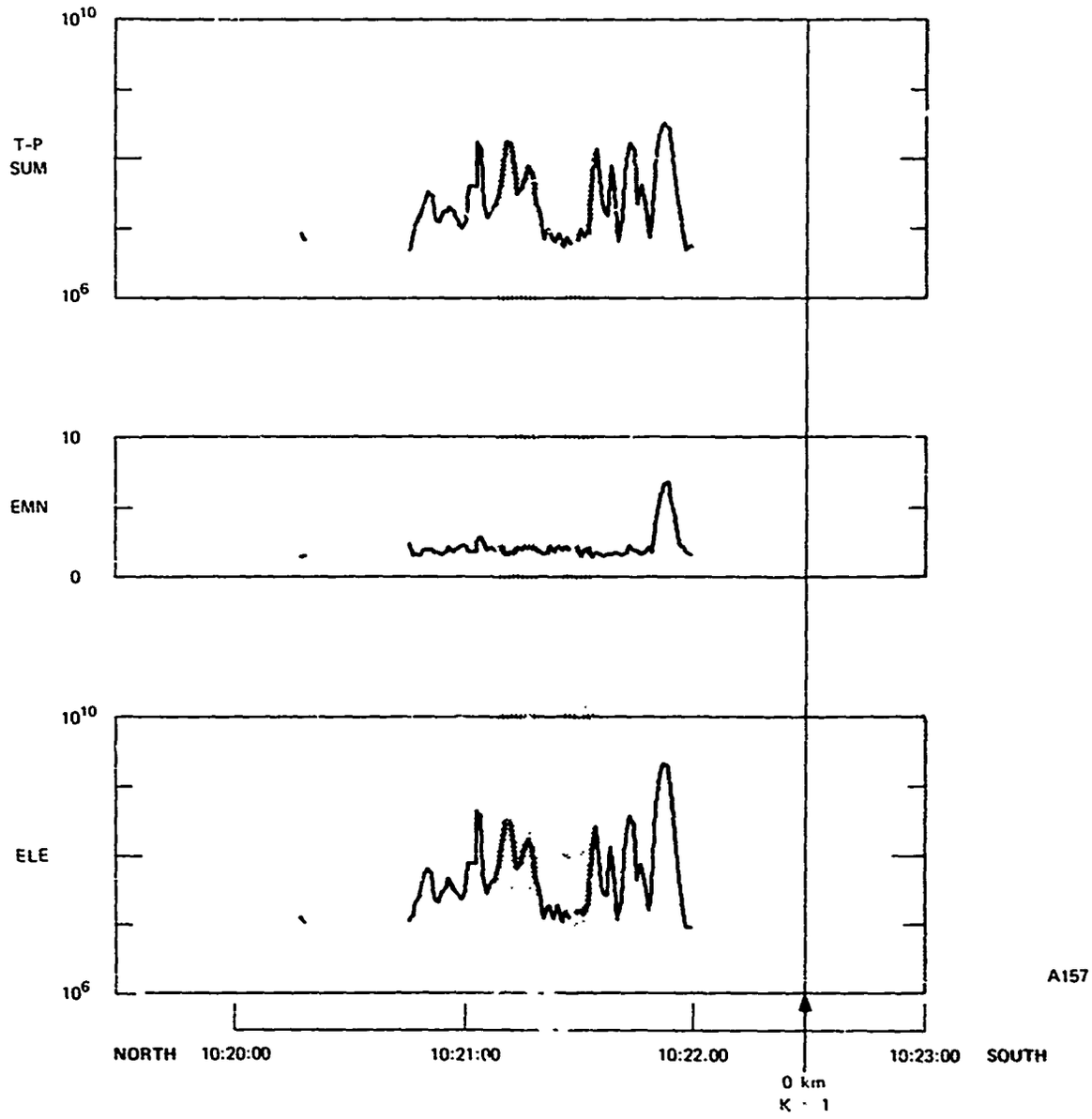

FIGURE 4.C.4 PRECIPITATING ELECTRON NUMBER FLUX (TSUM), AVERAGE ENERGY (EMN), AND ENERGY FLUX (ELE) versus UNIVERSAL TIME FOP SATELLITE PASS A157

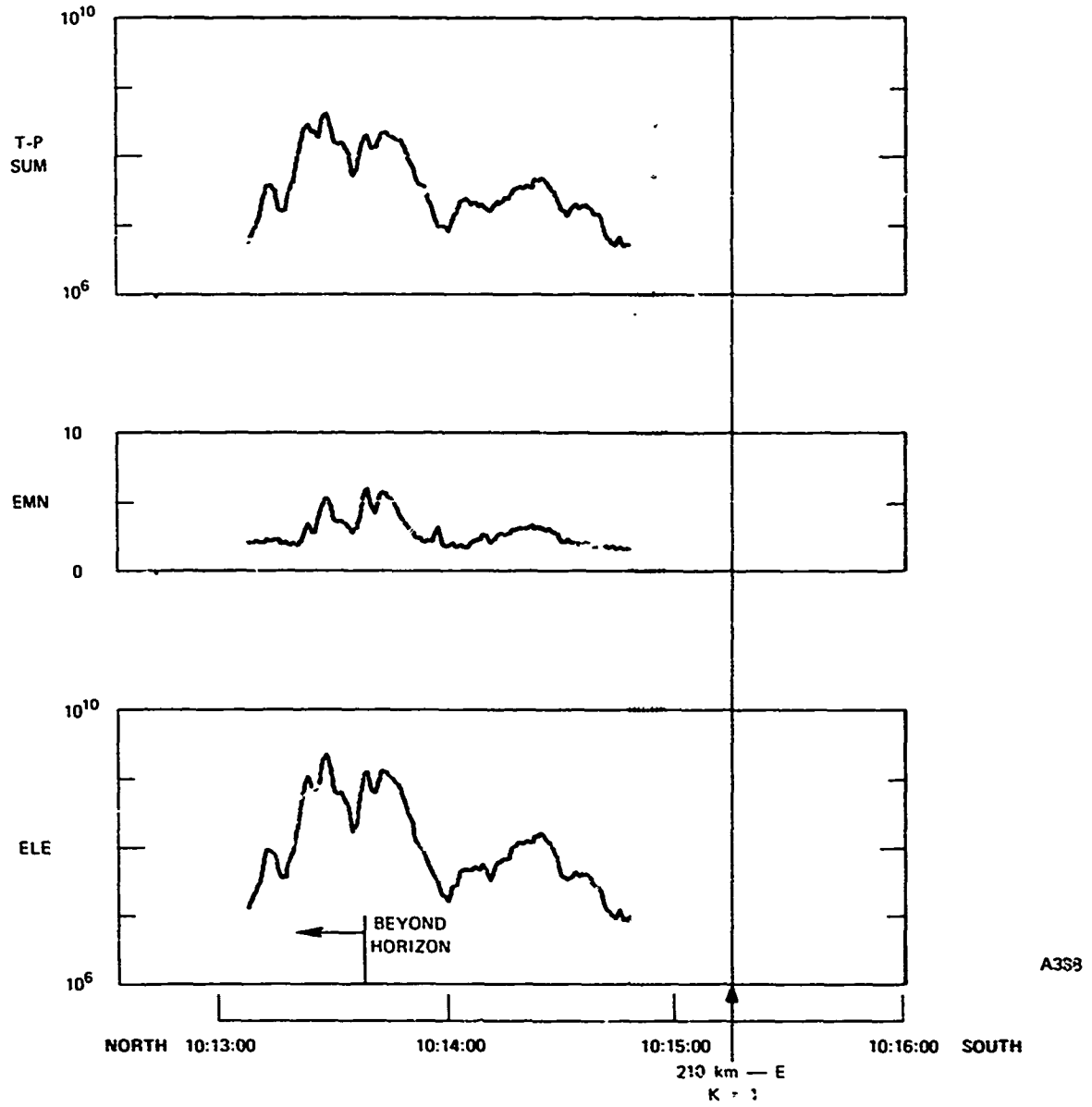

FIGURE 4.C.5 PRECIPITATING ELECTRON NUMBER FLUX (TSUM), AVERAGE ENERGY (EMN), AND ENERGY FLUX (ELE) ve UNIVERSAL TIME FOR SATELLITE PASS A388

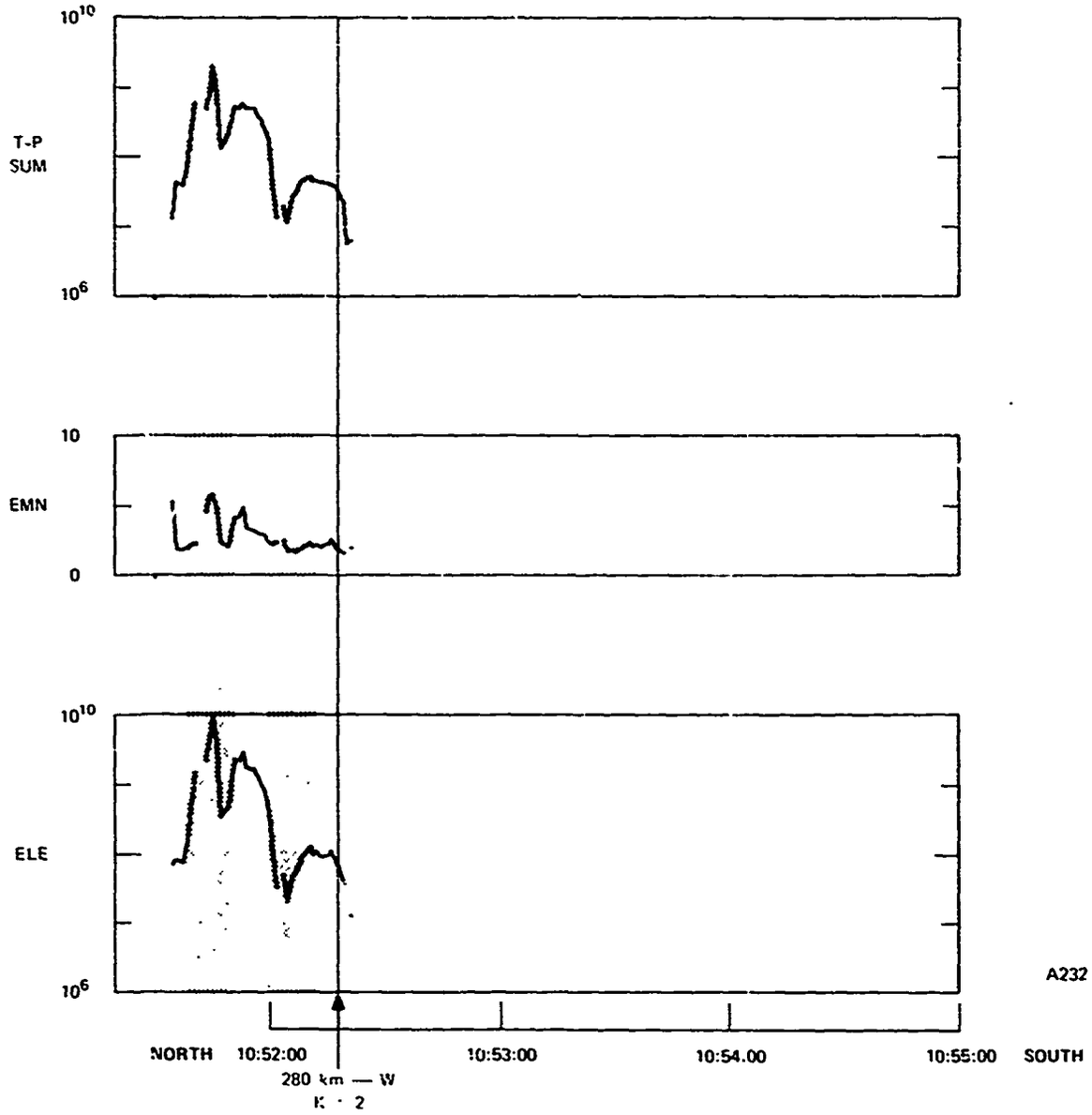

FIGURE 4.C.6 PRECIPITATING ELECTRON NUMBER FLUX (TSUM), AVERAGE ENERGY (EMN), AND ENERGY FLUX (ELE) versus UNIVERSAL TIME FOR SATELLITE PASS A232

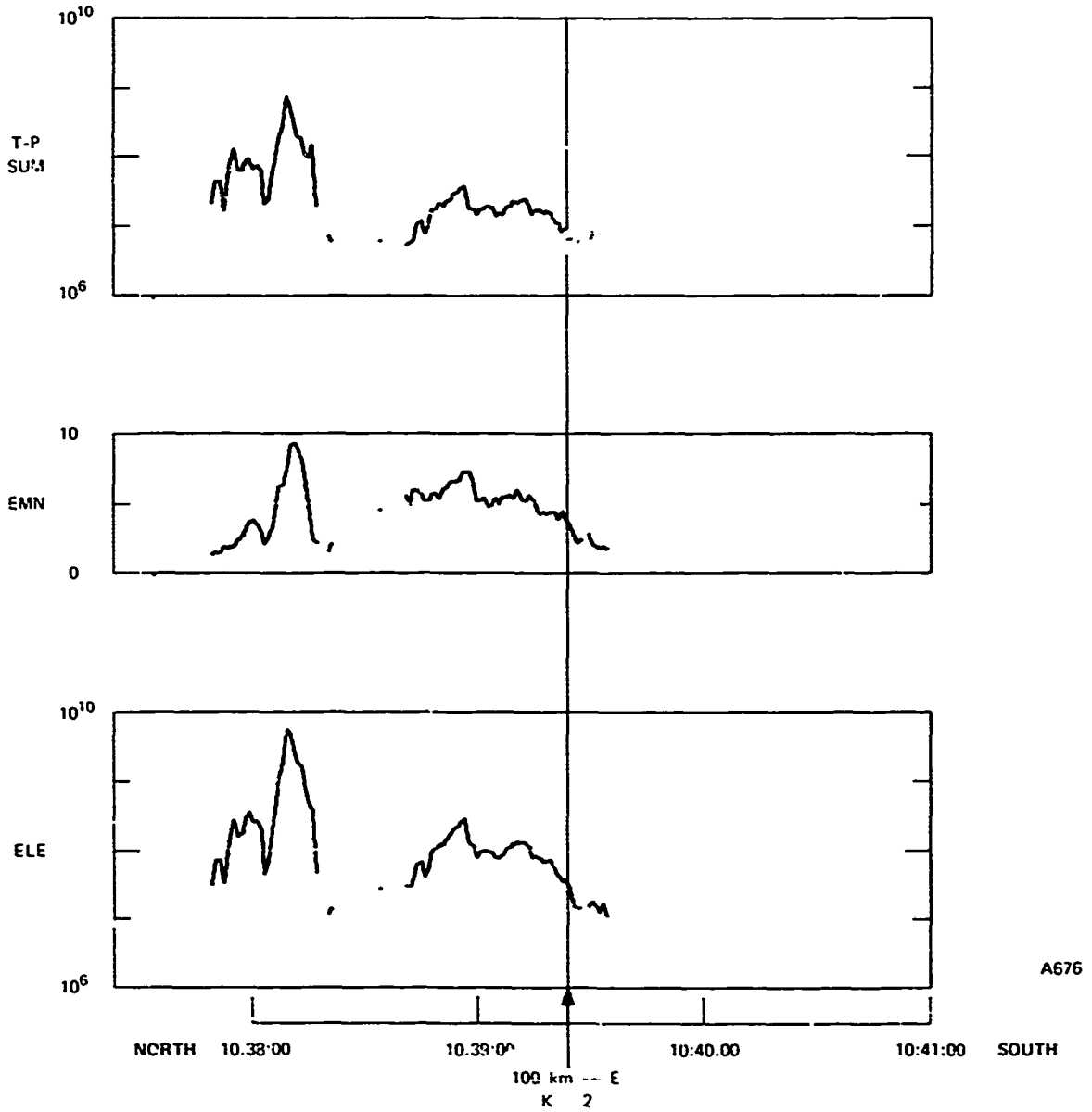

FIGURE 4.3.7 PRECIPITATING ELECTRON NUMBER FLUX (TSUM), AVERAGE ENERGY (EMN), AND ENERGY FLUX (ELE) versus UNIVERSAL TIME FOR SATELLITE PASS A676

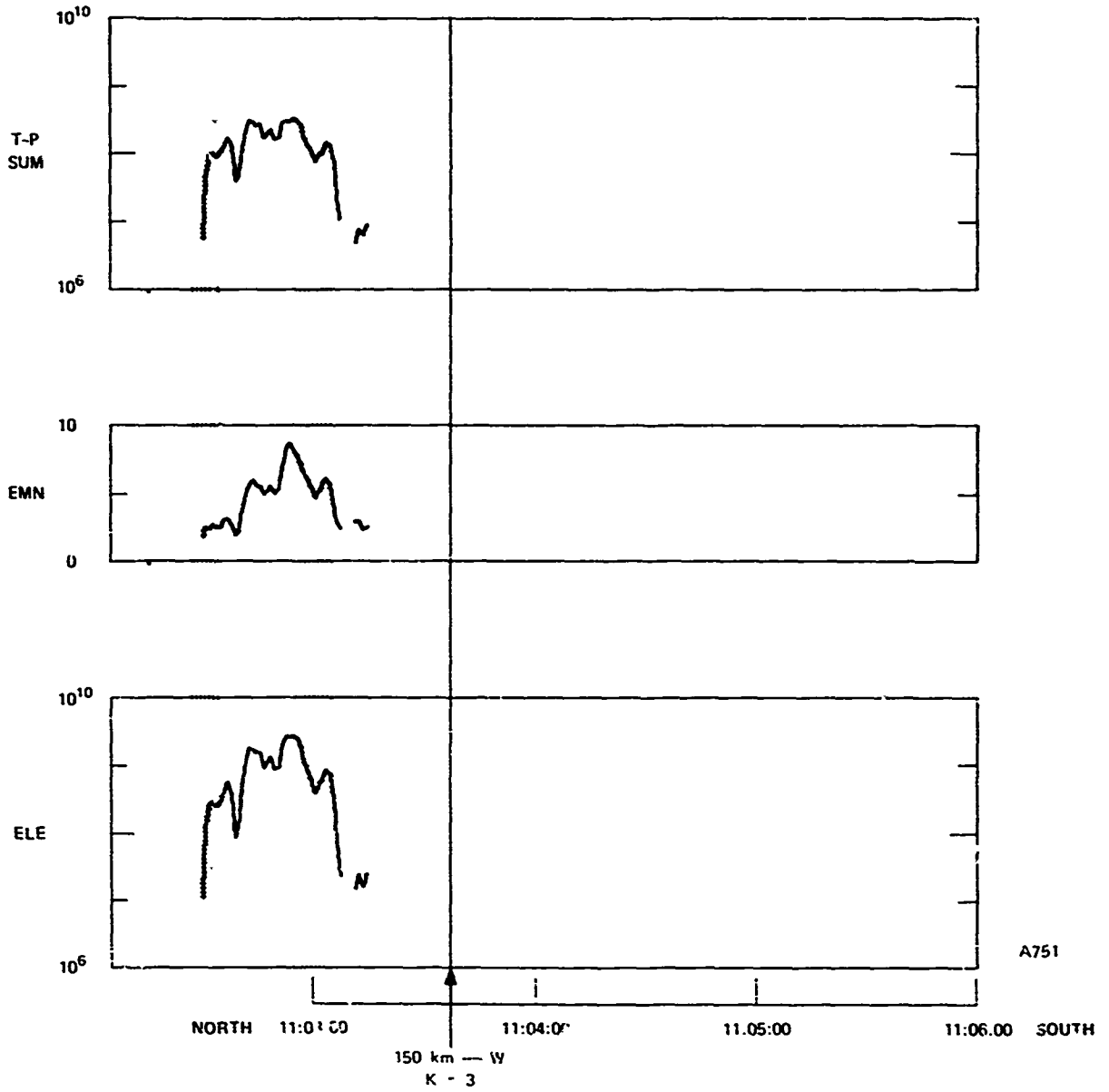

FIGURE 4.C.8 PRECIPITATING ELECTRON NUMBER FLUX (TSUM), AVERAGE ENERGY (EMN), AND ENERGY FLUX (ELE) versus UNIVERSAL TIME FOR SATELLITE PASS A751

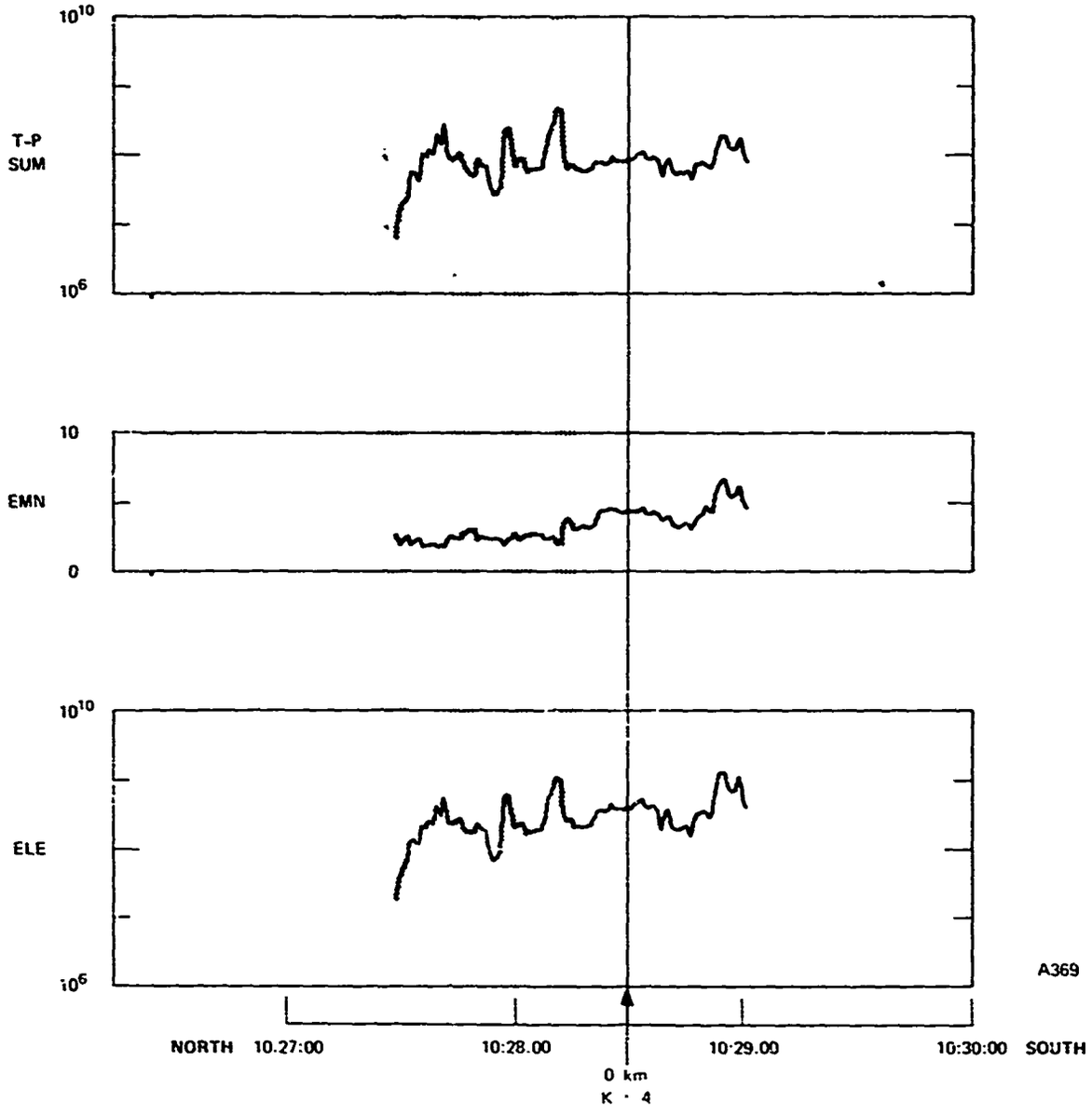

FIGURE 4.C.9 PRECIPITATING ELECTRON NUMBER FLUX (TSUM), AVERAGE ENERGY (EMN), AND ENERGY FLUX (ELE) versus UNIVERSAL TIME FOR SATELLITE PASS A369

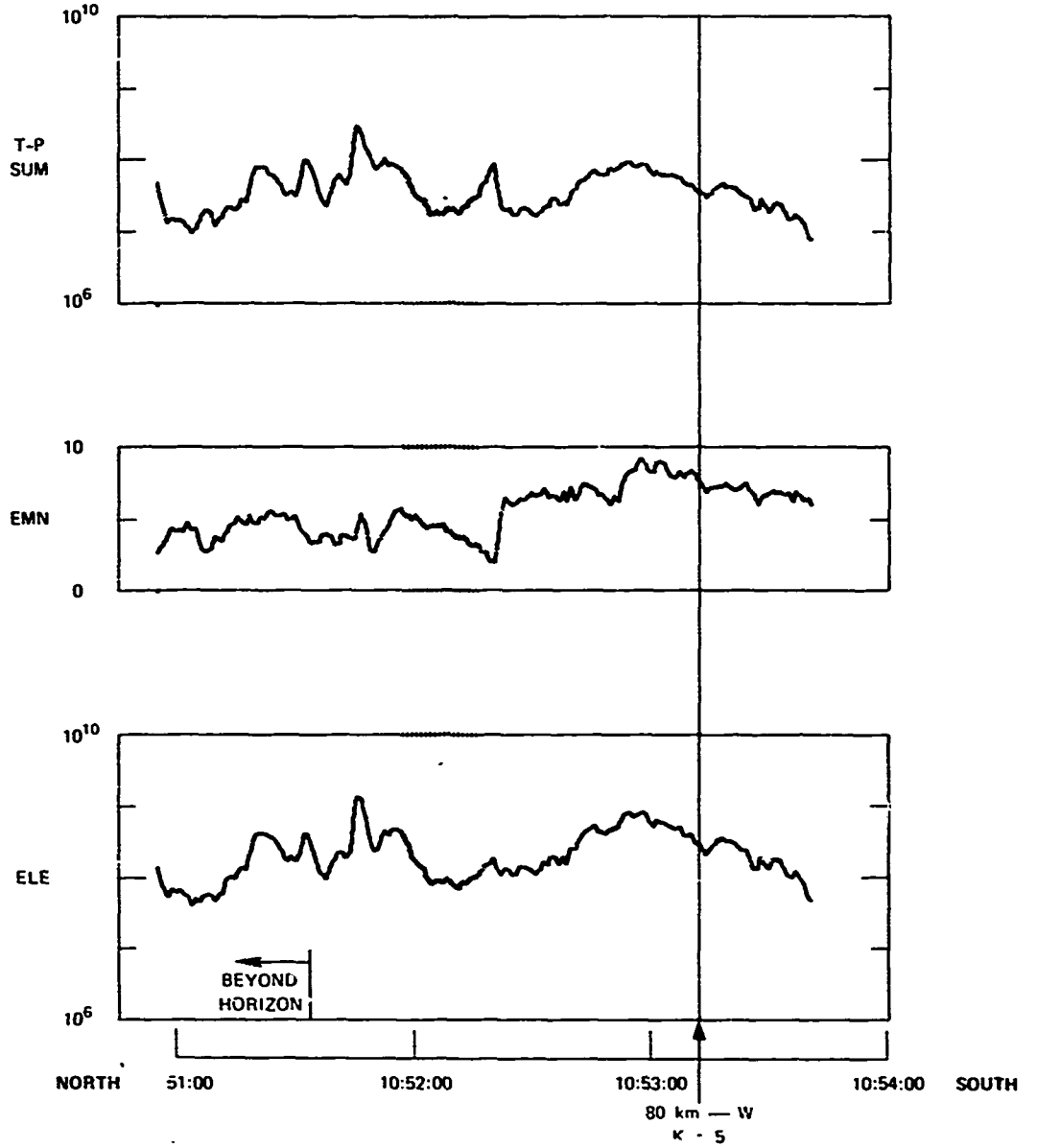

FIGURE 4.C.10 PRECIPITATING ELECTRON NUMBER FLUX (TSUM), AVERAGE ENERGY (EMN), AND ENERGY FLUX (ELE) versus UNIVERSAL TIME FOR SATELLITE PASS A657

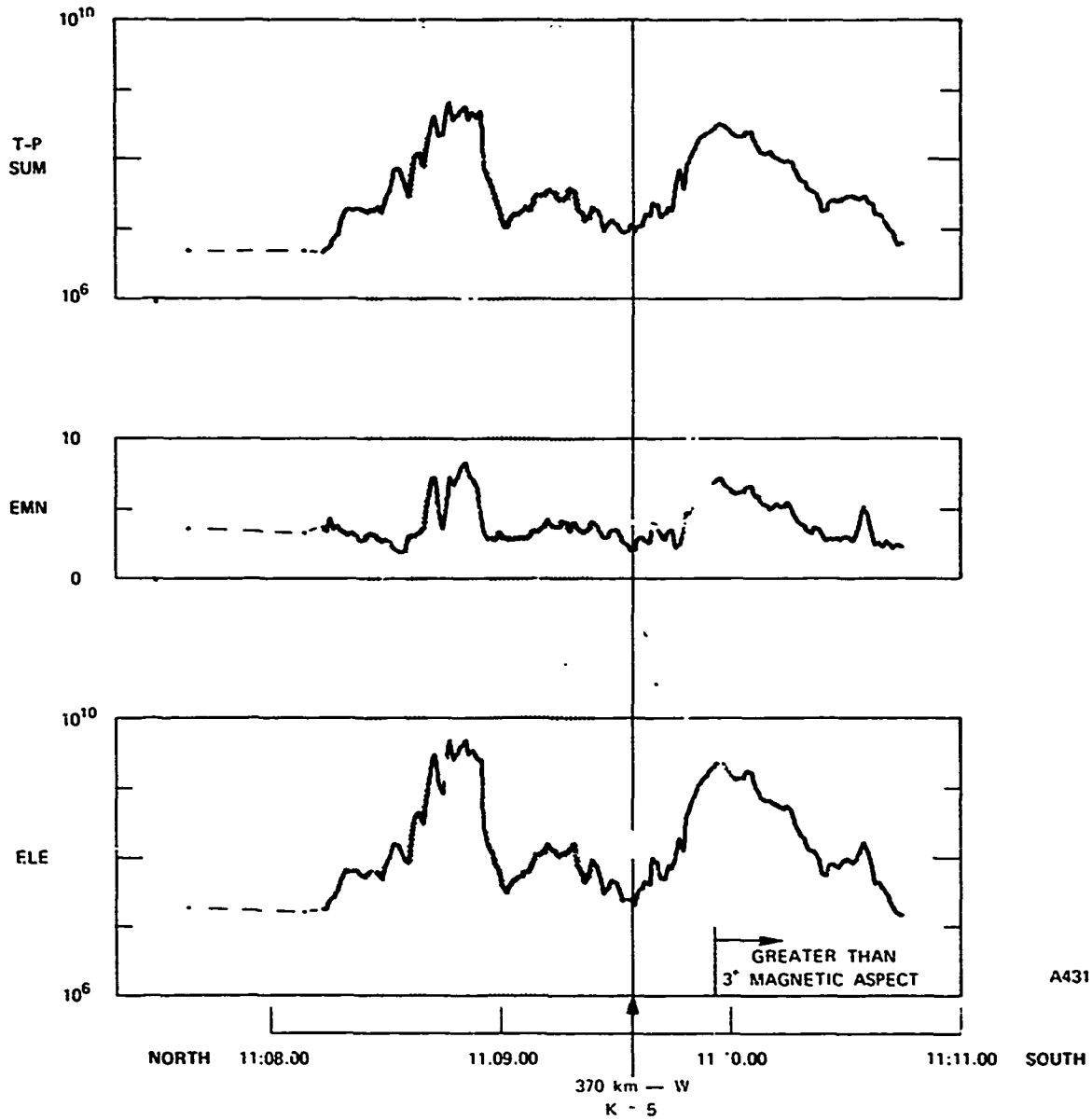

FIGURE 4.C.11 PRECIPITATING ELECTRON NUMBER FLUX (TSUM), AVERAGE ENERGY (EMN), AND ENERGY FLUX (ELE) versus UNIVERSAL TIME FOR SATELLITE PASS A431

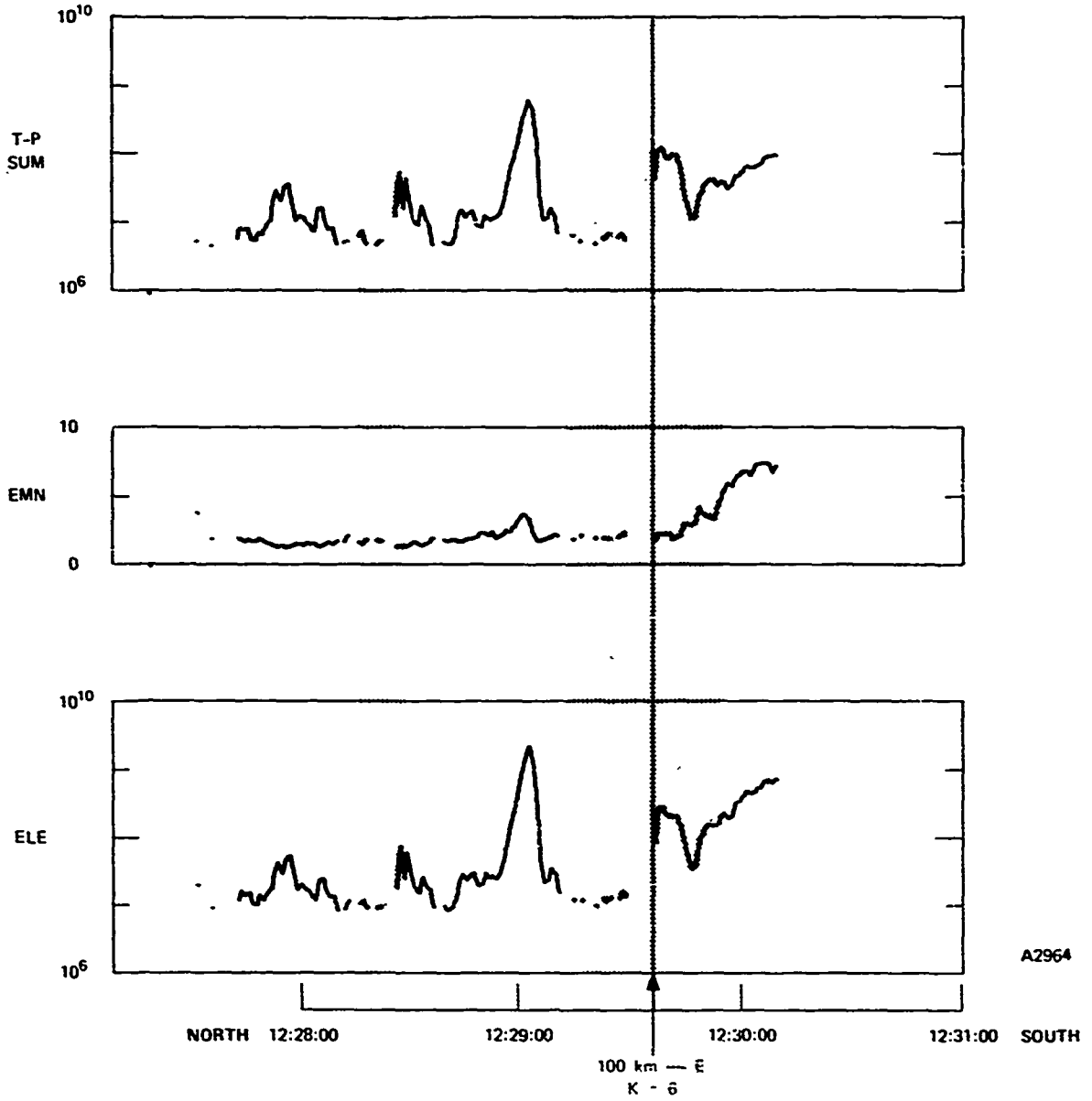

FIGURE 4.C.12 PRECIPITATING ELECTRON NUMBER FLUX (TSUM), AVERAGE ENERGY (EMN), AND ENERGY FLUX (ELE) versus UNIVERSAL TIME FOR SATELLITE PASS A2964

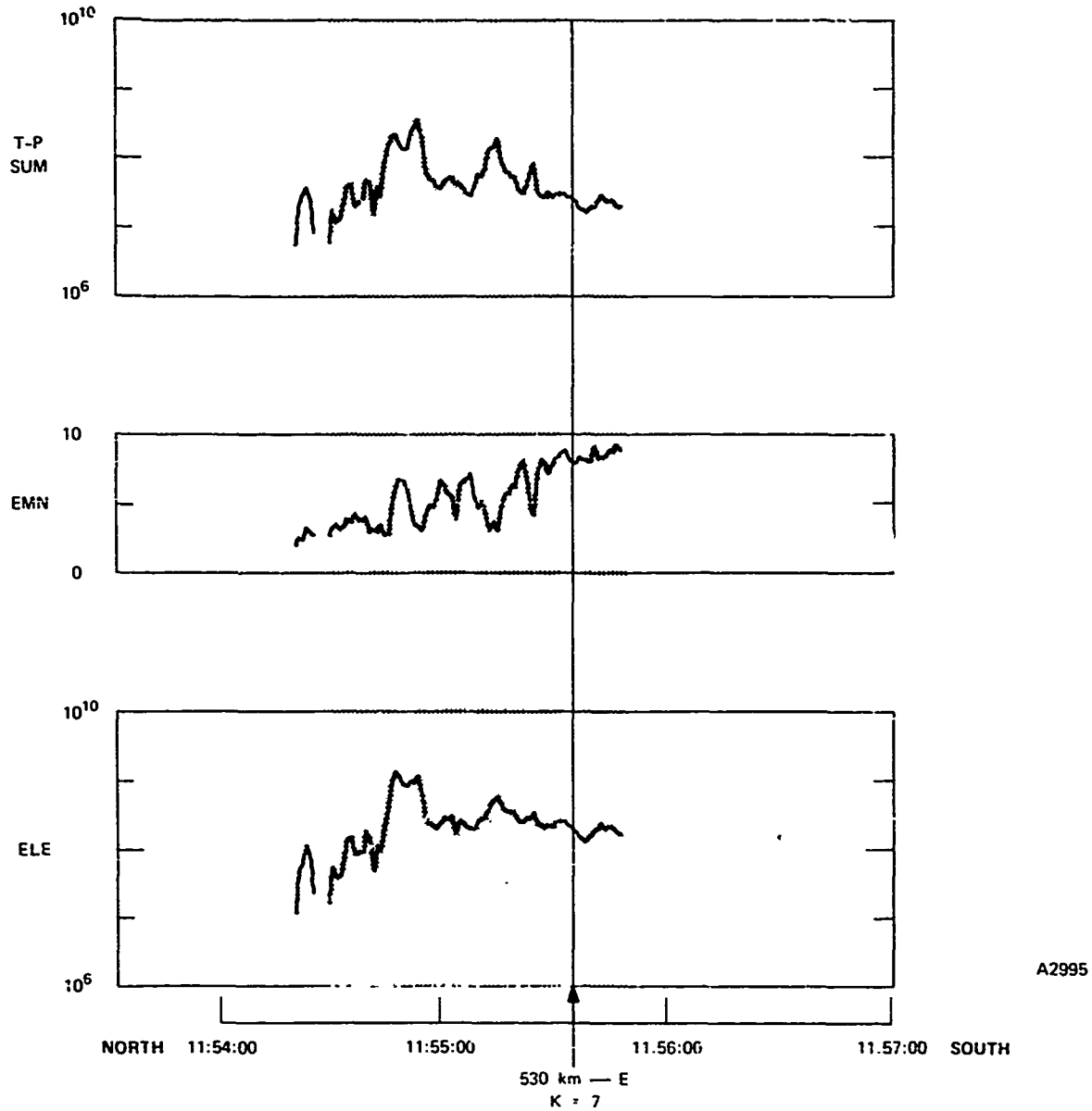

FIGURE 4.C.13 PRECIPITATING ELECTRON NUMBER FLUX (TSUM), AVERAGE ENERGY (EMN), AND ENERGY FLUX (ELE) versus UNIVERSAL TIME FOR SATELLITE PASS A2995

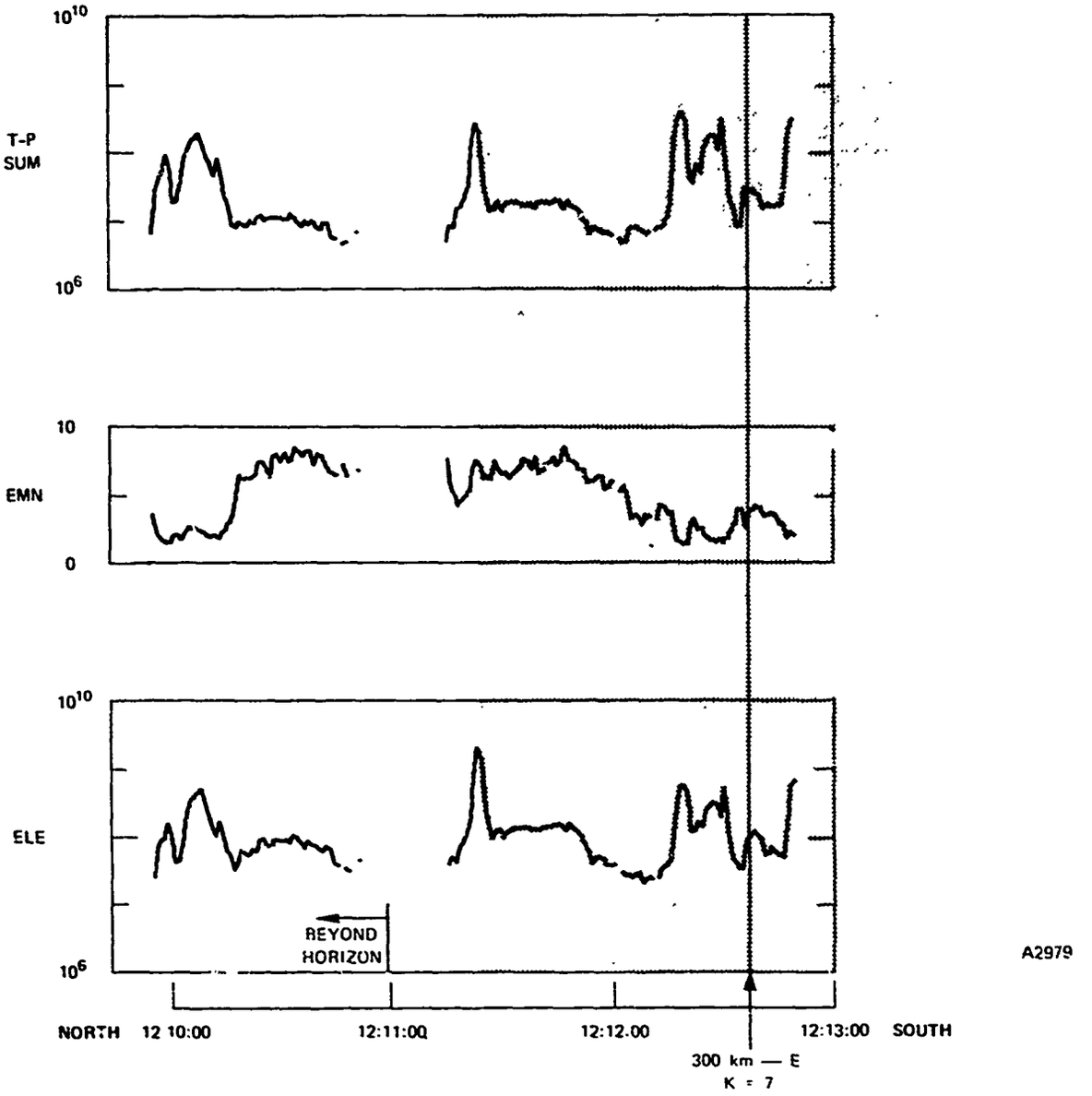

FIGURE 4.C.14 PRECIPITATING ELECTRON NUMBER FLUX (T-SUM), AVERAGE ENERGY (EMN), AND ENERGY FLUX (ELE) versus UNIVERSAL TIME FOR SATELLITE PASS A2979

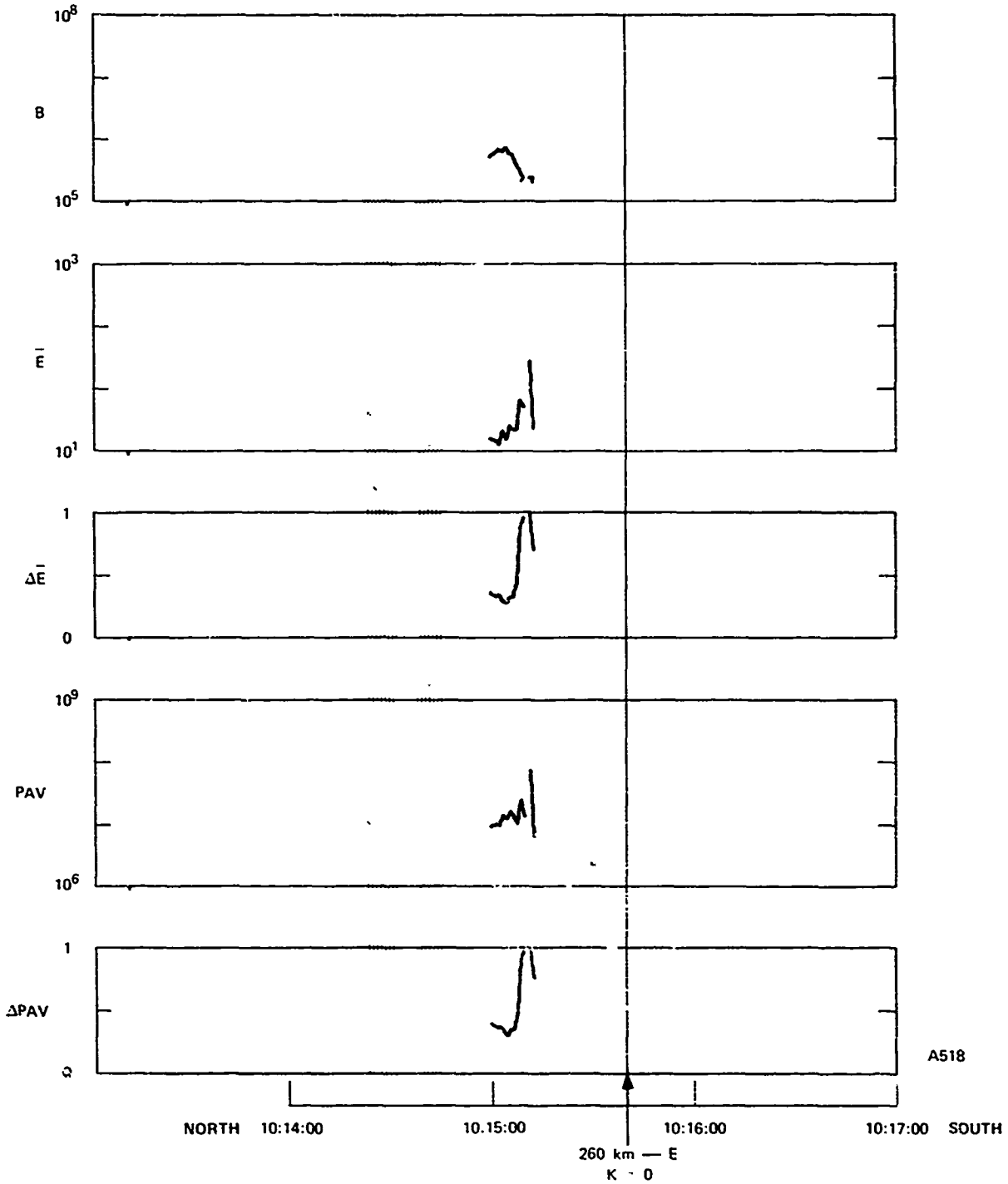

FIGURE 4.D.1 PRECIPITATING PROTON NUMBER FLUX (B), AVERAGE ENERGY ($\bar{E}$), STATISTICAL ERROR IN AVERAGE ENERGY ($\Delta\bar{E}$), ENERGY FLUX (PAV), AND STATISTICAL ERROR IN ENERGY FLUX (ΔPAV) versus UNIVERSAL TIME FOR SATELLITE PASS A518

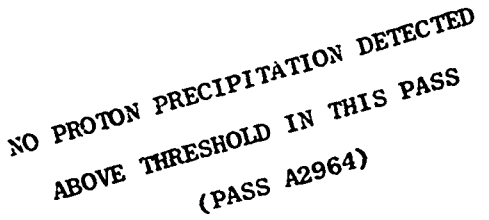

FIGURE 4.D.2 PRECIPITATING PROTON NUMBER FLUX (B), AVERAGE ENERGY ($\bar{E}$), STATISTICAL ERROR IN AVERAGE ENERGY ($\Delta\bar{E}$), ENERGY FLUX (PAV), AND STATISTICAL ERROR IN ENERGY FLUX (ΔPAV) versus UNIVERSAL TIME FOR SATELLITE PASS A641

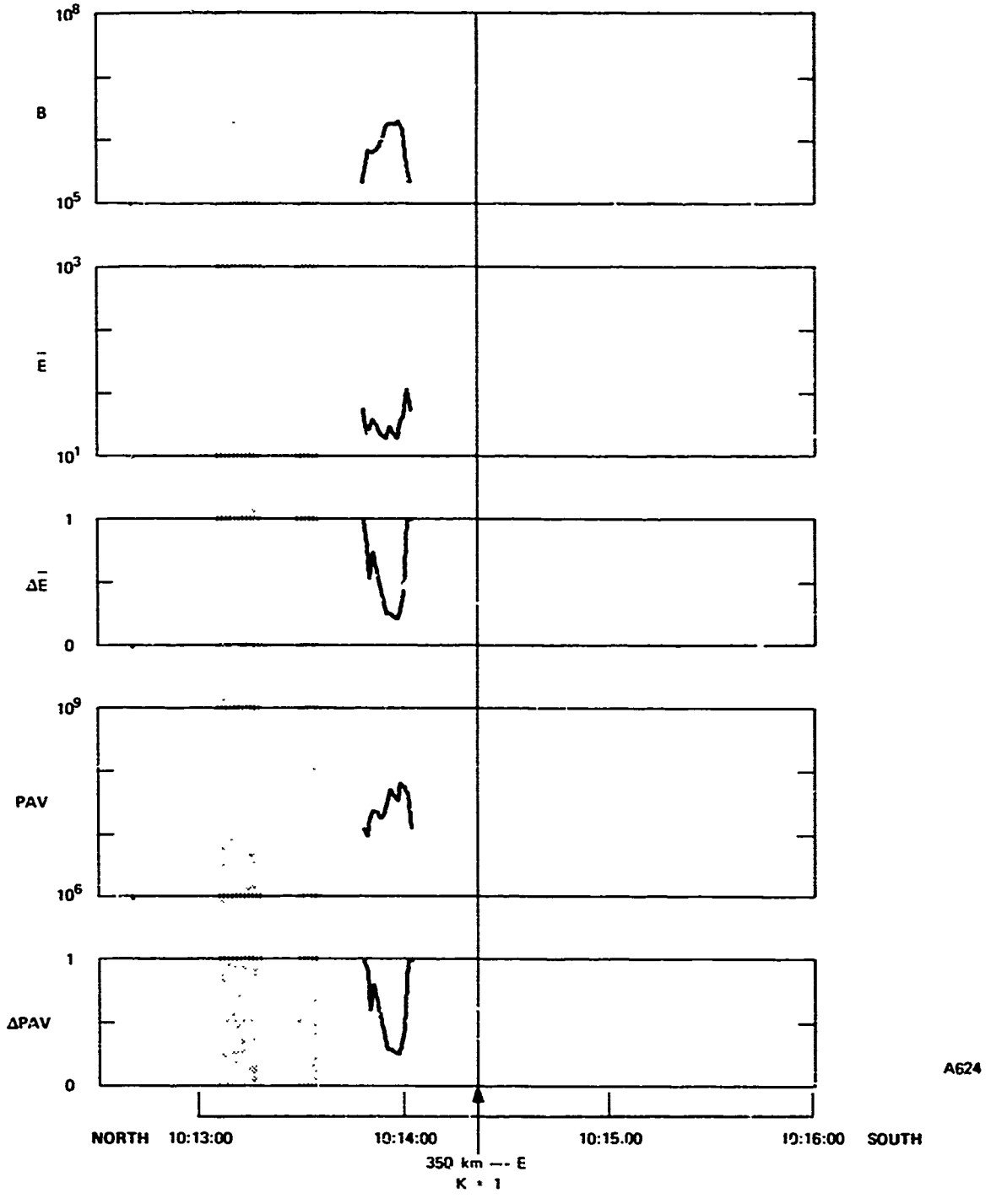

FIGURE 4.D.3 PRECIPITATING PROTON NUMBER FLUX (B), AVERAGE ENERGY ($\bar{E}$), STATISTICAL ERROR IN AVERAGE ENERGY ($\Delta\bar{E}$), ENERGY FLUX (PAV), AND STATISTICAL ERROR IN ENERGY FLUX (ΔPAV) versus UNIVERSAL TIME FOR SATELLITE PASS A624

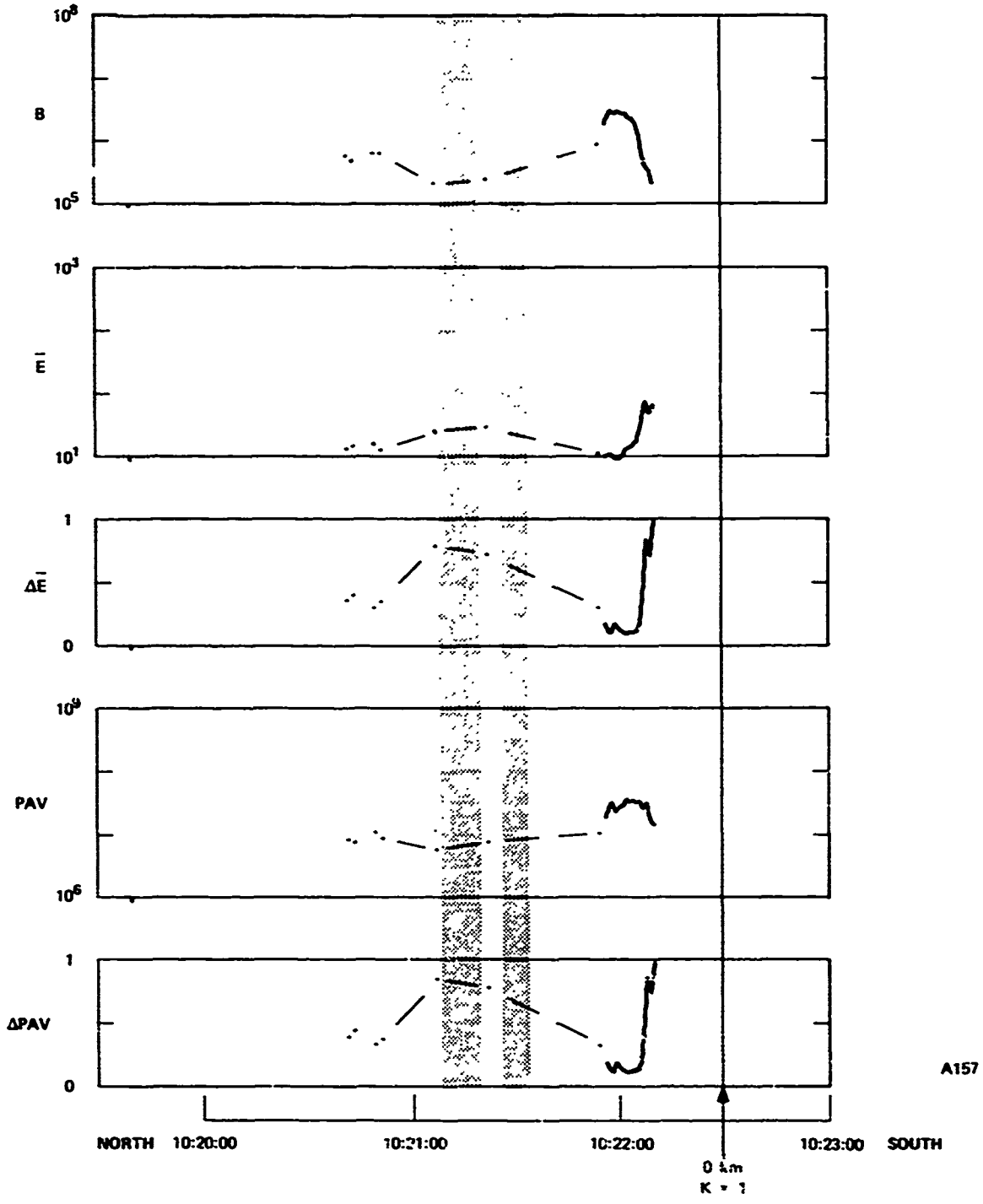

FIGURE 4.D.4 PRECIPITATING PROTON NUMBER FLUX (B), AVERAGE ENERGY ($\bar{E}$), STATISTICAL ERROR IN AVERAGE ENERGY ($\Delta\bar{E}$), ENERGY FLUX (PAV), AND STATISTICAL ERROR IN ENERGY FLUX (ΔPAV) versus UNIVERSAL TIME FOR SATELLITE PASS A157

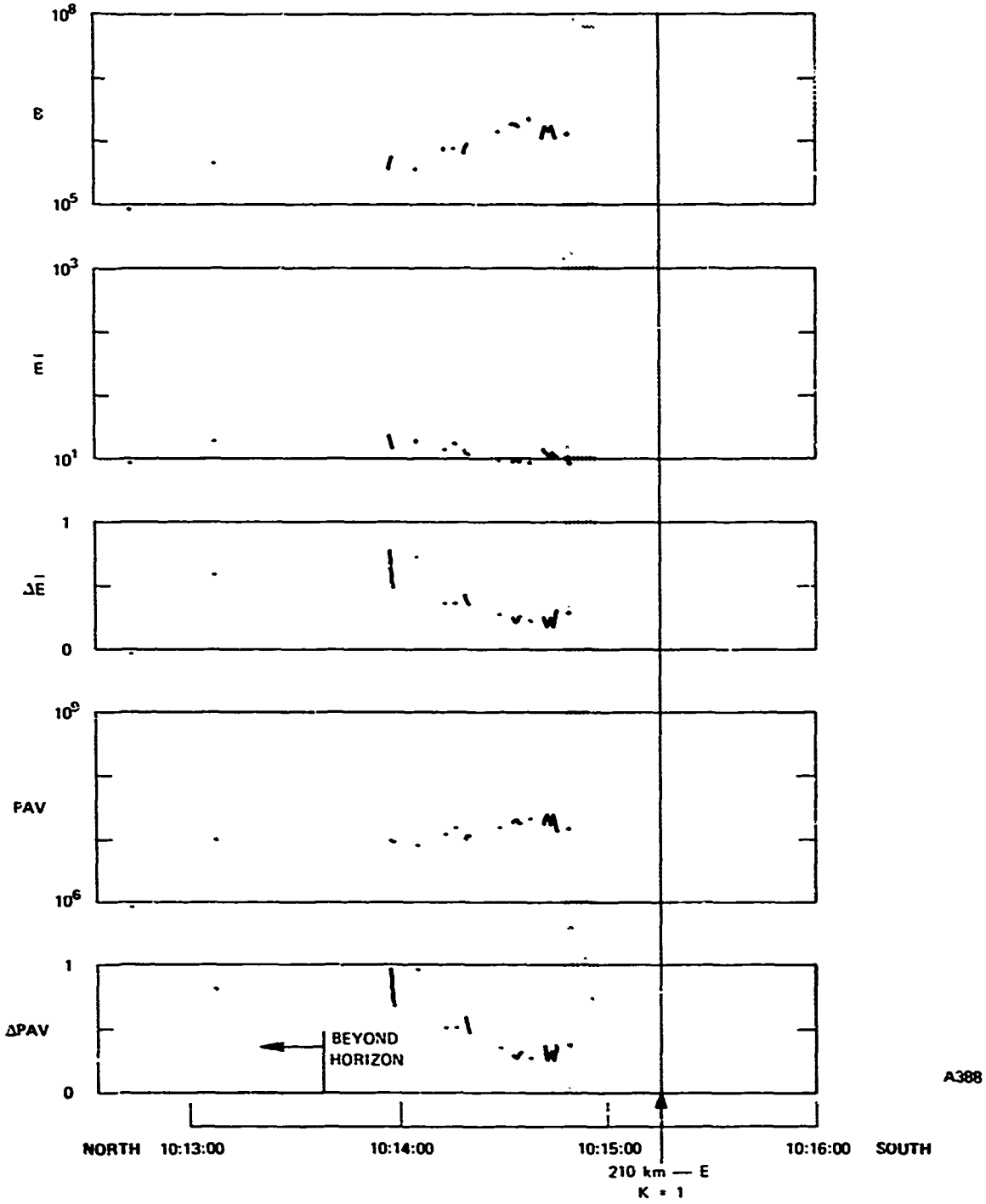

FIGURE 4.D.5 PRECIPITATING PROTON NUMBER FLUX (B), AVERAGE ENERGY ($\bar{E}$), STATISTICAL ERROR IN AVERAGE ENERGY ($\Delta\bar{E}$), ENERGY FLUX (PAV), AND STATISTICAL ERROR IN ENERGY FLUX (ΔPAV) versus UNIVERSAL TIME FOR SATELLITE PASS A388

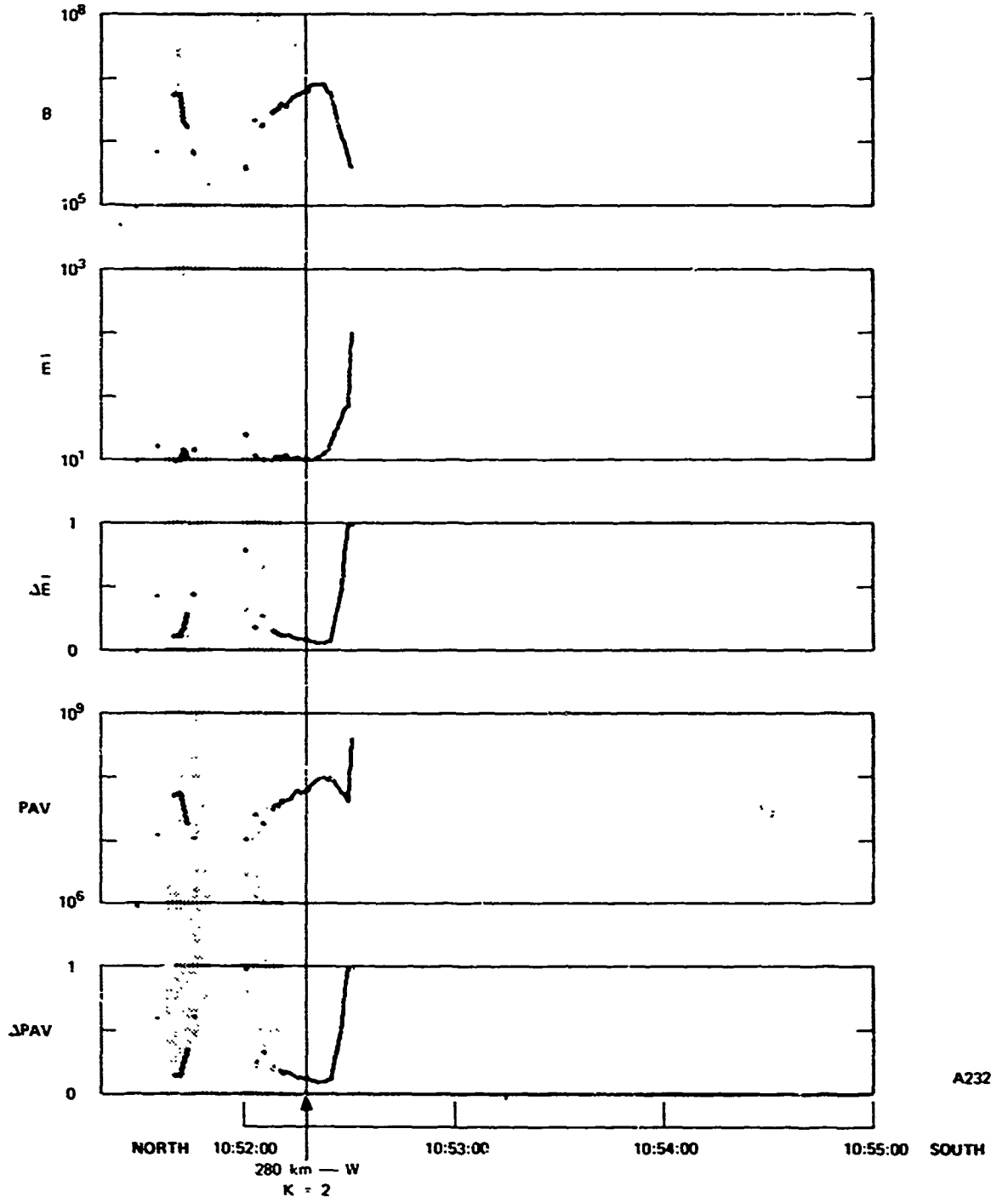

FIGURE 4.D.6 PRECIPITATING PROTON NUMBER FLUX (B), AVERAGE ENERGY ($\bar{E}$), STATISTICAL ERROR IN AVERAGE ENERGY ($\Delta\bar{E}$), ENERGY FLUX (PAV), AND STATISTICAL ERROR IN ENERGY FLUX (ΔPAV) versus UNIVERSAL TIME FOR SATELLITE PASS A232

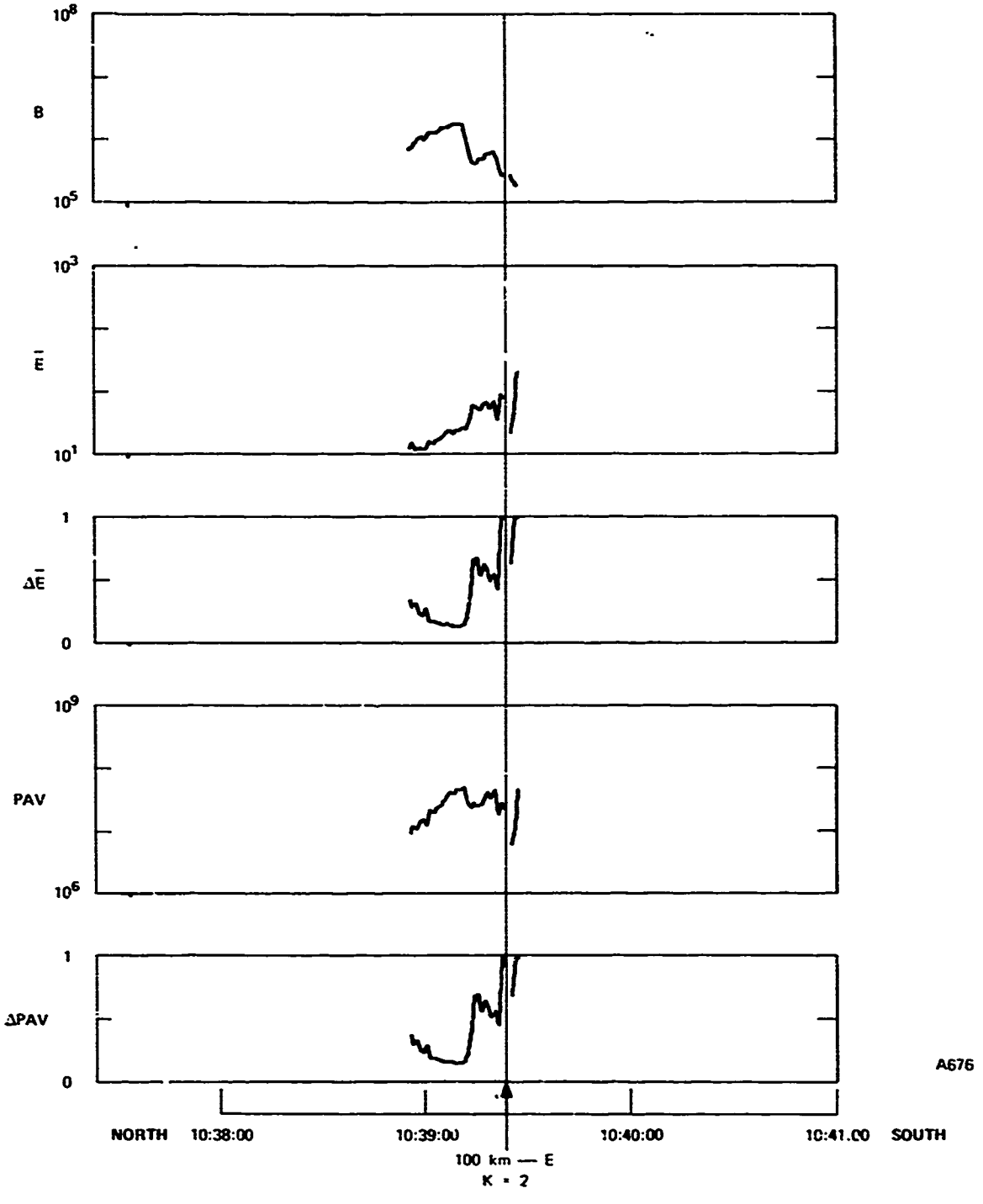

FIGURE 4.D.7 PRECIPITATING PROTON NUMBER FLUX (B), AVERAGE ENERGY ($\bar{E}$), STATISTICAL ERROR IN AVERAGE ENERGY ($\Delta\bar{E}$), ENERGY FLUX (PAV), AND STATISTICAL ERROR IN ENERGY FLUX (ΔPAV), versus UNIVERSAL TIME FOR SATELLITE PASS A676

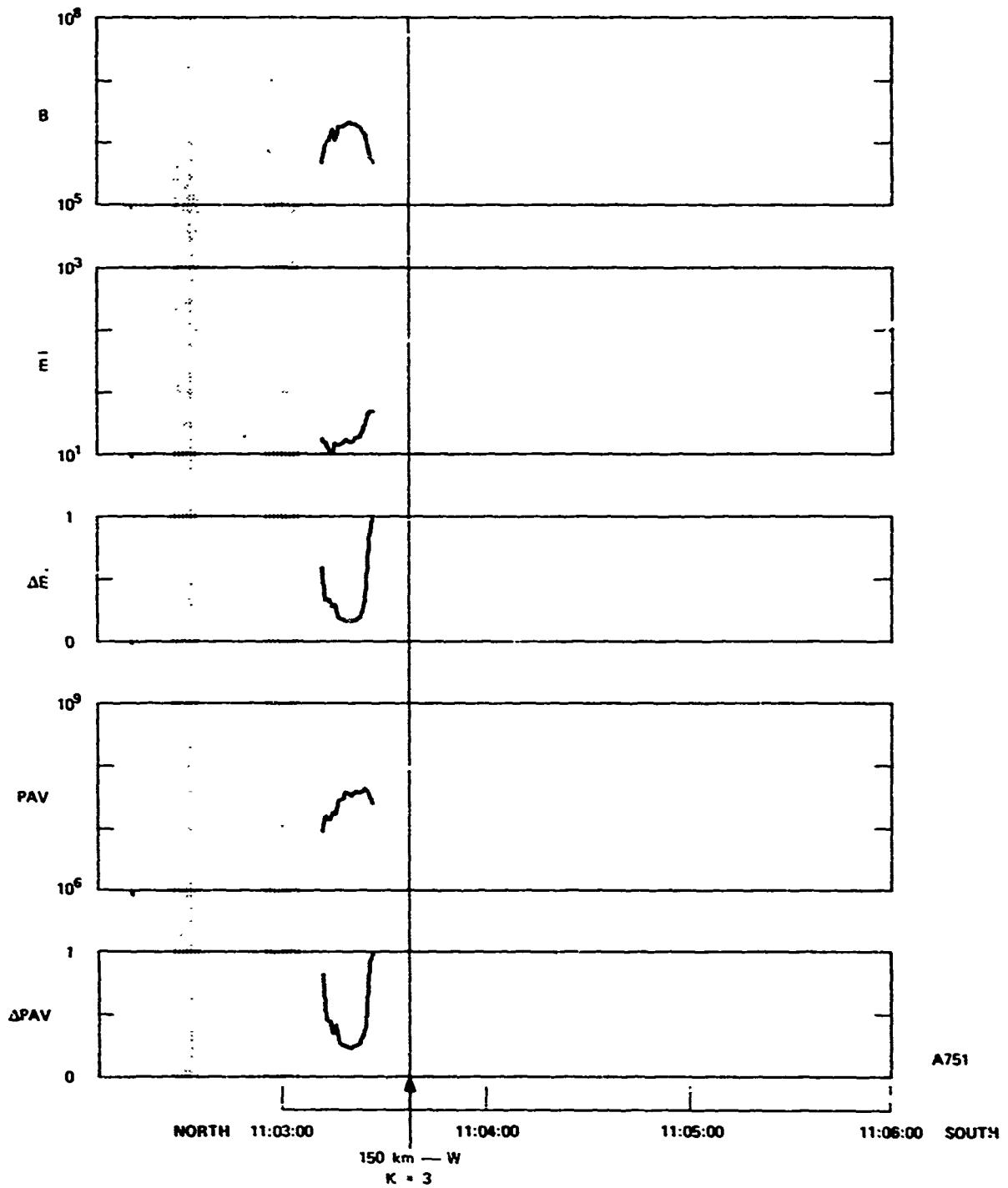

FIGURE 4.D.8 PRECIPITATING PROTON NUMBER FLUX (B), AVERAGE ENERGY ($\bar{E}$), STATISTICAL ERROR IN AVERAGE ENERGY ($\Delta\bar{E}$), ENERGY FLUX (PAV), AND STATISTICAL ERROR IN ENERGY FLUX (ΔPAV) versus UNIVERSAL TIME FOR SATELLITE PASS A751

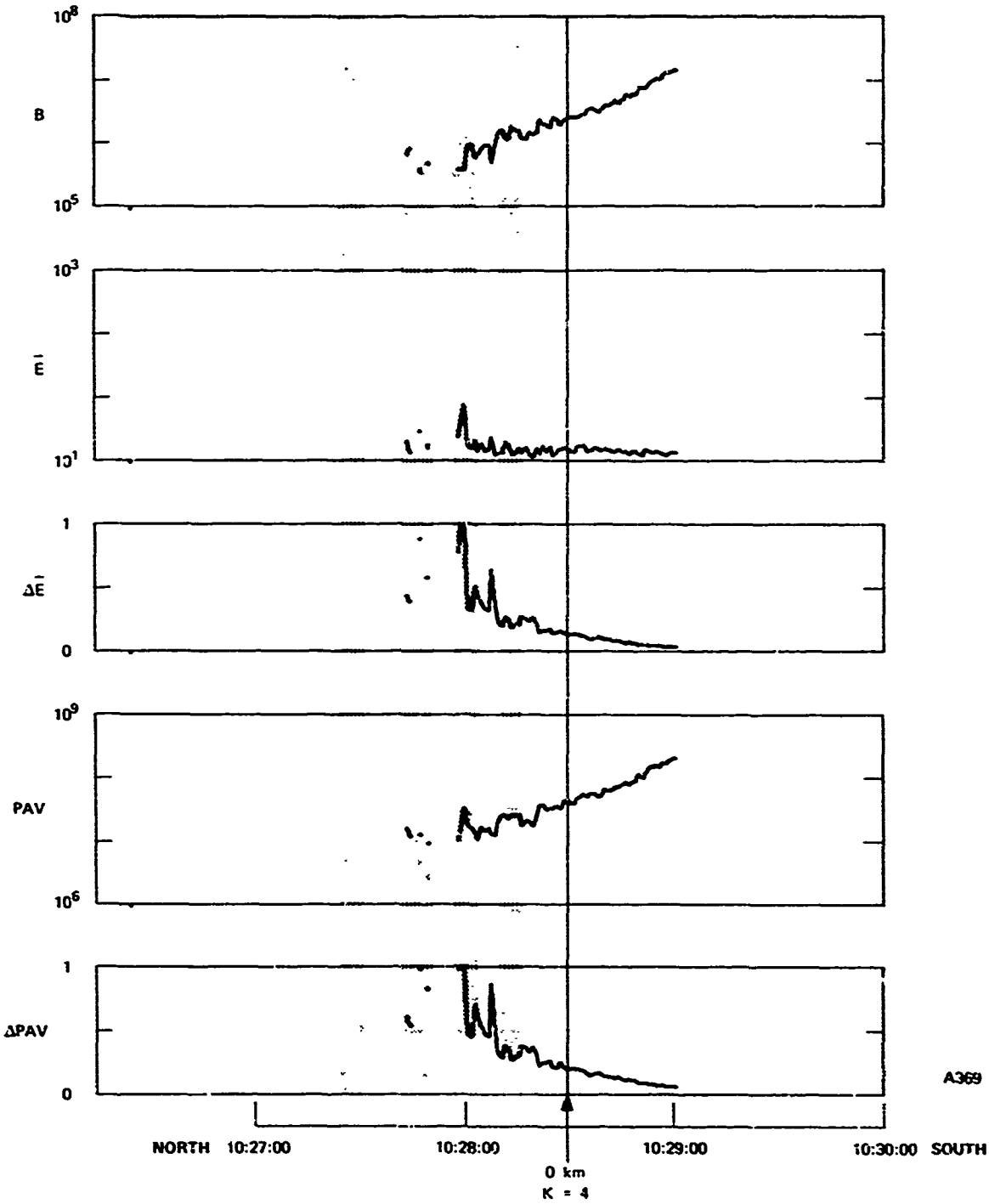

FIGURE 4.D.9 PRECIPITATING PROTON NUMBER FLUX (B), AVERAGE ENERGY ($\bar{E}$), STATISTICAL ERROR IN AVERAGE ENERGY ($\Delta\bar{E}$), ENERGY FLUX (PAV), AND STATISTICAL ERROR IN ENERGY FLUX (ΔPAV) versus UNIVERSAL TIME FOR SATELLITE PASS A369

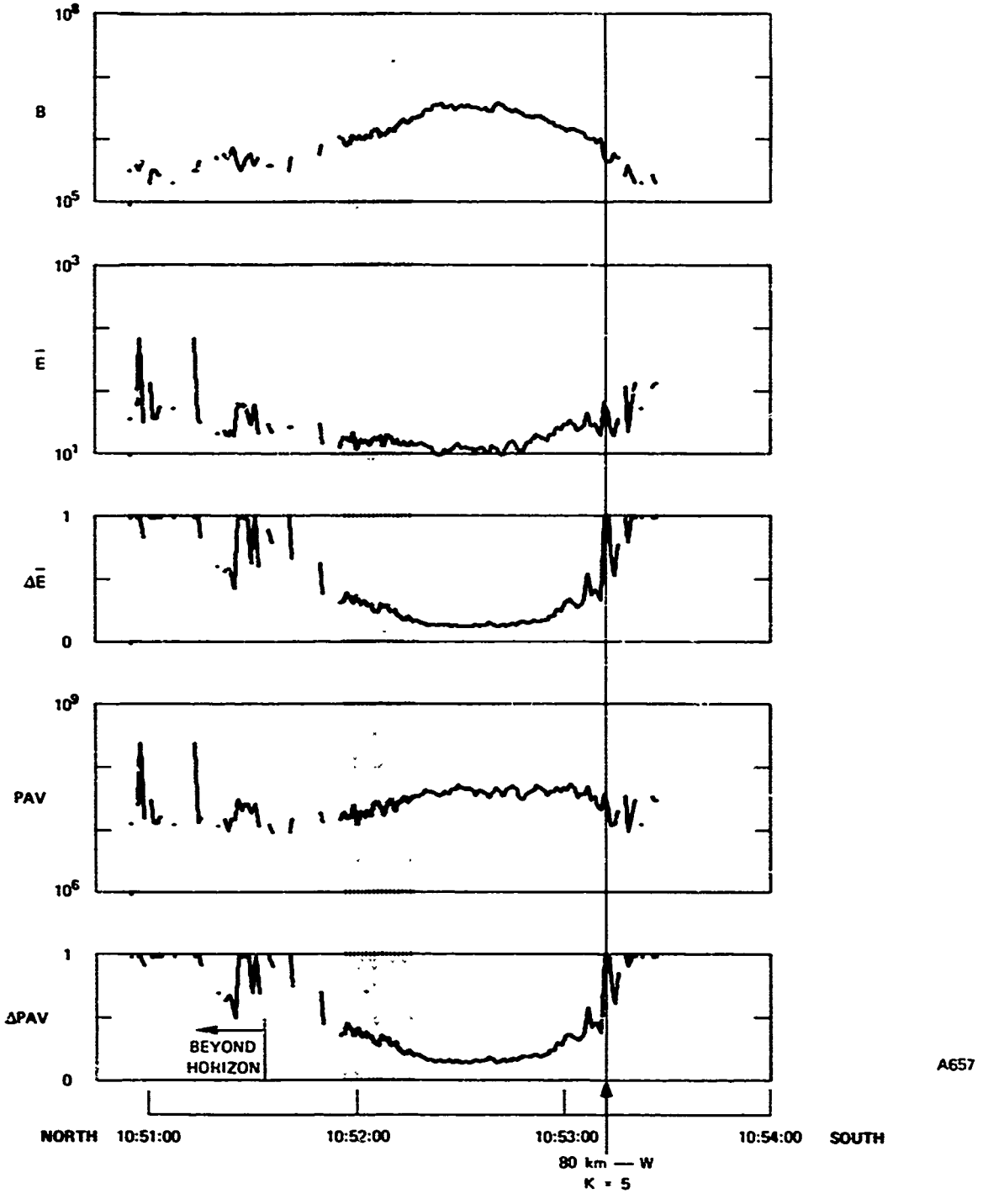

FIGURE 4.D.10 PRECIPITATING PROTON NUMBER FLUX (B), AVERAGE ENERGY ($\bar{E}$), STATISTICAL ERROR IN AVERAGE ENERGY ($\Delta\bar{E}$), ENERGY FLUX (PAV), AND STATISTICAL ERROR IN ENERGY FLUX (ΔPAV) versus UNIVERSAL TIME FOR SATELLITE PASS A657

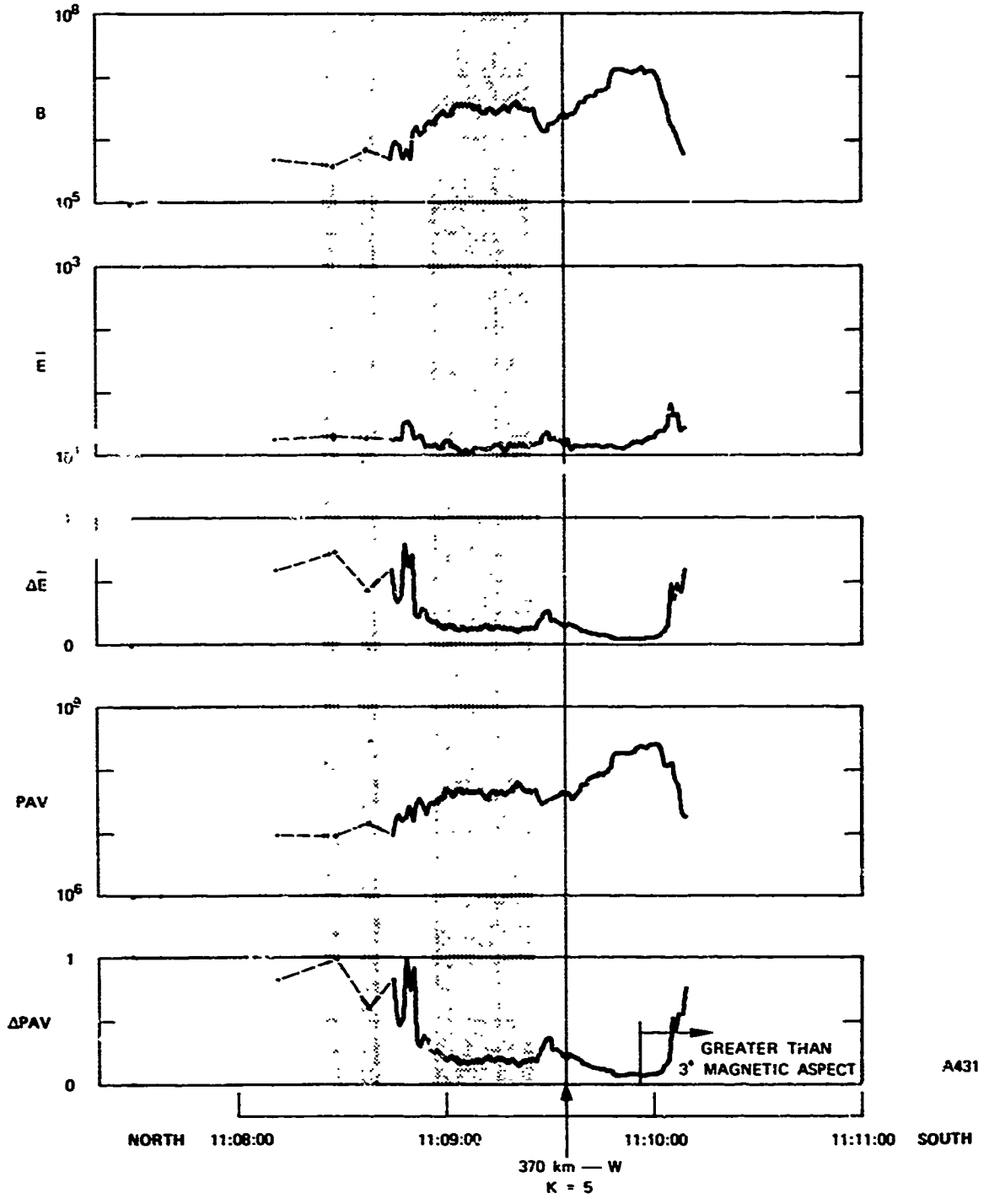

FIGURE 4.D.11 PRECIPITATING PROTON NUMBER FLUX (B), AVERAGE ENERGY ($\bar{E}$), STATISTICAL ERROR IN AVERAGE ENERGY ($\Delta\bar{E}$), ENERGY FLUX (PAV), AND STATISTICAL ERROR IN ENERGY FLUX (ΔPAV) versus UNIVERSAL TIME FOR SATELLITE PASS A431

NO PROTON PRECIPITATION DETECTED
ABOVE THRESHOLD IN THIS PASS
(PASS A641)

FIGURE 4.D.12 PRECIPITATING PROTON NUMBER FLUX (B), AVERAGE ENERGY ($\bar{E}$), STATISTICAL ERROR IN AVERAGE ENERGY ($\Delta\bar{E}$), ENERGY FLUX (PAV), AND STATISTICAL ERROR IN ENERGY FLUX (ΔPAV) versus UNIVERSAL TIME FOR SATELLITE PASS A2964

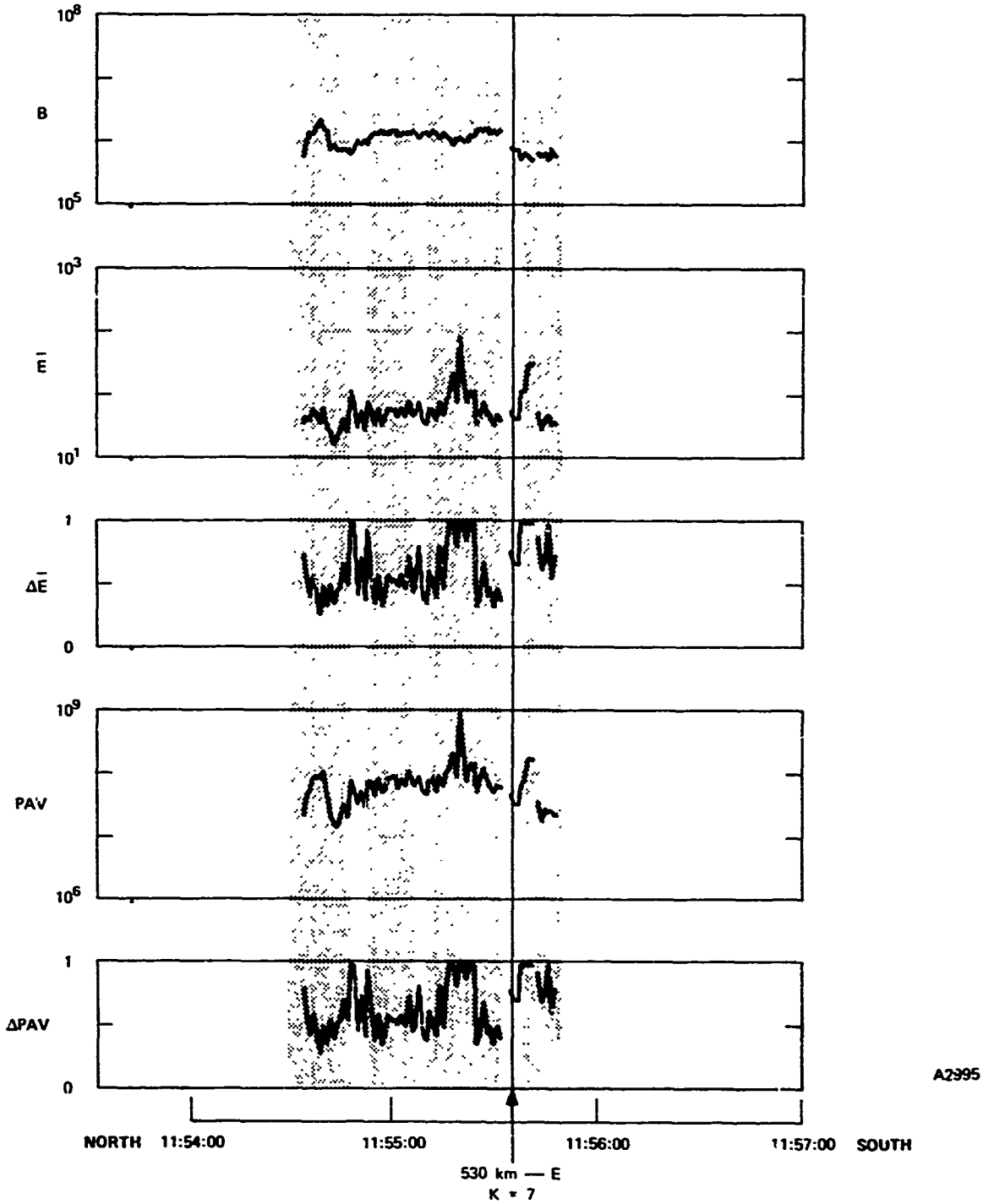

FIGURE 4.D.13 PRECIPITATING PROTON NUMBER FLUX (B), AVERAGE ENERGY ($\bar{E}$), STATISTICAL ERROR IN AVERAGE ENERGY ($\Delta\bar{E}$), ENERGY FLUX (PAV), AND STATISTICAL ERROR IN ENERGY FLUX (ΔPAV) versus UNIVERSAL TIME FOR SATELLITE PASS A2995

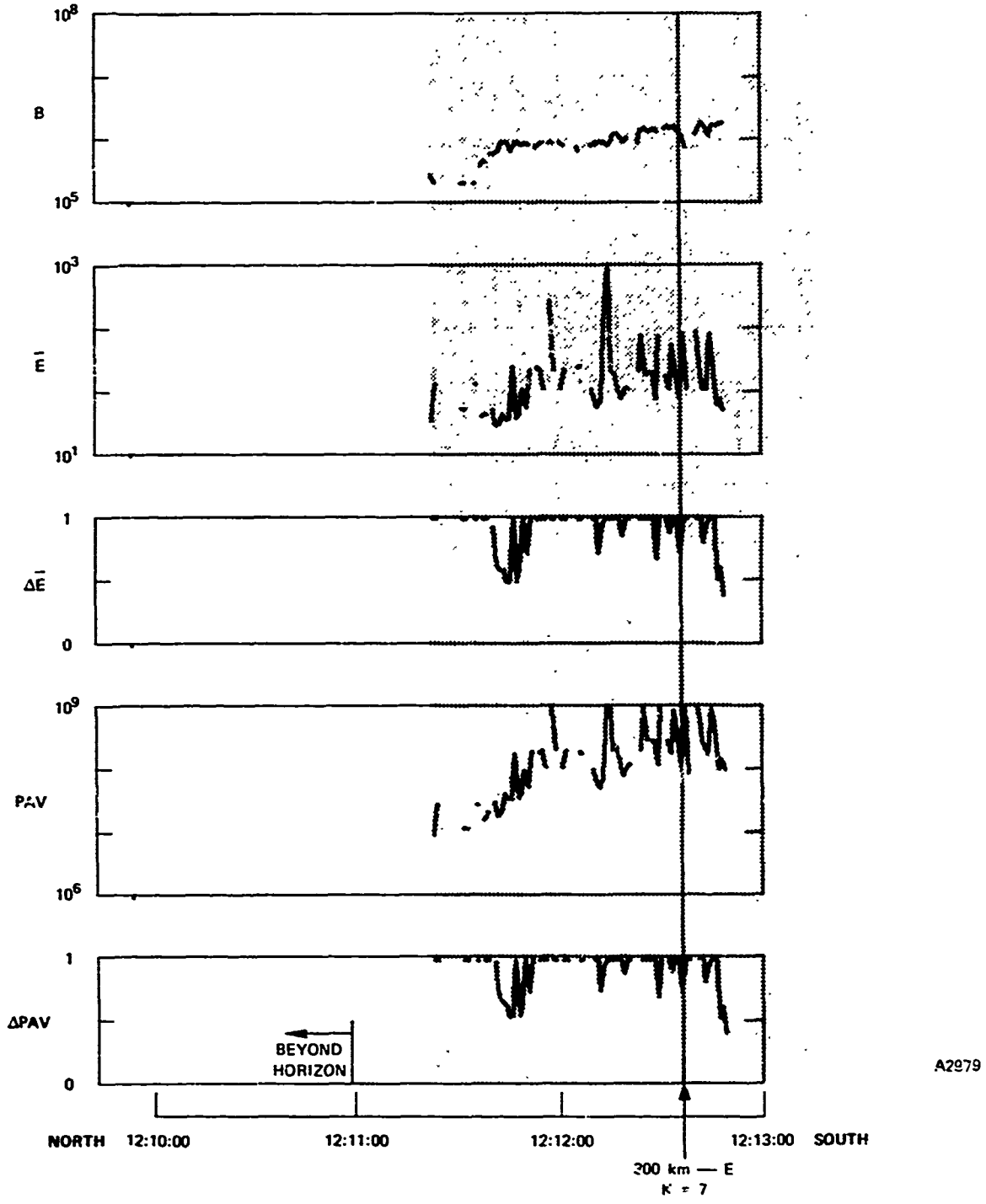

FIGURE 4.D.14 PRECIPITATING PROTON NUMBER FLUX (B), AVERAGE ENERGY ($\bar{E}$), STATISTICAL ERROR IN AVERAGE ENERGY ($\Delta\bar{E}$), ENERGY FLUX (PAV), AND STATISTICAL ERROR IN ENERGY FLUX (ΔPAV) versus UNIVERSAL TIME FOR SATELLITE PASS A2979

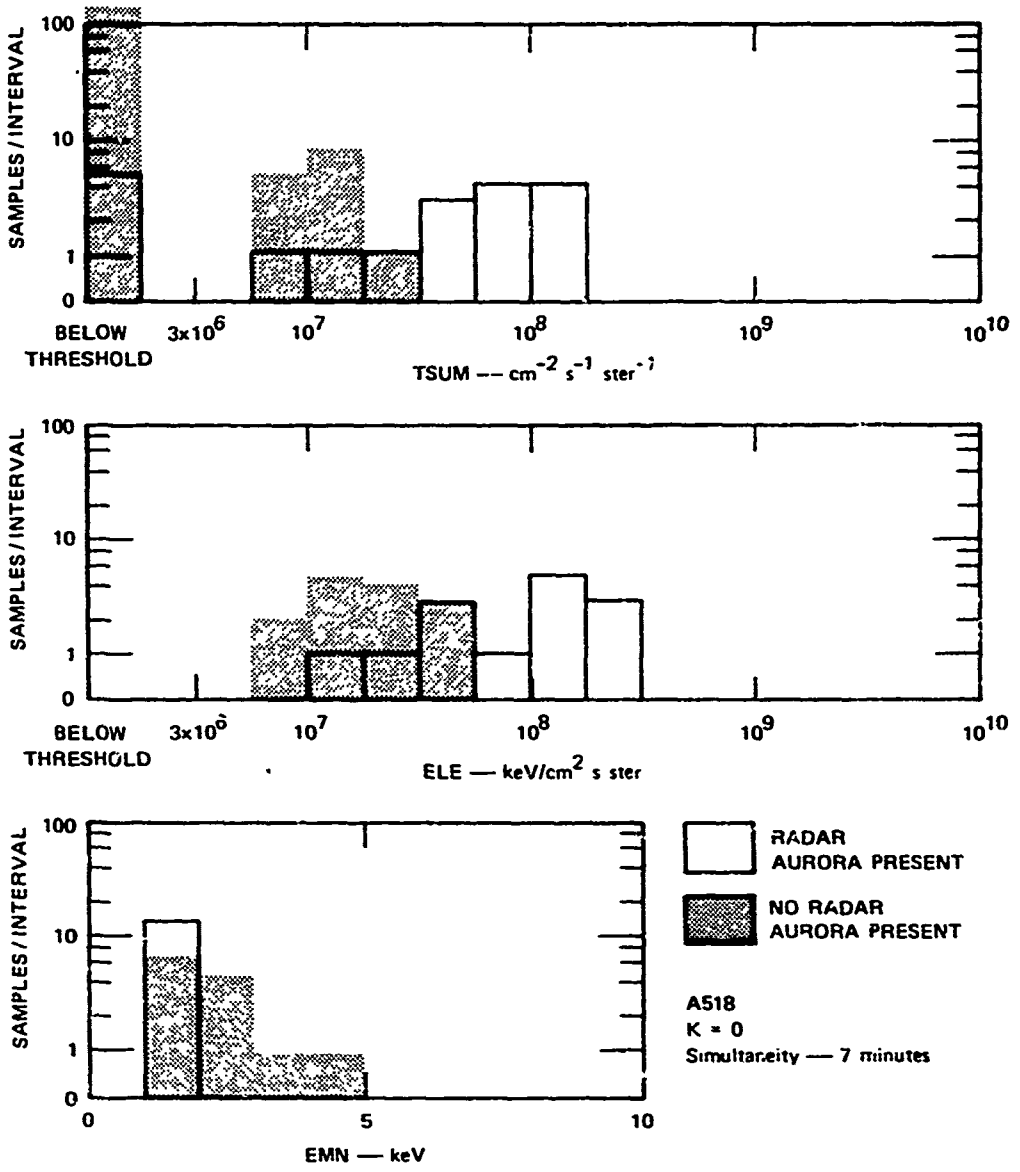

FIGURE 4.E.1 HISTOGRAMS OF LOGARITHMIC OCCURRENCE versus PRECIPITATING ELECTRON NUMBER FLUX (TSUM), ENERGY FLUX (ELE), AND AVERAGE ENERGY (EMN) FOR SATELLITE PASS A518

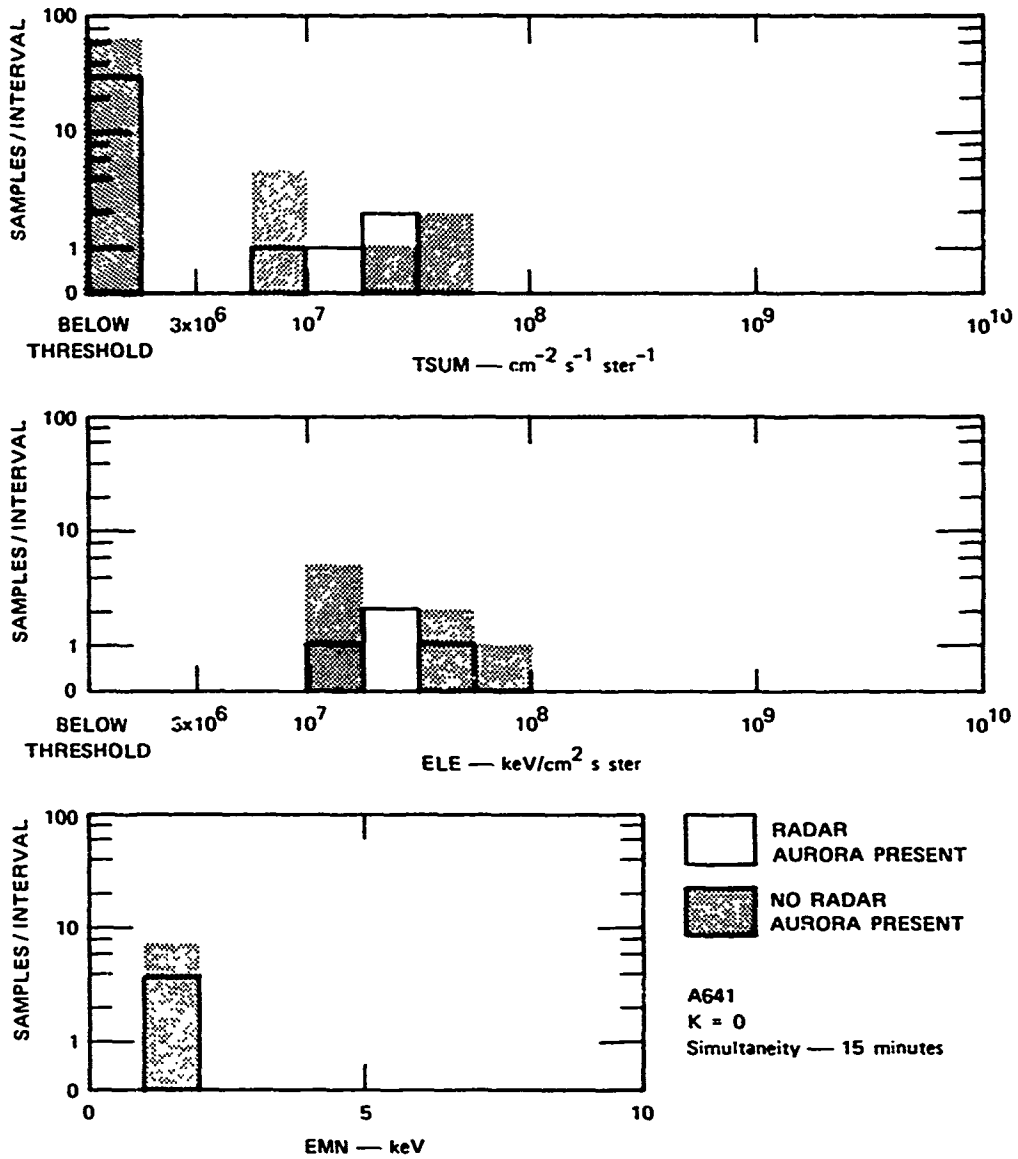

FIGURE 4.E.2 HISTOGRAMS OF LOGARITHMIC OCCURRENCE versus PRECIPITATING ELECTRON NUMBER FLUX (TSUM), ENERGY FLUX (ELE), AND AVERAGE ENERGY (EMN) FOR SATELLITE PASS A641

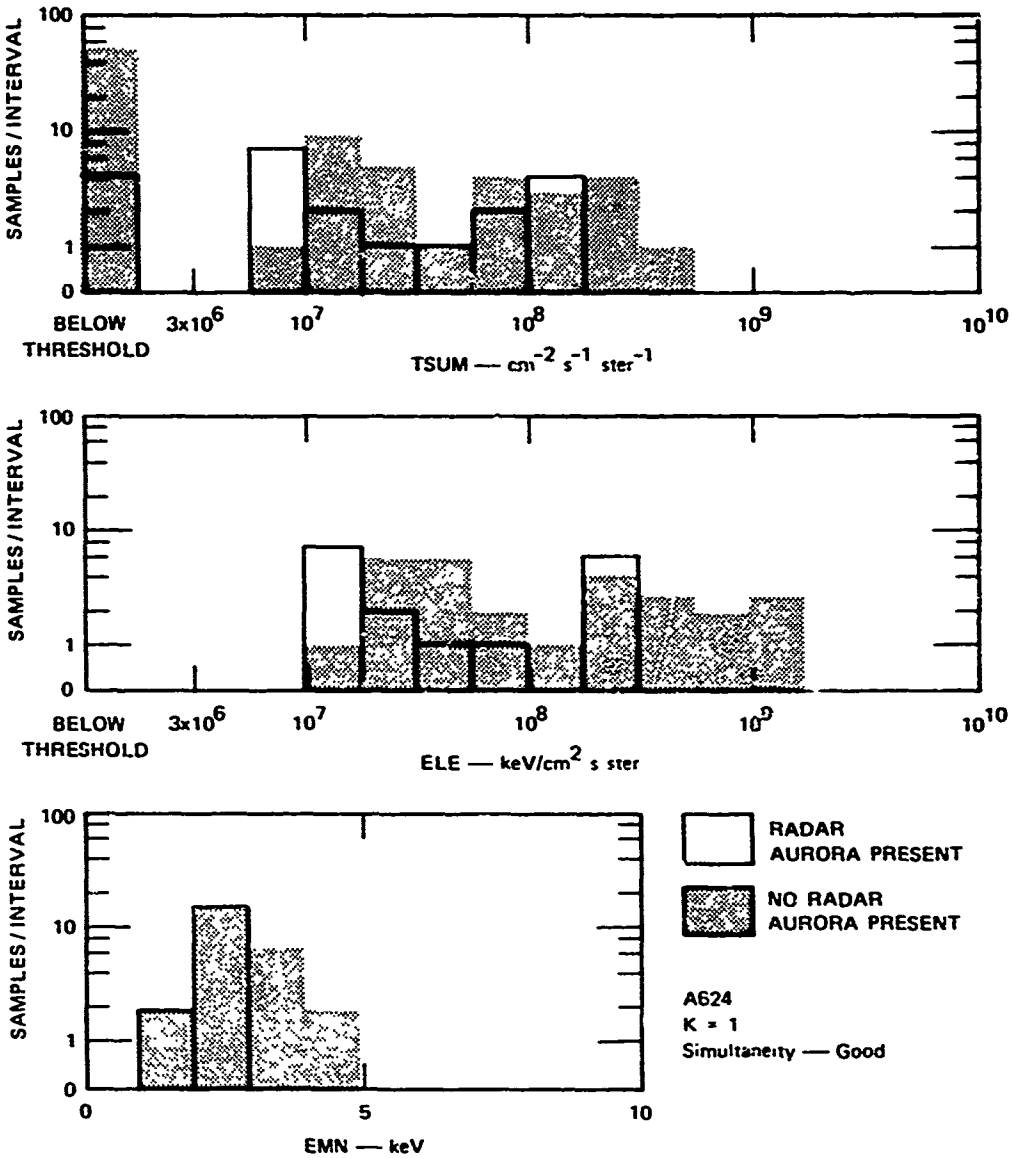

FIGURE 4.E.3 HISTOGRAMS OF LOGARITHMIC OCCURRENCE versus PRECIPITATING ELECTRON NUMBER FLUX (TSUM), ENERGY FLUX (ELE), AND AVERAGE ENERGY (EMN) FOR SATELLITE PASS A624

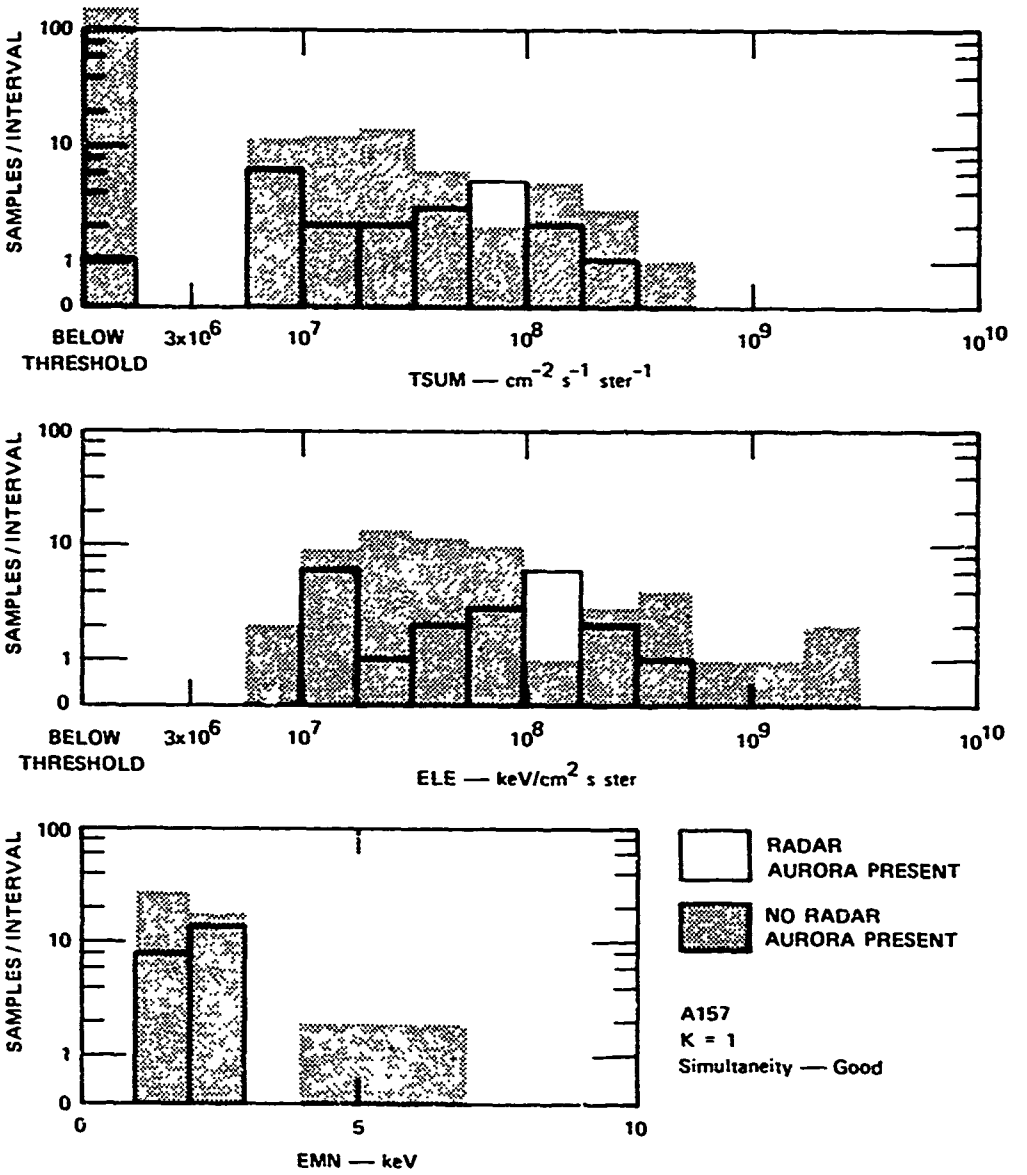

FIGURE 4.E.4 HISTOGRAMS OF LOGARITHMIC OCCURRENCE versus PRECIPITATING ELECTRON NUMBER FLUX (TSUM), ENERGY FLUX (ELE), AND AVERAGE ENERGY (EMN) FOR SATELLITE PASS A157

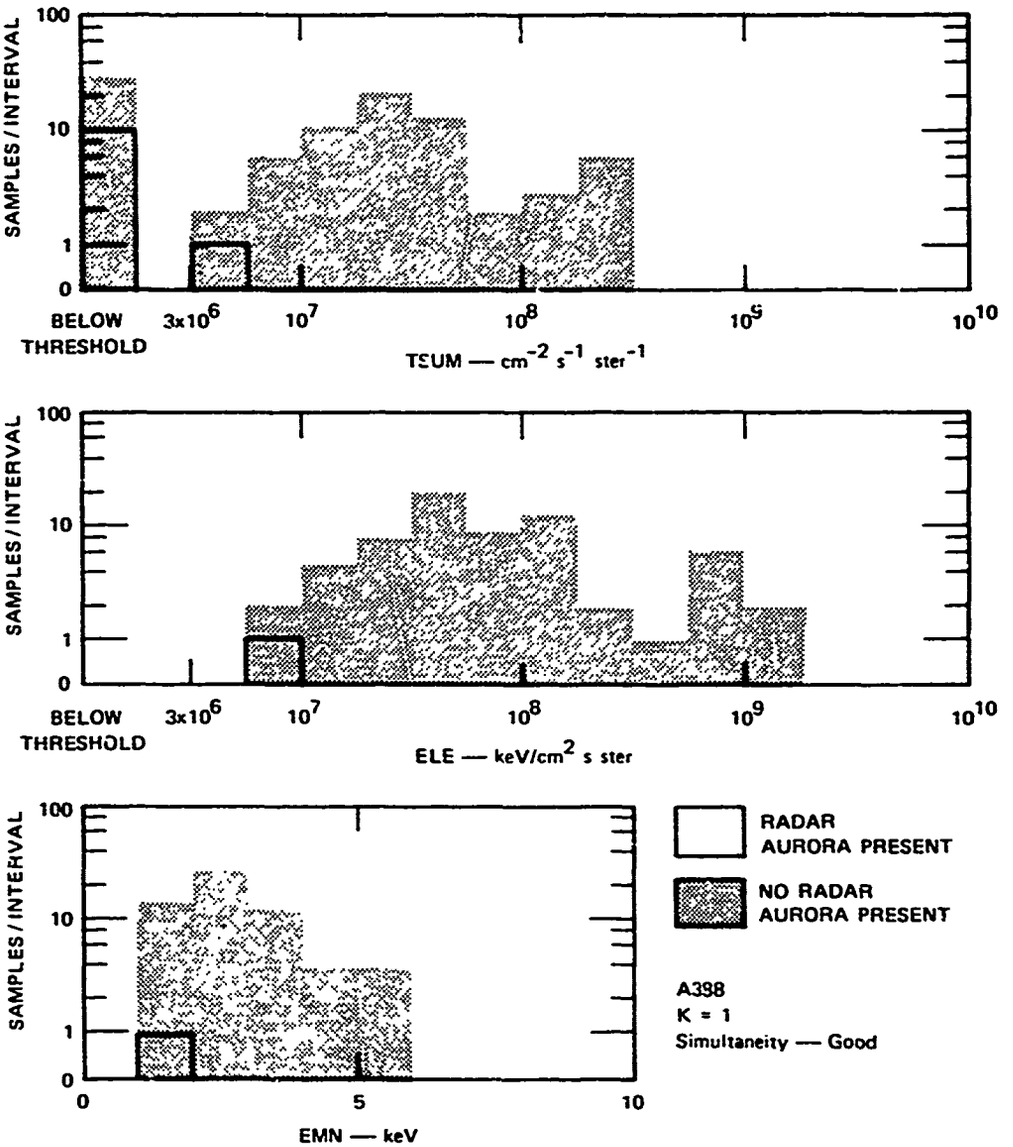

FIGURE 4.E.5 HISTOGRAMS OF LOGARITHMIC OCCURRENCE versus PRECIPITATING ELECTRON NUMBER FLUX (TSUM), ENERGY FLUX (ELE), AND AVERAGE ENERGY (EMN) FOR SATELLITE PASS A388

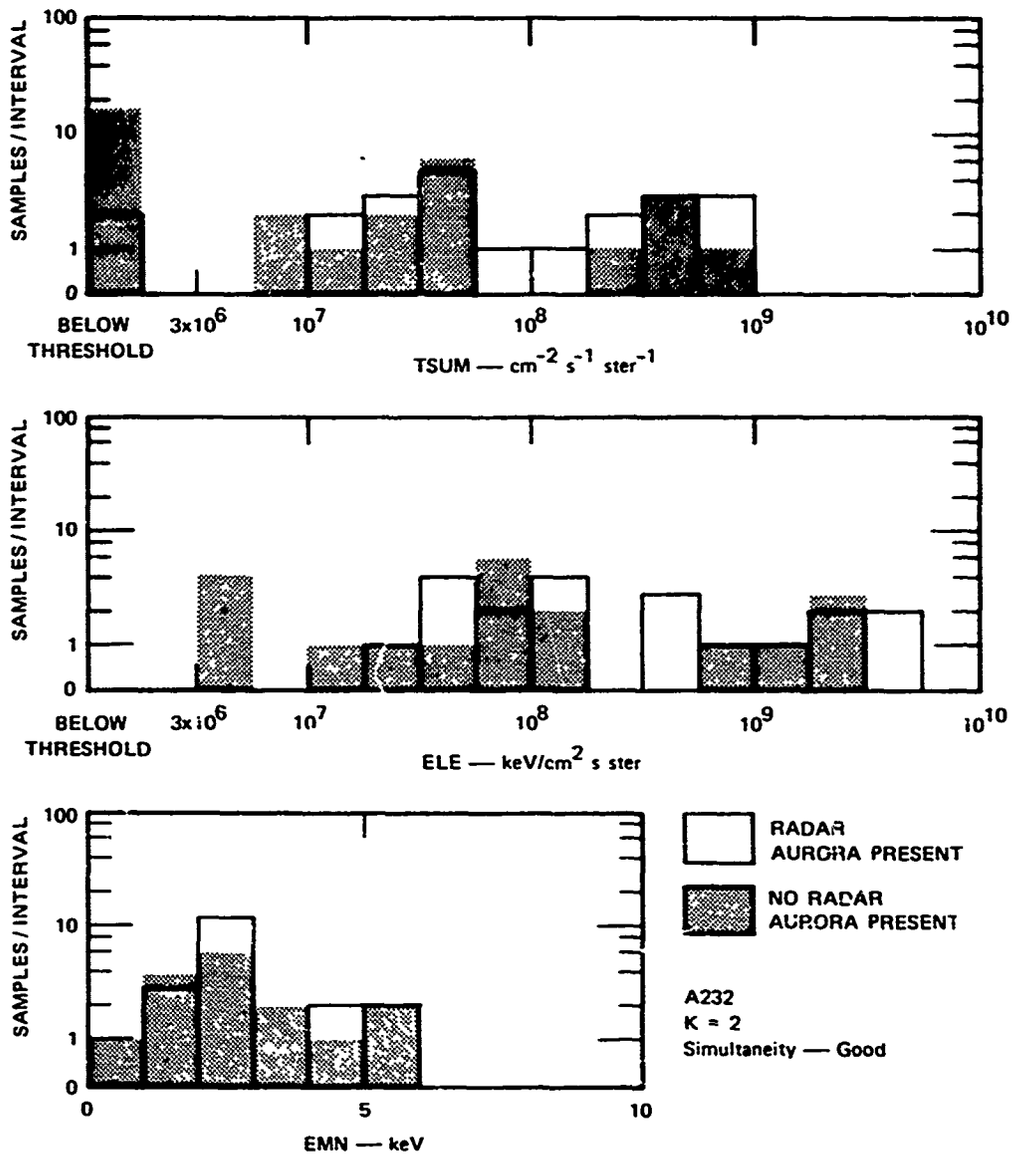

FIGURE 4.E.6 HISTOGRAMS OF LOGARITHMIC OCCURRENCE versus PRECIPITATING ELECTRON NUMBER FLUX (TSUM), ENERGY FLUX (ELE), AND AVERAGE ENERGY (EMN) FOR SATELLITE PASS A232

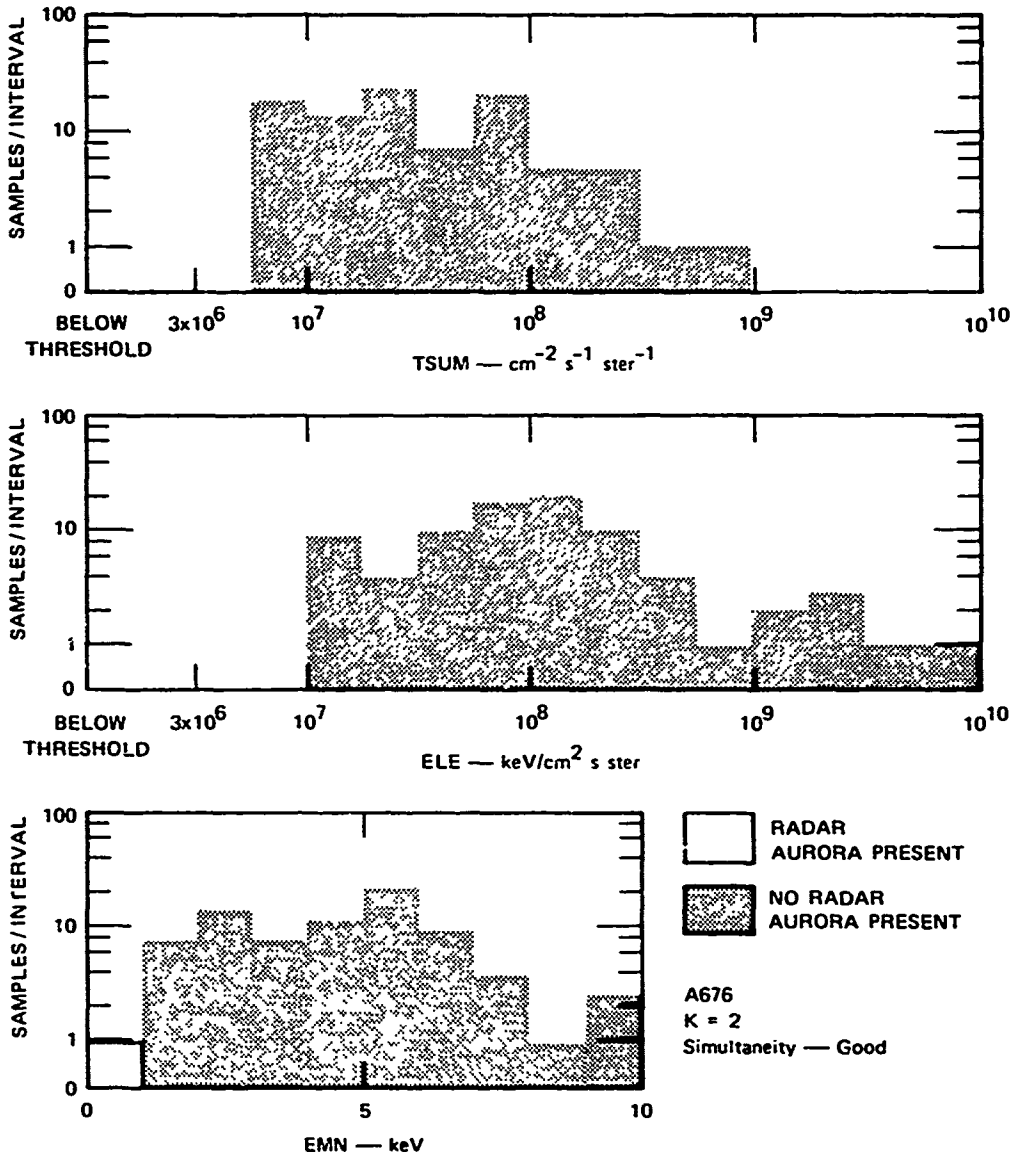

FIGURE 4.E.7 HISTOGRAMS OF LOGARITHMIC OCCURRENCE versus PRECIPITATING ELECTRON NUMBER FLUX (TSUM), ENERGY FLUX (ELE), AND AVERAGE ENERGY (EMN) FOR SATELLITE PASS A676

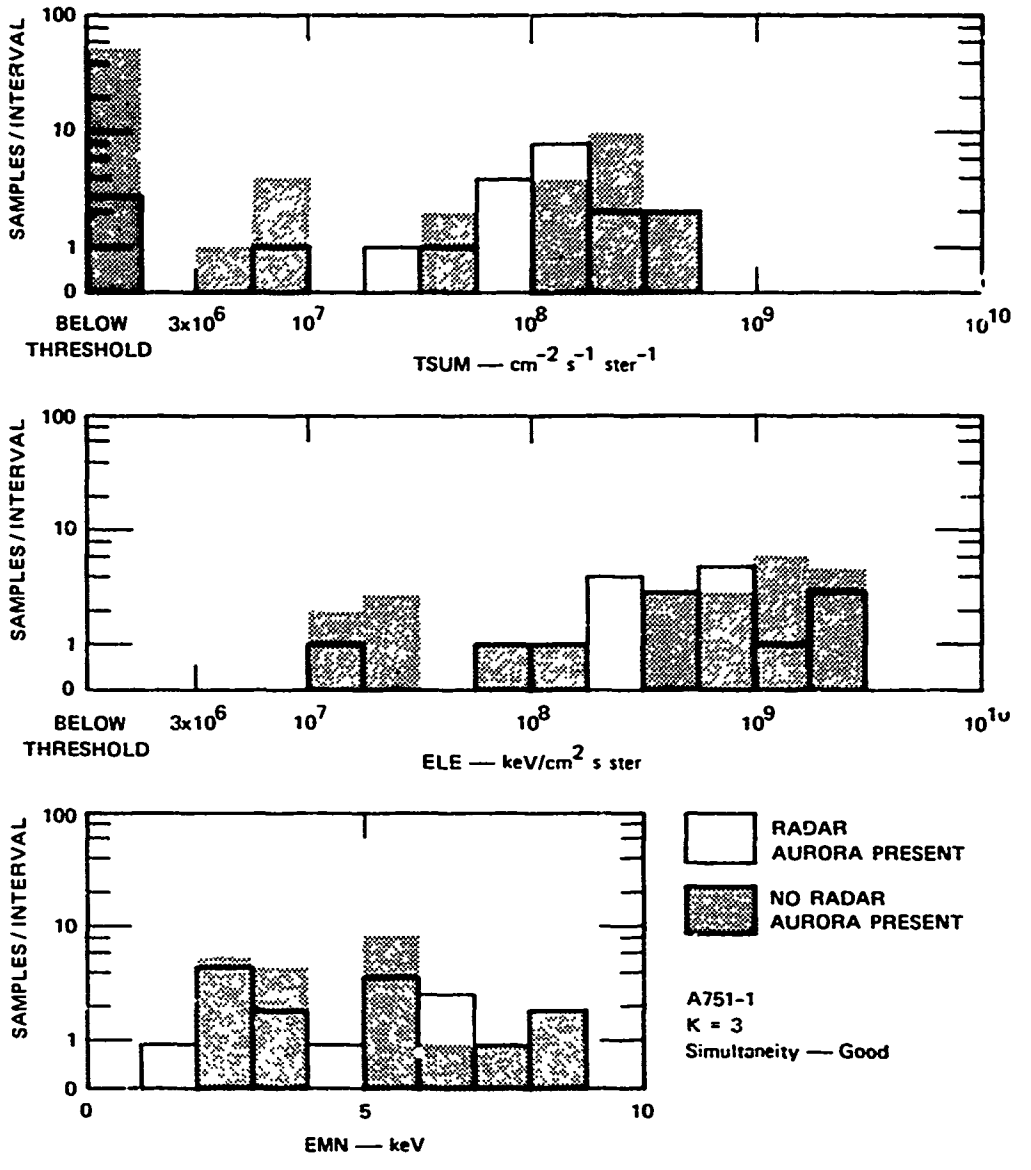

FIGURE 4.E.8 HISTOGRAMS OF LOGARITHMIC OCCURRENCE versus PRECIPITATING ELECTRON NUMBER FLUX (TSUM), ENERGY FLUX (ELE), AND AVERAGE ENERGY (EMN) FOR SATELLITE PASS A751

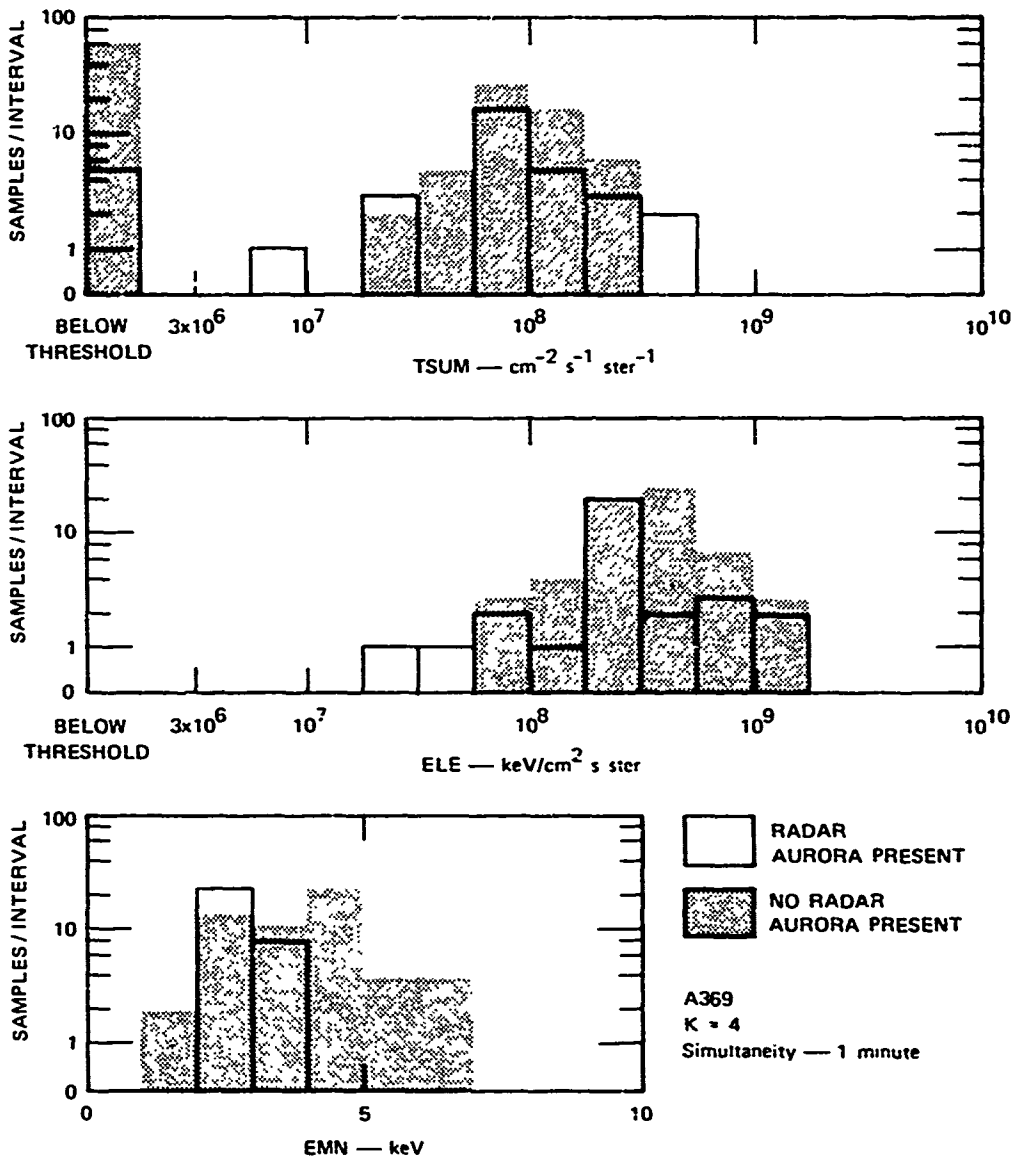

FIGURE 4.E.9 HISTOGRAMS OF LOGARITHMIC OCCURRENCE versus PRECIPITATING ELECTRON NUMBER FLUX (TSUM), ENERGY FLUX (ELE), AND AVERAGE ENERGY (EMN) FOR SATELLITE PASS A369

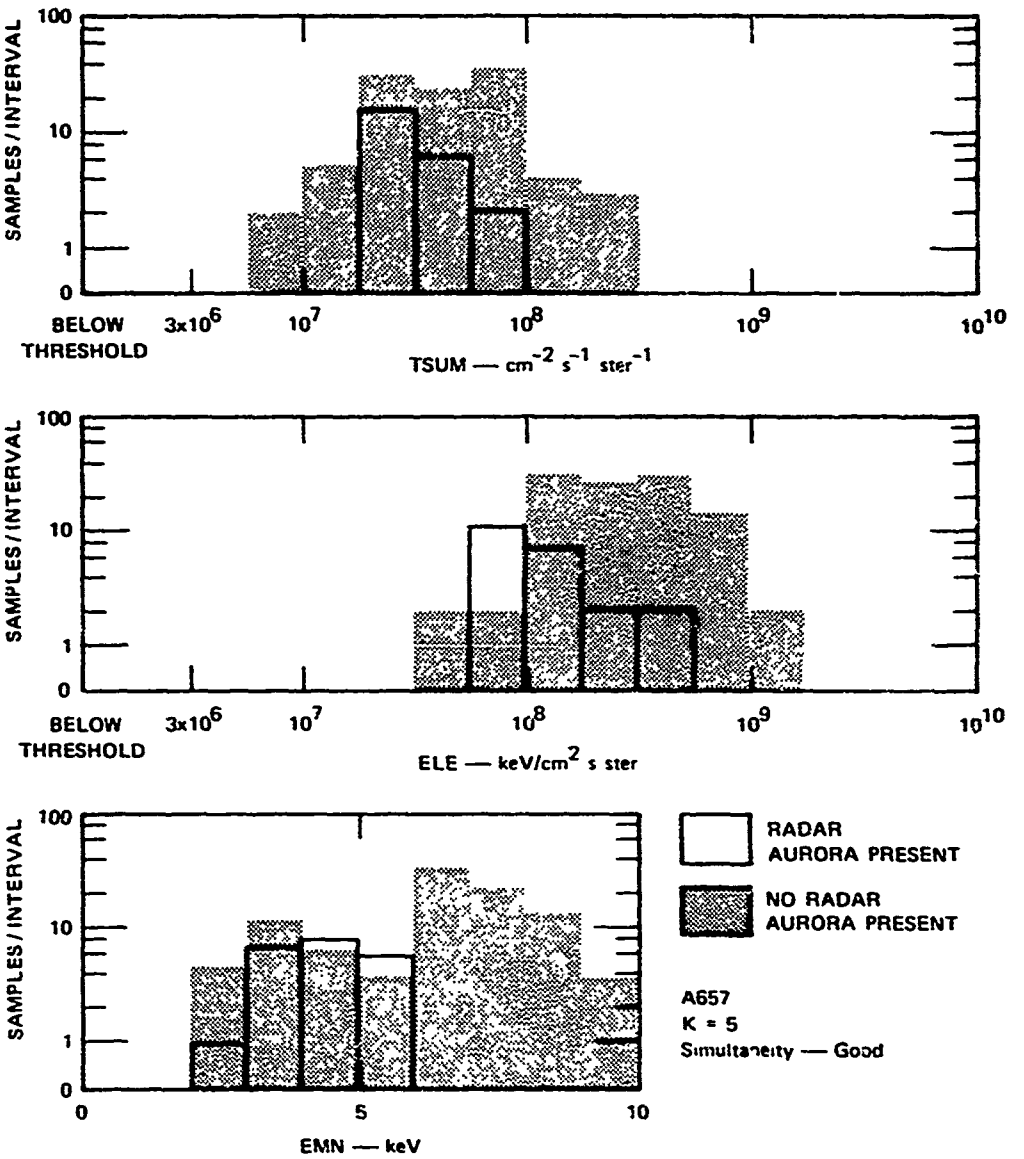

FIGURE 4.E.10 HISTOGRAMS OF LOGARITHMIC OCCURRENCE versus PRECIPITATING ELECTRON NUMBER FLUX (TSUM), ENERGY FLUX (ELE), AND AVERAGE ENERGY (EMN) FOR SATELLITE PASS A657

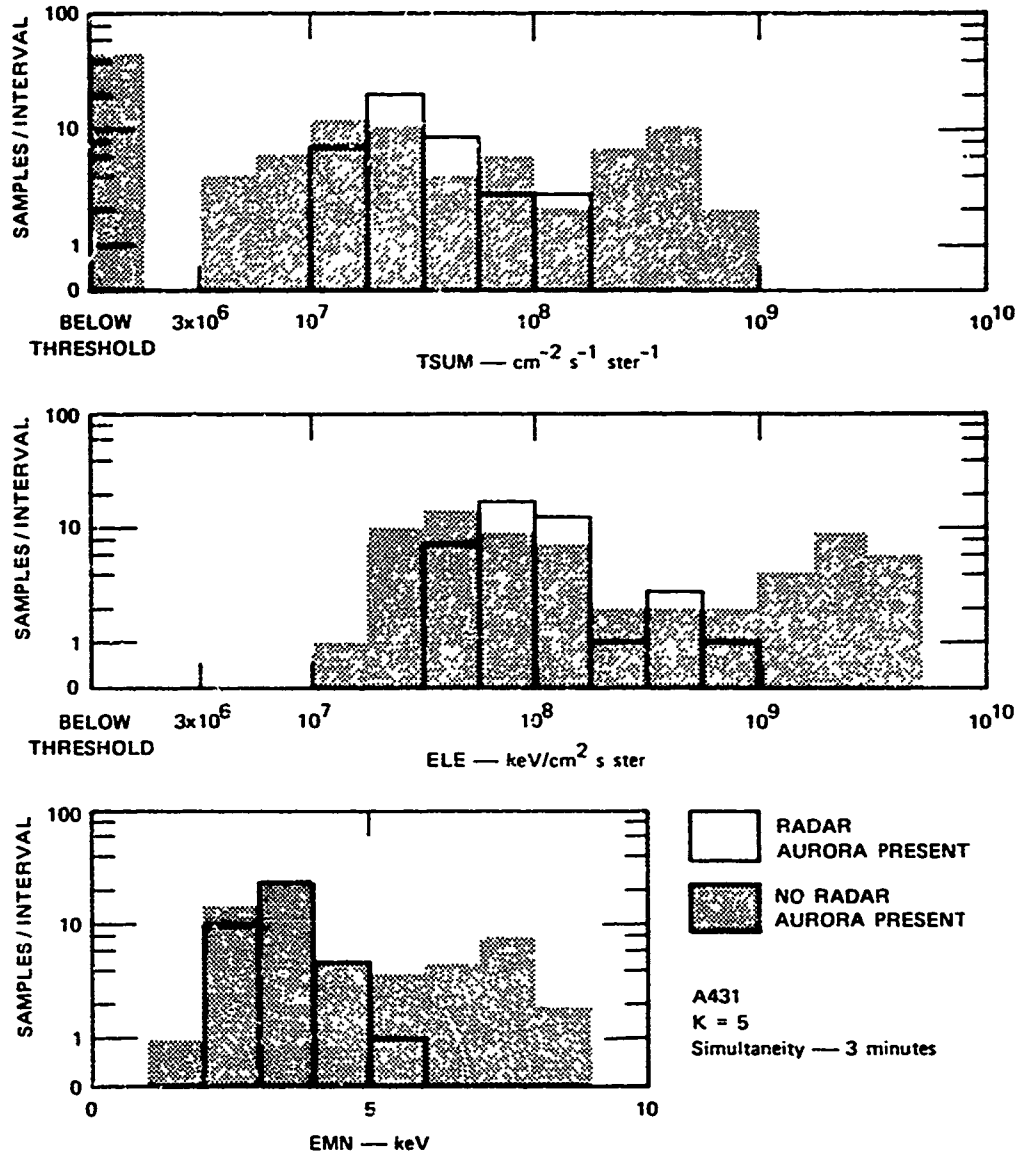

FIGURE 4.E.11 HISTOGRAMS OF LOGARITHMIC OCCURRENCE versus PRECIPITATING ELECTRON NUMBER FLUX (TSUM), ENERGY FLUX (ELE), AND AVERAGE ENERGY (EMN) FOR SATELLITE PASS A431

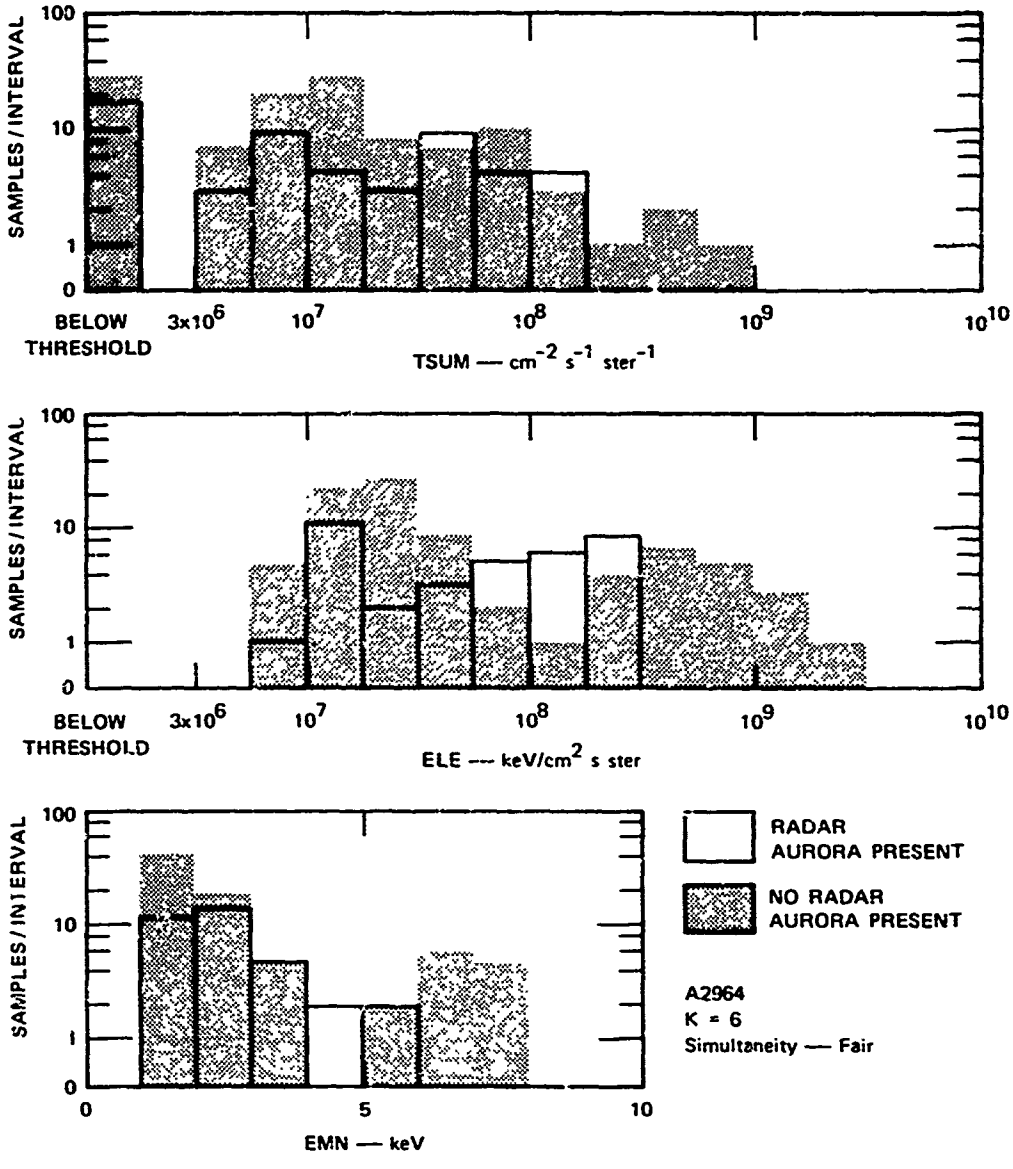

FIGURE 4.E.12 HISTOGRAMS OF LOGARITHMIC OCCURRENCE versus PRECIPITATING ELECTRON NUMBER FLUX (TSUM), ENERGY FLUX (ELE), AND AVERAGE ENERGY (EMN) FOR SATELLITE PASS A2964

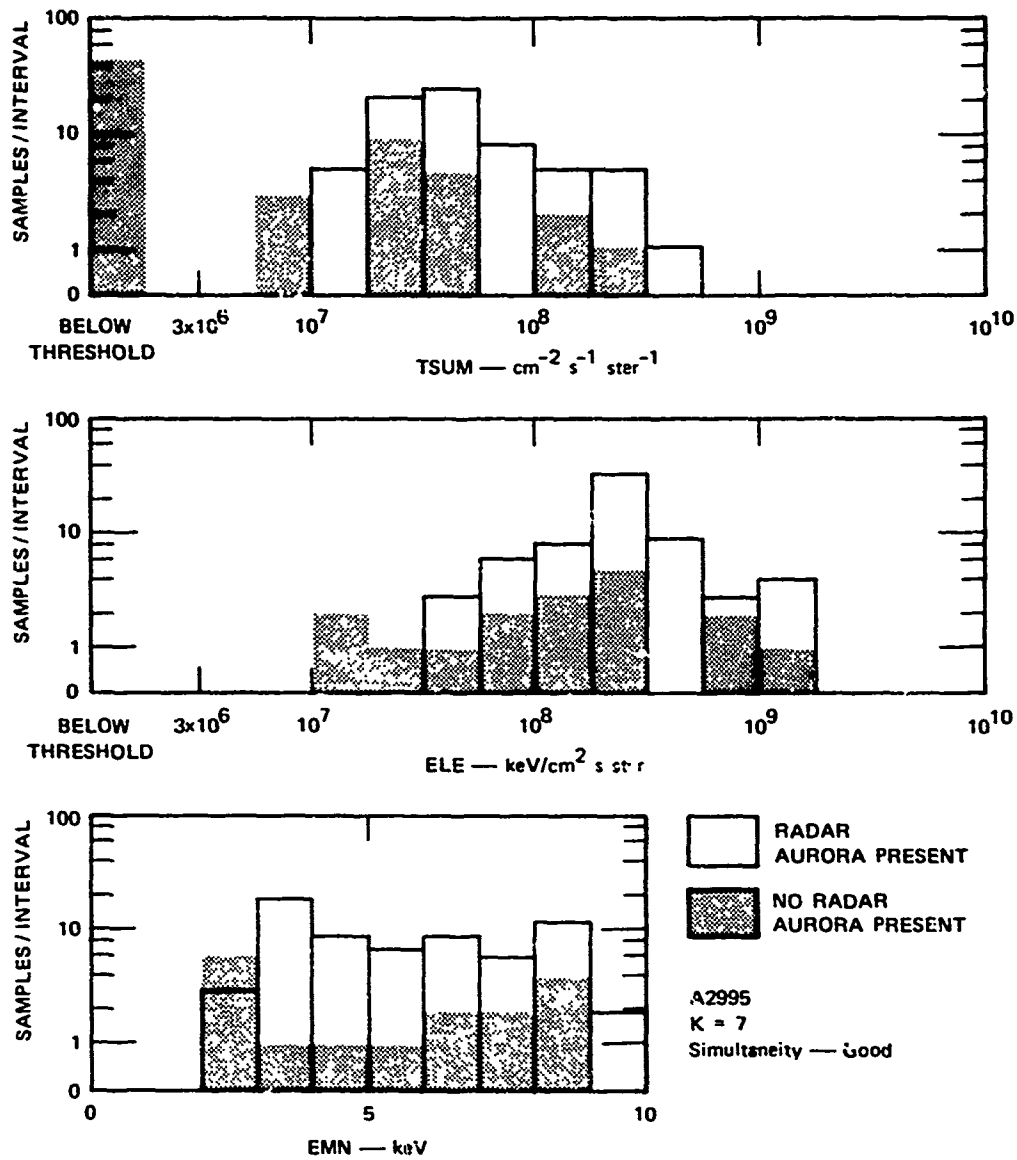

FIGURE 4.E.13 HISTOGRAMS OF LOGARITHMIC OCCURRENCE versus PRECIPITATING ELECTRON NUMBER FLUX (TSUM), ENERGY FLUX (ELE), AND AVERAGE ENERGY (EMN) FOR SATELLITE PASS A2995

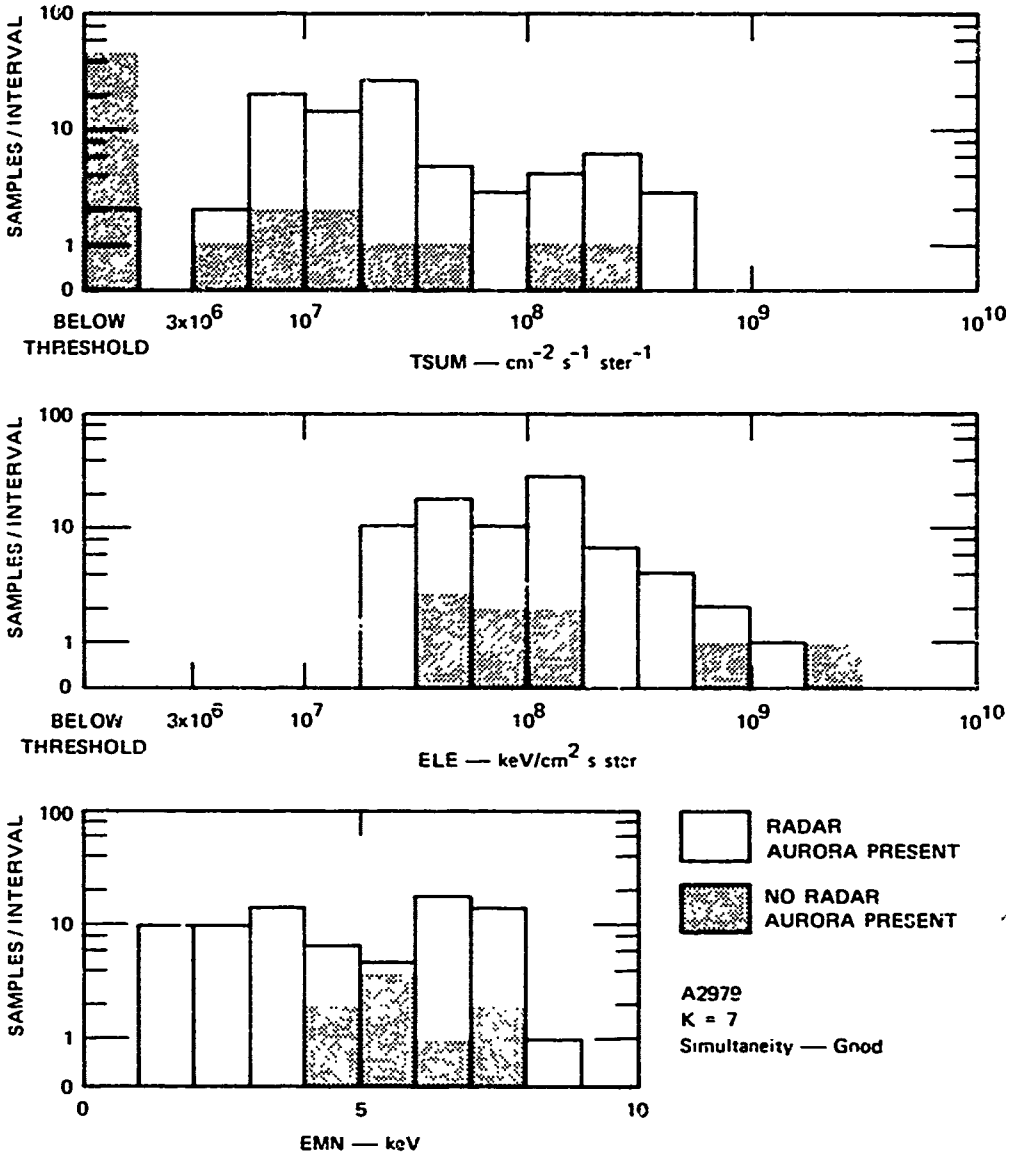

FIGURE 4.E.14 HISTOGRAMS OF LOGARITHMIC OCCURRENCE versus PRECIPITATING ELECTRON NUMBER FLUX (TSUM), ENERGY FLUX (ELE), AND AVERAGE ENERGY (EMN) FOR SATELLITE PASS A2979

5. COMPARISONS OF RADAR AURORA WITH MAGNETOMETER AND ALL-SKY-CAMERA DATA

In this section two other kinds of data correlations that may shed light on the understanding of radar aurora are presented. The first study is a comparison of magnetometer data with radar aurora. The second comparison is between radar aurora and visual aurora as recorded with all-sky cameras.

5.1 Radar-Aurora Magnetometer Comparison

On 24 March 1969 radar data were collected for approximately 5 hours for the purpose of seeking a correlation between radar echoes and magnetometer response for a magnetometer placed below the region from which radar echoes were being obtained. The radar antenna was directed toward the ionosphere at an altitude of 110 kilometers on the magnetic field line that intersected a magnetometer operated by the University of Alaska located at College, Alaska. We present here a composite figure of radar data and magnetometer data; the composite is given in Figure 5.1. The upper portion of the figure gives magnetometer response versus Greenwich Meridian Time for the Z and H components of magnetic field. At the bottom of the field are three amplitude-versus-time traces. The amplitudes are given in dBm. These are radar signal amplitudes obtained with the 139-MHz radar. The amplitudes were measured using a 40-km range gate. The range gates were centered on the magnetic field line through the magnetometer (center trace) and at ranges less than and beyond the magnetometer field line--as indicated in the figure.

Visual inspection of the data presented in Figure 5.1 does not show an obvious correlation between behavior of these two instruments

(radar and magnetometer). The magnetometer samples ionospheric currents over a fairly large north/south extent of the ionosphere. It is probable that our three radar range gates are so close together that the magnetometer averages over effects in all three gates. It must also be remembered that magnetometers respond to current in the ionosphere; it is believed that conditions for the structuring of ionization that leads to radar scattering requires ionospheric electric fields, not electric currents. Therefore lack of an obvious, detailed correlation may not be surprising.

5.2 Radar Aurora--All-Sky-Camera Comparison

The question of relationships between visual aurora and radar aurora has not been unambiguously resolved. There is a tendency, we believe, for radar aurora to be located near to but not necessarily coincident with visual aurora. This relationship has been found on occasion during periods of fairly stable, quiescent aurora. The study of the relation of radar aurora to visual aurora currently requires stable, well defined visual arcs and stable radar aurora. This is because it takes several minutes to accomplish radar scans to map radar aurora. Many aurora will move very great distances during this period of time. It is expected that with the addition of the phased-array radar to the Homer facility, more dynamic aurora can be investigated to seek visual radar relations.

Our experience has shown that radar/visual correlations are only meaningful if the visual data are obtained by triangulation between at least two camera sites. For Alaska this requires inordinately good weather. Otherwise, cloud cover prevents successful acquisition of all-sky data.

Figures 5.2 and 5.3 provide two examples of radar visual correlations. These data were obtained with the 139-MHz radar. The data for

Figure 5.2 were obtained at 12:19 GMT on 24 September 1969. The data for Figure 5.3 were obtained at 12:28 GMT on 10 October 1969. In Figure 5.2, two visual arcs are indicated; these were located by triangulation between all-sky photographs taken at Ft. Yukon and at College, Alaska. The regions of radar return are indicated by the bars located generally to the north of the northern visual arc. We note that the radar returns seem to be adjacent to, but not superposed upon, the visual arc. We note that in the eastern end of the northern visual arc, the visual arc seems to bifurcate the radar echo. The data of Figure 5.3 generally show radar returns that are also bifurcated by the visual arc.

It has been speculated[2] that since radar aurora is thought to be produced by high electric fields, the high conductivity produced by ionization generated by the precipitating particles that cause visual arcs will short circuit these electric fields. In the absence of the electric field, plasma instabilities cannot grow to produce structured ionization that is needed for radar scattering. These visual/radar comparisons seem consistent with this speculation.

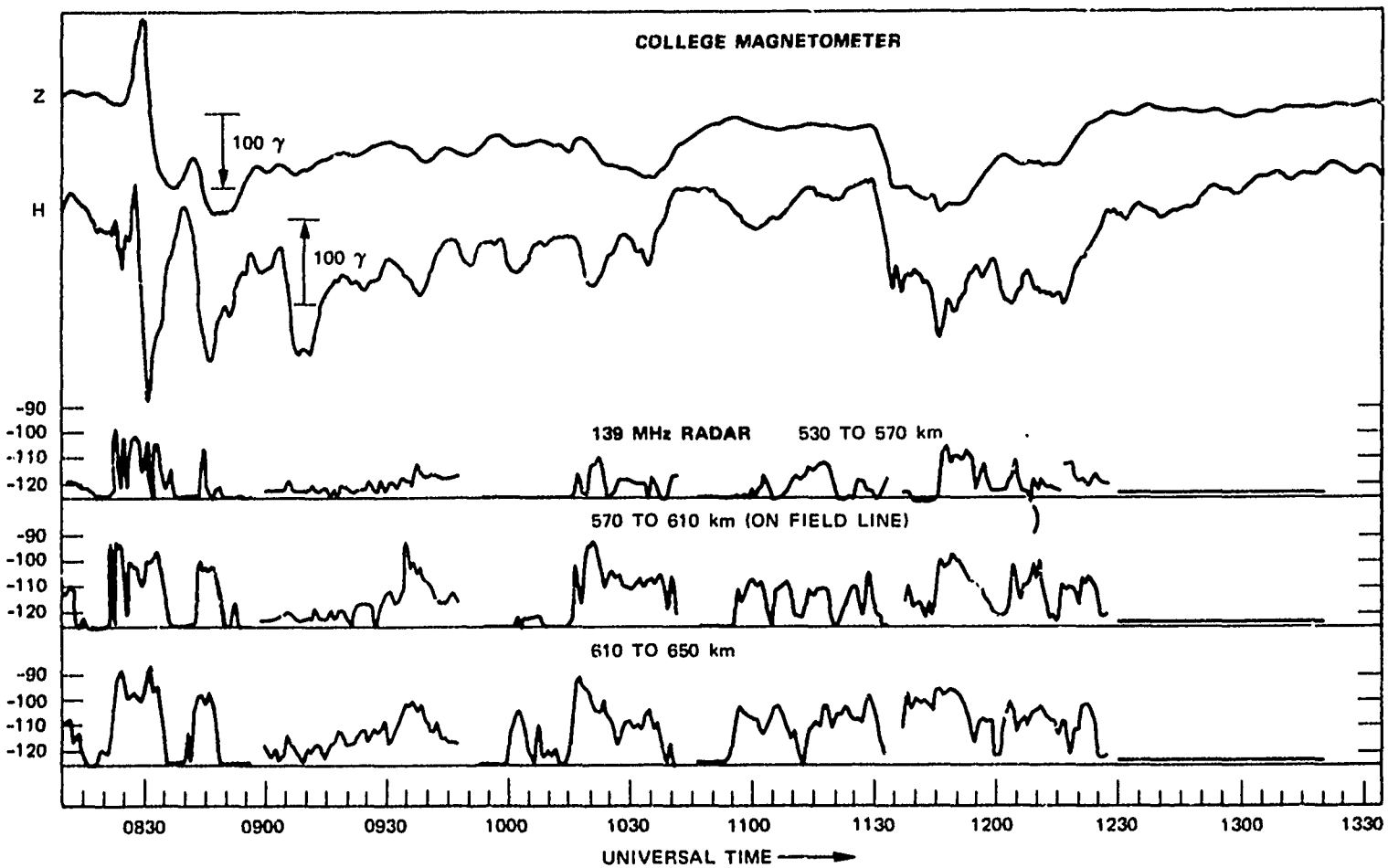

FIGURE 5.1 SIMULTANEOUS AURORAL RADAR ECHO STRENGTH AND COLLEGE, ALASKA MAGNETOMETER DEFLECTIONS *versus* TIME ON 24 MARCH 1969

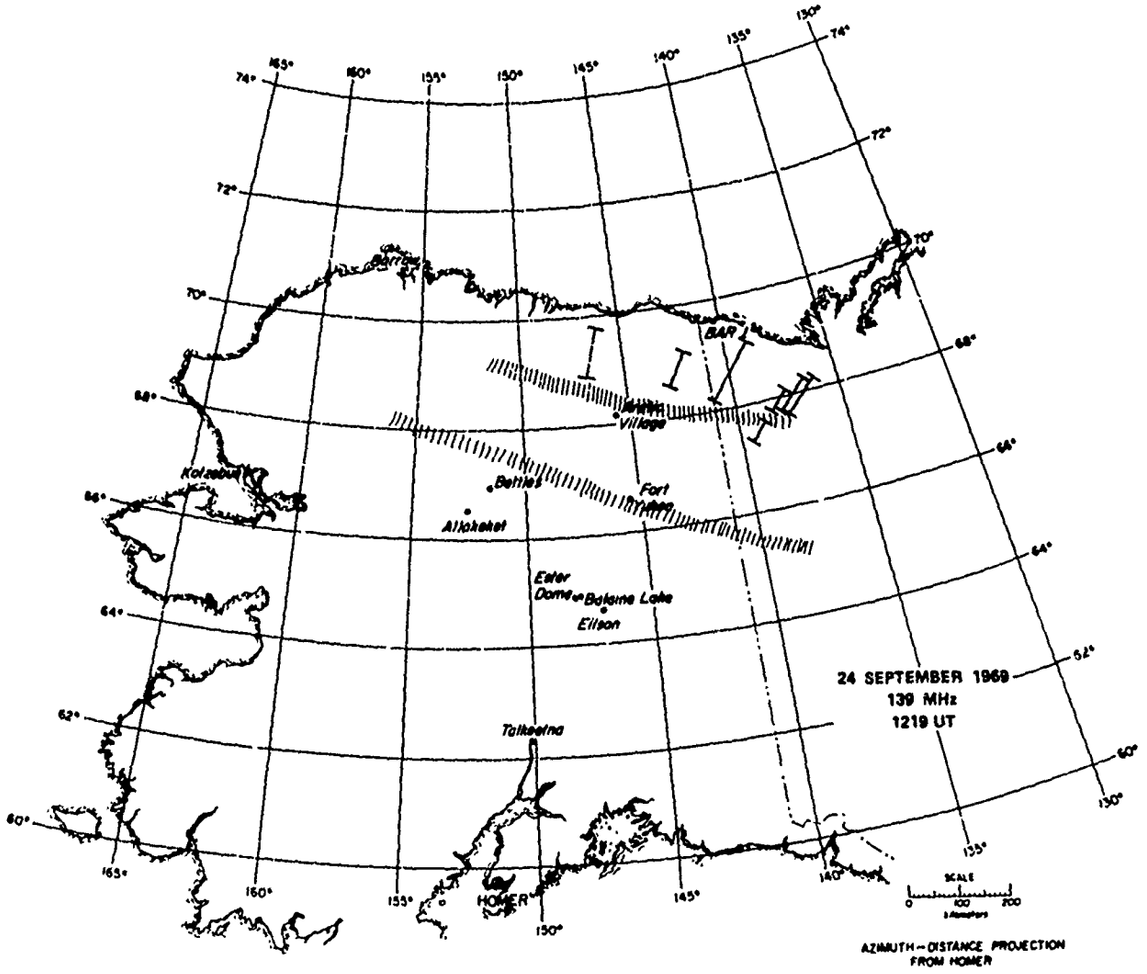

FIGURE 5.2 MAP SHOWING LOCATION OF VISUAL AURORA AND RADAR AURORA AT 12:19 UT, 24 SEPTEMBER 1969. Radar frequency, 139 MHz.

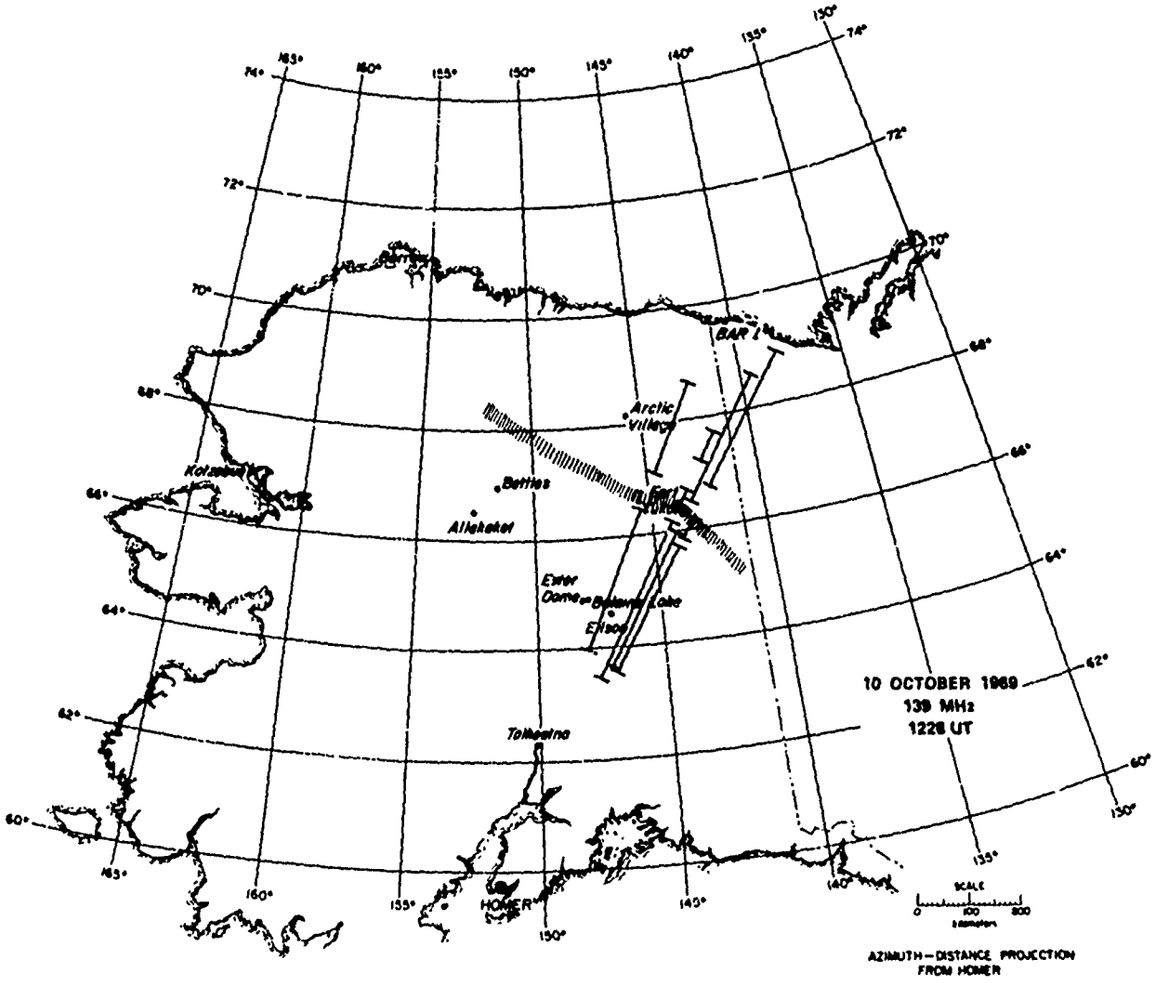

FIGURE 5.3 MAP SHOWING LOCATION OF VISUAL AURORA AND RADAR AURORA AT 12:28 UT, 10 OCTOBER 1969. Radar frequency, 139 MHz.

6. STUDY OF SATELLITE DATA

It is now universally agreed that radar aurora is produced by scattering of radar energy from field-aligned irregularities in E-region ionization. There are several important questions that are continually being addressed. Some of these are as follows:

(1) What produces the E-region ionization (during nighttime)?

(2) What mechanisms produce irregularities in the E-region ionization?

(3) What is the detailed relationship between radar aurora and other auroral phenomena?

In this section we study some of the physics and chemistry of precipitating particle interactions in the ionosphere as background to interpreting the satellite data. We then concern ourselves with preliminary interpretation of the data presented in Sections 4 and 5 as a start in clarifying our understanding of the problems posed as questions above.

6.1 E-Region Ionization Produced by Precipitating Electrons

A question of concern in radar aurora is whether precipitating particles produce the ionization that is necessary for radar clutter echoes when the E-region is not sunlit. Daytime (sunlit) radar aurora can be produced by structuring of normal daytime E-region electrons. We have pursued this question in relation to the satellite precipitation data in order to better understand the production of nighttime E-region ionization required to produce auroral radar returns. The data provided to us by Lockheed only gave the average energy of precipitating electrons.

The detailed spectrum based on their five energy-selecting channeltron counters was not made available to us. Figure 6.1 presents data[6] giving the altitude of maximum ionization rate due to precipitating electrons. The data in this figure are for precipitation at a geomagnetic latitude of 67°. The pitch-angle distribution is assumed to be isotropic over the downward hemisphere. The data of Figure 6.1 are for a monoenergetic electron energy spectrum.

The precipitating electron spectra are not monoenergetic. The proton data to be presented later, as well as the rate of photon-production data for an exponential electron spectrum,[7] reveal deeper penetration than indicated in Figure 6.1 if the altitude of the effect is referenced to average particle energy. That is to say, had we used an exponential spectrum for the electrons and plotted ionization rate versus average electron energy, then the curves in Figure 6.1 would be moved to a lower altitude.

Figure 6.1 indicates by cross-hatching the band of altitudes over which radar aurora is most frequently observed. For monoenergetic electrons with isotropic pitch-angle distribution, energies must exceed 5 keV before ionization is produced in the altitude region of prime concern to radar clutter. Because electron spectra probably have a spread in energy when the EMN from the channeltron spectrometer exceeds 2 kV or so, we presume that ionization will be produced by the electrons in the altitude region of the most frequent and most intense radar clutter.

Since the satellite data provide an absolute flux, it is possible to estimate the E-region electron density produced by the precipitating particles. Figure 6.2 provides some results of these computations. Altitude in kilometers is plotted versus ionospheric electron density for various precipitating electron fluxes. These electron densities are computed at each altitude using a monoenergetic electron beam that produces its maximum ionization rate at that altitude. Thus the computation

at 100 km altitude assumes a monoenergetic electron flux of 17 keV (see Figure 6.1). The calculation for an altitude of 130 km, for example, assumes an electron energy of 2.5 keV.

The steady-state electron density in these calculations was computed assuming that unperturbed atmospheric chemistry is pertinent. The electron clean-up mechanism that dominates the chemistry is disassociative recombination. This reaction varies with altitude, according to data summarized elsewhere.[8] The reaction is also temperature-sensitive so that if the auroral precipitation or the auroral electrojet heat the ionosphere above normal temperatures, higher electron densities than we compute may be produced.

The radar clutter data do not directly reveal the electron density in the scattering regions. Under very special circumstances one can deduce approximate values for this quantity (see Ref. 2). When this is done, values of nighttime E-region electron densities between 10^5 and 10^6 el/cm^3 are found. To produce these densities, according to Figure 6.2, fluxes equal to or greater than 10^7 el/cm^2-s-ster are required. The electron counter threshold, below which Lockheed advised us not to use the data, is 5×10^6. Figure 6.2 indicates, therefore, that when electron precipitation is measured by the satellite above its detection threshold, the precipitation is nearly capable of producing the electron densities that seem to be needed.

Another important question is that of persistence of the ionization produced by precipitation. If the precipitation suddenly turns on, how long does it take until the ionospheric electron density reaches the steady-state electron density as determined from Figure 6.2? Figure 6.3 presents altitude versus chemical time-constant for the electron-precipitation fluxes described by Figure 6.2. In the altitude region of concern (105 to 115 kilometers), Figure 6.3 indicates that chemistry

lifetimes are shorter than 20 to 30 seconds for the satellite electron precipitation threshold of 5×10^6. We conclude from this figure and Figure 6.2 that the electron densities produced by electron precipitation as measured by the Lockheed satellite are great enough and can be produced in a sufficiently short time to explain the presence of electrons at E-region altitudes during the nighttime when auroral clutter is observed. We study later whether there is spatial overlap of measureable electron precipitation and radar aurora.

6.2 E-Region Ionization Produced by Precipitating Proton

As with electron precipitation we ask the question, do precipitating protons produce enough E-region ionization--in the absence of sunlight--to explain radar auroral clutter when clutter and proton precipitation spatially overlap? To investigate this we have plotted data obtained from Chamberlain.[9] The data are for an exponential (in energy) proton spectrum, and an isotropic pitch-angle distribution in the downward-going hemisphere. The results are presented in Figure 6.4. Also indicated is the altitude at which the ionization production rate is 10 percent of the peak value. The upper-altitude 10-percent region is so high it was not plotted.

To aid in understanding penetration of a continuous spectrum compared with the monoenergetic spectrum that was used for the electron precipitation, the stopping altitude for monoenergetic protons with zero pitch angle was also plotted in Figure 6.4. The isotropic pitch angle distribution would tend to raise the altitude of peak ionization with respect to this latter, zero-pitch-angle curve. The high-energy tail of an exponential spectrum moves the altitude of peak ionization rate downward into the atmosphere, if one plots peak ionization rate versus <u>average</u> proton energy. We note that the proton average energy must exceed about

10 keV in order to produce ionization in the altitude band of most frequent and intense auroral radar clutter.

As we interpret the data provided in Ref. 9 we can only compute the average electron density produced by a proton exponential energy spectrum with average energy at 32 keV. Using the reaction rates of Ref. 8 we have plotted the electron density versus proton flux in Figure 6.5. We assume that a background ionization density of 10^5 el/cm^3 is needed to explain auroral clutter; Figure 6.5 indicates that the proton flux would have to exceed 5×10^6 in order to produce the needed ionization in the absence of solar (daytime) E-region ionization.

It is important to note that precipitating protons can undergo a process that is not available to the electrons. A precipitating proton can pick up an electron from an atmospheric atom and thereby become a neutral particle. Once the proton is neutralized it is no longer constrained to follow the earth's magnetic field lines. On deeper penetration of the atmosphere, the neutral proton may again become ionized. By this process the protons can migrate across magnetic field lines. Therefore, proton fluxes that are measured by the satellite at altitudes of about 400 km may be spatially spread by charge exchange by the time the proton reaches altitudes of 100 to 120 km. As a result, a localized peak in proton flux measured at an altitude of 400 km may become spatially spread by 100 km or more by the time the protons reach E-region altitudes. Estimates of E-region ionization that may be produced by proton precipitation as measured by the satellite must be spatially averaged along the satellite path in some manner. We have not pursued this question in any more than qualitative depth at this time.

6.3 Correlation of Radar Echoes with Satellite-Borne Particle-Precipitation Measurements

In this subsection we compare some results of the simultaneous measurement of radar aurora and particle precipitation. In particular, we compare locations of peak energy flux with locations of radar aurora. In some sense, this kind of measurement may be redundant with radar/all-sky camera comparisons, in that it would be expected that spatial peaks in satellite-measured electron precipitation would give rise to discrete auroral forms that would be recorded by all-sky cameras as visual arcs. Other investigators have not been able to well substantiate this relation, but few believe the relationship should not exist. We shall also study the question of whether satellite-measured precipitation is sufficient to provide the ionization that must exist in regions from which we obtain radar echoes if these echoes are to be observed.

6.3.1 Correlation of Regions of Peak Energy Flux with Locations Radar Aurora

The data from 14 satellite passes have been studied to seek a variety of correlations. Table 6.1 presents one set of correlations of these data. The first column of Table 6.1 identifies satellite pass number.

We have categorized the type of auroral event that was occurring in Column 2 according to the nature of the satellite precipitation data. If there is no symbol, the event was a weak precipitation event, meaning that the particle fluxes were quite low but were measurable in some parts of the trajectory. If, in our judgement, the energy flux of electrons (not the number flux) was large, then we have placed an E in this column. If proton precipitation was weakly observable over a reasonable portion of the orbit, we have placed wp, meaning moderate to weak total proton energy. Three events have been labeled with a P because

Table 6.1

COINCIDENCES AND ANTI-COINCIDENCES BETWEEN RADAR AURORA AND PEAKS IN ENERGY PRECIPITATION FROM SATELLITE MEASUREMENTS

Sequence Number	Pass Number	Type of Auroral Event*	3 Hour Magnetic Index-K	Electron Precipitation			Proton Precipitation			Simultaneity in Time of Radar Measurements and Satellite Pass
					Anti-Coincidence			Anti-Coincidence		
				Coincidence	Radar	Electron Peaks	Coincidence	Radar	Proton Peaks	
1	A518	--	0	2	0	0	0	2	1	Satellite data 7 min. earlier than radar data
2	A641	--	0	0	3	2	No protons	No protons	No protons	Satellite data 15 min. earlier than radar data
3	A624	--	1	1	1	2	0	2	1	Good
4	A157	--	1	1	1	5	0	2	1	Good
5	A388	E	1	0	1	Widespread outside radar's view	0	1	1	Good
6	A232	E, wp	2	1	1	1	0	2	1	Good
7	A676	E	2	0	1	2-3	0	1	1	Good
8	A751	E	3	?	?	Several	0	2	1	Good
9	A369	E, wp	4	3	1	Widespread	0	4	1	Radar 1 min. late-- radar aurora moving south
10	A657	E, wp	5	0	1	Many peaks	0	1	1	Good
11	A431	E, P	5	0 to 1(?)	4-3(?)	Many peaks	0	4	1	Satellite data 3 min. earlier than radar data
12	A2964	E	6	1-2(?)	2-1(?)	0-1	0	2	0	Fair
13	A2995	E, P	7	Widespread	Widespread	Widespread	Widespread	Widespread	Widespread	Good
14	A2979	E, P	7	Widespread	Widespread	Widespread	Widespread	Widespread	Widespread	Good

*E--fairly large total electron energy flux; P--fairly large total proton flux; wp--moderate to weak total proton energy.

the proton energy flux was very large. For our own work we have named these "proton events."

The next column gives the College, Alaska three-hour magnetic index for the period of the satellite pass.

In the electron-precipitation columns we have defined collocation of electron energy peaks and radar aurora as coincidences. This means that radar aurora seemed to be located in the same regions in which there is a local maximum in the energy flux of precipitating electrons. We have also counted the number of isolated radar aurora and peaks in electron energy flux that were not associated with each other, and have called these anti-coincidences. We have done the same for proton precipitation. The last column gives a measure of the simultaneity of the radar and satellite measurements (on some passes the ephemeris data available at the time that our data were reduced were less accurate than we would have desired).

The determination of these correlations is extremely subjective. In some areas there will be many, closely spaced, intense precipitation peaks. In some cases the radar auroral boundary may be located at the particle-precipitation peak. We have tried to be consistent in calling these coincidences. The subjectivity of the interpretation should be evident by the way we have filled out our columns.

Our attempts to redo the electron precipitation columns always produce a slightly differing coincidence set--that is to say, our estimation procedure is very subjective. This is very disturbing, but we have not discovered a way to uniquely define precipitation peaks. Our reevaluation of coincidences--though very subjective--does show a tendency for radar aurora to be anti-coincident with peaks in electron-energy precipitation except for the cases of very active aurora.

Examination of Table 6.1 as given here reveals the following:

- In the auroras that we have not categorized as proton events and not labeled as P, there are no coincidences between radar returns and peaks in proton precipitation.
- There are some coincidences between peaks in electron-energy fluxes, but there are many more anti-coincidences.
- For two of the proton events, since radar aurora is nearly everywhere, there are many peaks in energy deposition, so that coincidences are everywhere and therefore may not be meaningful.
- The electron-coincidence enumeration suggests to us that coincidences between peaks of electron precipitation with radar aurora is almost a random phenomenon. There appears to be no clear-cut, absolute trend, though there are more "valid" anti-coincidences than valid coincidences.

In summary, we believe the data in Table 6.1 indicate that except for intense proton events, radar aurora is not coincident with peaks in proton energy flux. Peaks in electron precipitation may or may not be coincident with radar aurora; we have not discerned a meaningful trend, although there seems to be a tendency toward anti-correlation.

We believe ionospheric electric fields play a role in causing radar aurora. Electric fields are caused by convecting magnetic fields. If the ionospheric ionization is great enough, then magnetic-field convection is slowed in the highly conductive ionosphere. Nearby,

where ionospheric electron densities are lower, large electric fields are not short-circuited by high conductivity. One might therefore expect that at locations where particles are heavily precipitating, ionospheric electric fields will be short-circuited and there will be no structuring of ionization into irregularities and therefore no radar scattering. Thus, during moderate auroral activity, regions of most intense (by particle number) precipitation should not coincide with regions of radar echoes.

On the other hand, if magnetic-field convection becomes extremely intense, even in regions of large precipitation (and therefore high E-region electron densities) electric fields may reach and exceed a threshold for production of plasma instabilities that lead to generation of E-region irregularities.

Therefore correlation between peaks in precipitation intensity along the satellite path and no radar aurora at the same location might be found at times of moderate or weak auroral activity. During strong aurora one might seek and find an inverted relationship. Table 6.1 does not support this hypothesis.

As an alternative approach to organizing data corresponding to the above intuitive guidelines, the histograms of Figures 4.E.1 through 4.E.14 were made. If the above ideas concerning electric-field short-circuiting in regions of high energy precipitation were valid, then the histograms should show more energy precipitated (larger ELE values) in regions where no radar aurora was observed. Examination of these histograms is consistent with this hypothesis except for five passes. Passes A518 and A641 seem inconsistent, but the time simultaneity was poor. Passes A232, A751, and A369 are not consistent with the hypothesis. Passes A2995 and A2979 are consistent in the sense that these passes occurred during very active aurora.

Examination of the other histograms of Figures 4.E.1 through 4.E.14 show no other obvious consistency or trend.

An additional attempt to reveal some relationship between precipitating electrons and the presence or absence of radar aurora in the same region of space was made by computing average quantities from the histograms of Figures 4.E.1 through 4.E.14. Figures 6.6 and 6.7 provide summaries of averages obtained from the histograms.

The top subfigure of Figure 6.6 presents average TSUM for each satellite pass plotted against sequence number according to ascending three-hour magnetic K index. Open circles are the average TSUM for the regions of the satellite pass where radar echoes were simultaneously observed; solid points are for the regions of the pass where no radar echoes were observed. On Pass A676, which is number 7 in our ordered sequences of passes, no electrons were measured above counter threshold in regions where radar echoes were observed. Thus, no point is plotted there for radar echoes. The middle subfigure presents the same kind of data for the average electron power (ELE). The bottom subfigure presents the average electron energy as a function of satellite pass according to ascending three-hour K index. In the bottom figure we have provided a linear regression fit to the data points. The fit for the data without radar echoes is shown as a solid line. The fit to the points corresponding to radar echoes present is shown as a dashed line. The fit was made with sequence number as abscissa; the fit serves only to dramatize similarities and differences between average electron energy in regions of radar aurora and in regions of no radar aurora.

Figure 6.7 plots the ratio of the various average quantities of Figure 6.6 versus satellite sequence number. The top subfigure in Figure 6.7 presents the ratio of TSUM from regions of radar aurora to the average TSUM in regions of no radar aurora. This ratio is then plotted versus satellite sequence number. The middle subfigure presents

this ratio for ELE. The bottom subfigure presents the ratio of average precipitating electron energy in radar regions to that in other precipitation regions.

The top subfigure of Figure 6.7 gives the impression that, on the average, the precipitating electron number flux is lower in regions of radar echoes than in other regions. In fact, this is only true in 8 of the 14 passes. However, the geometric mean of the 13 useable passes (Pass A676 had no electron precipitation in regions of radar aurora) is 0.81, meaning that in expectation the average number flux of the precipitating electrons in radar scattering regions is 80% of that for electrons precipitating elsewhere.

The data from Figures 6.6 and 6.7 concerning the energy flux (ELE) seem to show more definitive differences between precipitation characteristics where radar echoes were obtained and where they were not. During only three passes of 14 was ELE greater in regions of radar aurora. If this ratio was a random quantity, then the probability that three or fewer passes as we have found would have ratios greater than 1.0 is only 2.9%. The ratio measured on two of these passes was only slightly greater than 1.0. The geometric mean of the 13 calculable ratios is 0.55, suggesting that, on the average, the energy flux is only half as great in regions of radar echoes as it is elsewhere where precipitation intensity is above the satellite threshold. This averaged characteristic is consistent with our often-stated hypothesis that more precipitation produces more ionization, resulting in short-circuiting of ionospheric electric fields.

The data plotted in the bottom subfigure of Figure 6.6 show a decided precipitating electron energy trend with 3-hour magnetic K index. The data suggest--and the corresponding subfigure of Figure 6.7 further support--an indication that on the average, electrons that

precipitate into regions from which radar echoes arise have lower energies than do electrons that precipitate elsewhere. On 8 of the 13 useable passes the average precipitating electron energy was lower in regions of radar aurora than elsewhere. On two passes the average energies were the same in the radar and non-radar regions. On three passes the average electron energy was greater in regions of radar aurora--but the largest ratio computed was only 1.08--which value just barely exceeded 1.0. From these data we compute a geometrical mean energy ratio of 0.84.

6.3.2 Production of Nighttime E-Region Ionization by Particle Precipitation

The previous section showed that regions of peak energy deposition did not seem to be located, necessarily, in regions where radar echoes were obtained. In this subsection we study whether any precipitation at all was occurring in the radar-reflecting regions, to determine whether particle precipitation can explain the existence of nighttime E-region ionization necessary for these reflections.

All 14 satellite passes occurred during E-region darkness. Radar aurora requires the presence of E-region ionization. Studies of radar/visual aurora correlation show that the visual forms do not necessarily correlate well in position with radar returns. One is therefore led to wonder what produces the ionization that is necessary for radar scattering. The concern here is whether there is any particle precipitation at all in regions from which auroral echoes are obtained.

The particle-flux precipitation in regions from which radar echoes were being obtained have been investigated even if these were not regions of peak energy flux. Table 6.2 presents these results. On two of the passes listed in the table there were radar echoes from regions in which particle-precipitation levels were below the detection threshold of the satellite. On pass A641 the simultaneity of the

Table 6.2

COINCIDENCES AND ANTI-COINCIDENCES
BETWEEN RADAR AURORA AND MEASURABLE PARTICLE PRECIPITATION

Sequence Number	Pass Number	Number of Radar Clutter Regions	Measurable Electron Precipitation in Region of Radar Aurora	Measurable Proton Precipitation in Region of Radar Aurora	Simultaneity in Time of Radar Measurements and Satellite Pass
1	A518	2	Yes	No	Satellite 7 minutes early
2	A641	3	No	No	Satellite 15 minutes early
3	A624	2	Yes	No	Good
4	A157	2	Yes	No	Good
5	A388	1	No	No	Good
6	A232	2	Yes	Yes	Good
7	A676	1	Yes	No	Good
8	A751	2	Yes	No	Good
9	A369	4	Yes	2 Yes 2 No	Radar 1 minute late--radar aurora moving south
10	A657	1	Yes	No	Good
11	A431	3	Yes	2 No 1 Yes	Satellite 3 min early
12	A2964	2	Yes	No	Fair
13	A2995	4	Yes	Yes	Good
14	A2979	1	Yes	Yes	Good

measurements was poor due to poor pre-pass ephemeris data, so that comparisons probably are not too meaningful. On Pass A388, 11 of 12 satellite data points showed no detectable electron or proton precipitation above our imposed thresholds where radar echoes were being obtained. However, in this case the particle flux nearby was decaying very slowly as the satellite approached the scattering regions. We are led to believe, but cannot prove, that the particle flux was below, but very near, the threshold detection level. On Pass A2979 the satellite data supplied to us by Lockheed does not extend as far as our radar echoes. Thus, lack of displayed precipitation in the most southerly portion of the radar echo is not of any significance.

We estimate that, provided particle energy is great enough to penetrate to 110-km altitude, the threshold detection flux of the satellite counters produces at this altitude an electron density of about 7×10^4 if the particles are electrons, and 2×10^4 if the particles are protons. These data suggest that there was some particle precipitation flux wherever radar aurora was found. The data of Table 6.2 and our other inferences imply that the nighttime, widespread particle precipitation as measured by the OV1-18 during our 14 passes is adequate to produce the ionospheric electron densities needed to explain observed radar aurora.

6.4 Discussion of Correlation Study and Other Possible Relationships

When comparing particle precipitation with radar echoes, the question arises whether one should compare energy flux or particle number flux deposited. We presume but cannot prove that the energy flux is a measure of the local strength of the auroral disturbance. From a radar point of view the particle-number flux is a measure of the generation of E-region ionization.

The particle energy spectrum is an indication of the depth of penetration of the particles; thus it is an indication of whether particles can penetrate deep enough to produce the ionization at altitudes where radar aurora is observed. Furthermore, the deeper the penetration, the lower the altitude where ionization is produced, and the greater the Hall conductivity and the normal magnetic-field-independent conductivity. As a result, the total, local ionospheric conductivity becomes much greater, so that magnetic field convection in these regions will be suppressed.

Conductivity is greater for large particle fluxes coupled with deeper penetration; this may mean that high conductivity is nearly correlated with higher energy fluxes. We suspect, then, that the energy-flux peaks in the satellite-pass profiles would correlate best with magnetometer data that record location and intensity of the auroral electrojet.

Past correlation work between location of visual and radar echoes[2] has shown that radar echoes are often adjacent to but not superposed upon visual arcs. This suggests that electric fields are lower inside the arcs because the high conductivity of the arc short-circuits the E-field. Barium-cloud releases[10] as well as the satellite-measured electric field[11] also suggest higher electric fields near to but not inside visual arcs. Thus, a correlation between energy flux and radar echoes is a proper correlation to study. Our results indicate no discernible trend, though there may be a slight tendency to be anti-coincident. The data of Figures 6.6 and 6.7 show that on the average the precipitation-energy flux is lower in regions that give rise to radar echoes than in other precipitation regions.

A radar/particle-flux precipitation correlation is meaningful in that we need a source for the ionospheric electron density. Our

work has indicated that widespread particle precipitation as measured by the Lockheed satellite is adequate to produce the needed ionospheric electron densities.

Some aspects of the data presented in this report have not been studied in depth. It would be important, we believe, to digitize the radar auroral echoes and compare absolute echo amplitude with precipitation characteristics. Our estimates of particle-stopping altitudes and resulting ionospheric electron densities, derived from work by Rees[6,7] and Chamberlain,[9] need to be altered to agree with spectral distributions that are appropriate for the actual satellite-measured precipitation. Data that were recorded by Lockheed but not made available to us concern the shape of the electron spectrum. That spectrum is sampled on-board the satellite at five energies. The data made available to us concerned only the absolute flux and the mean energy. Energy-distribution details would be of considerable value.

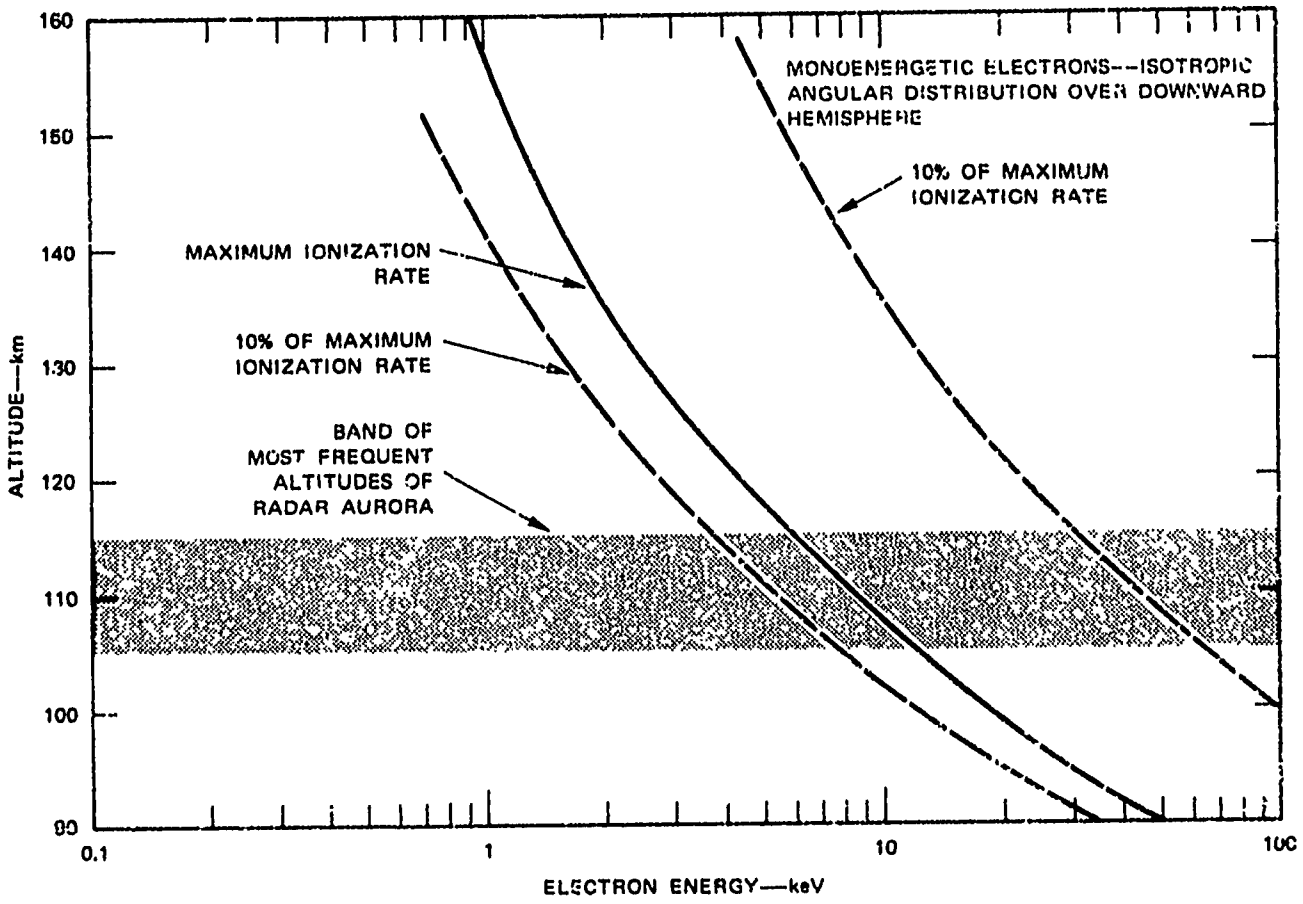

FIGURE 6.1 ALTITUDE OF THE MAXIMUM RATE OF PRODUCTION OF IONIZATION versus MONOENERGETIC ELECTRON ENERGY FOR MONOENERGETIC ELECTRON SPECTRUM. Isotropic angular distribution over downward hemisphere.

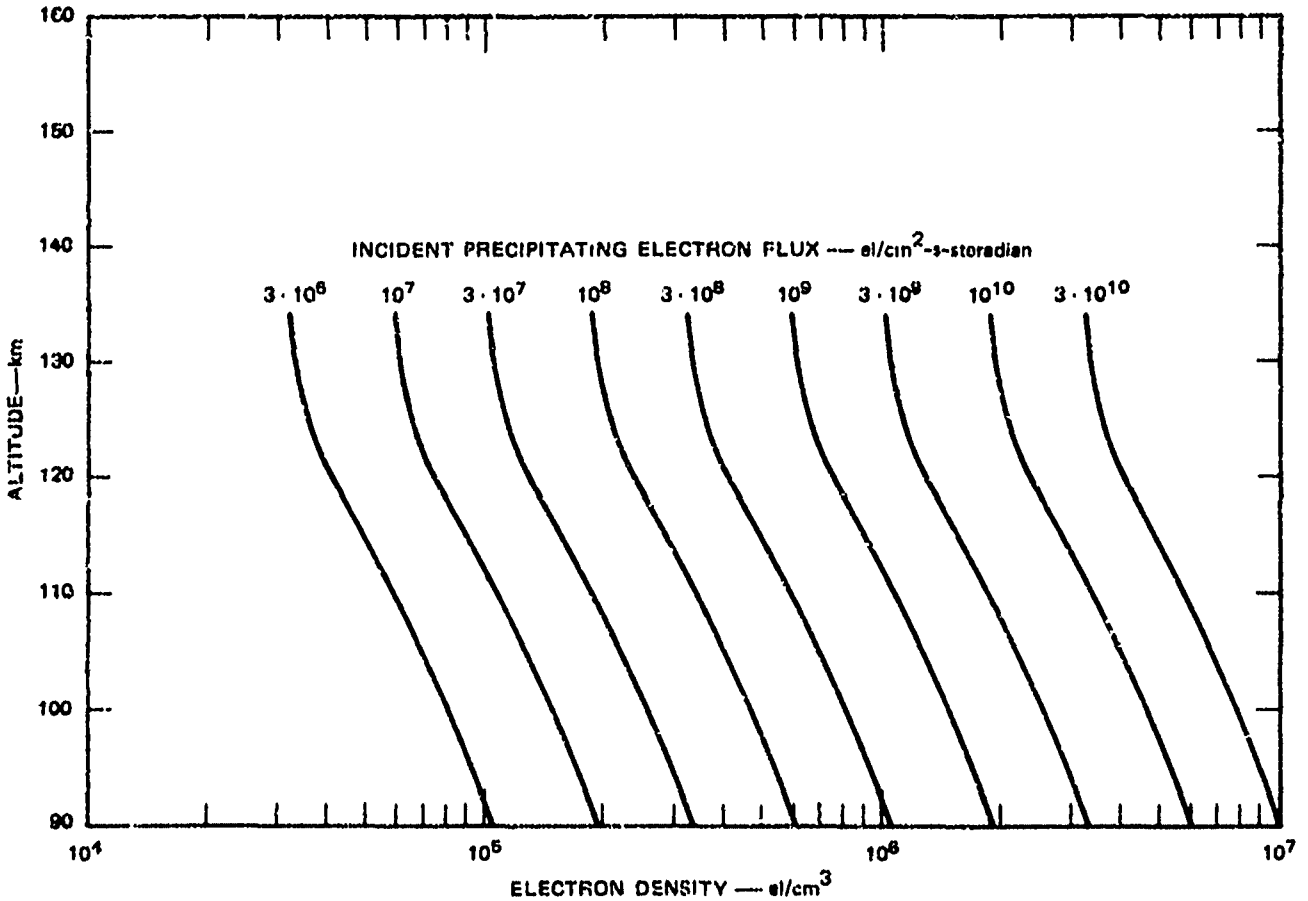

FIGURE 6.2 ALTITUDE versus ELECTRON DENSITY FOR VARIOUS MONOENERGETIC ELECTRON FLUXES. Electron density is at altitude of peak ionization rate.

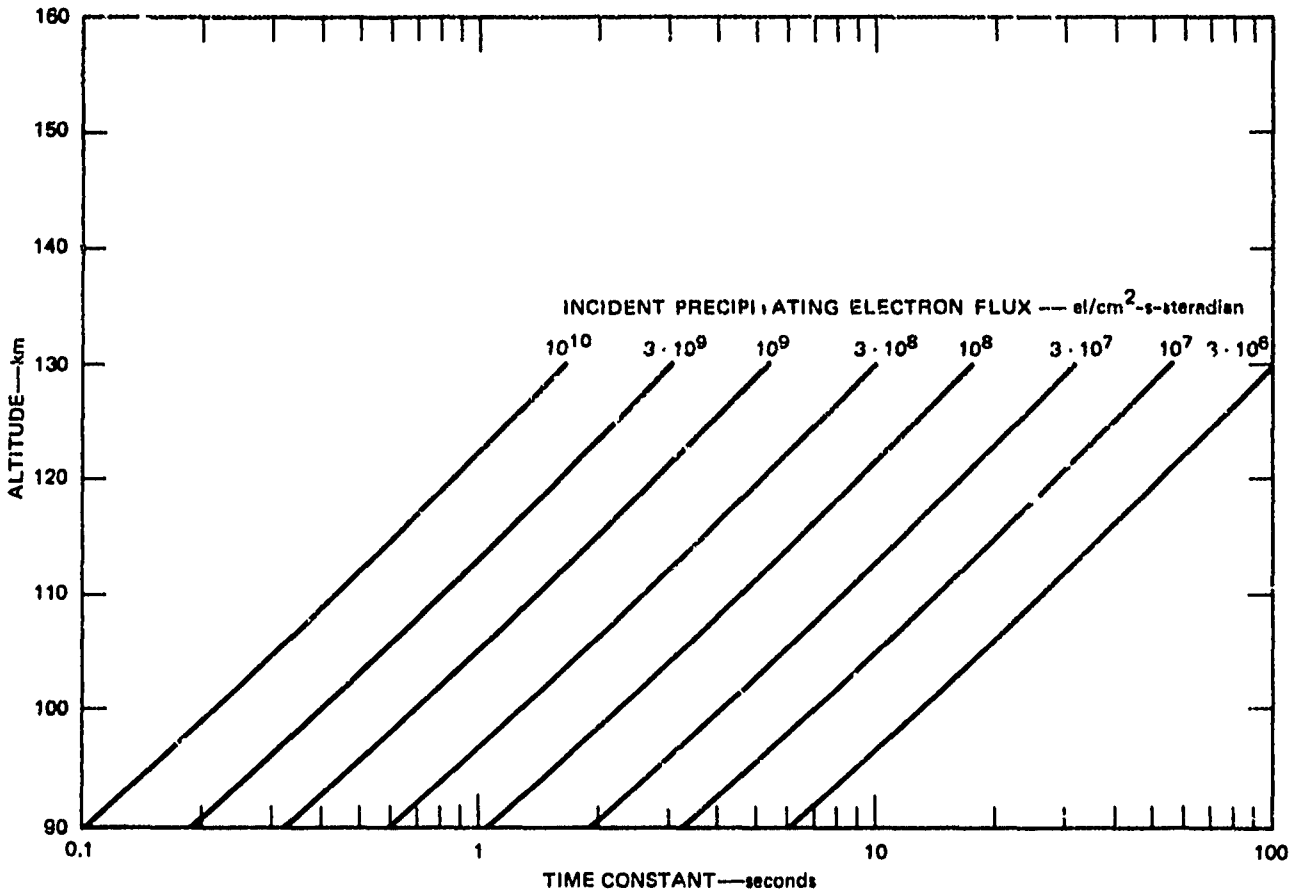

FIGURE 6.3 ALTITUDE versus CHEMICAL TIME CONSTANT FOR MONOENERGETIC ELECTRON FLUXES. Time constant is appropriate to altitude of peak ionization for monoenergetic electrons.

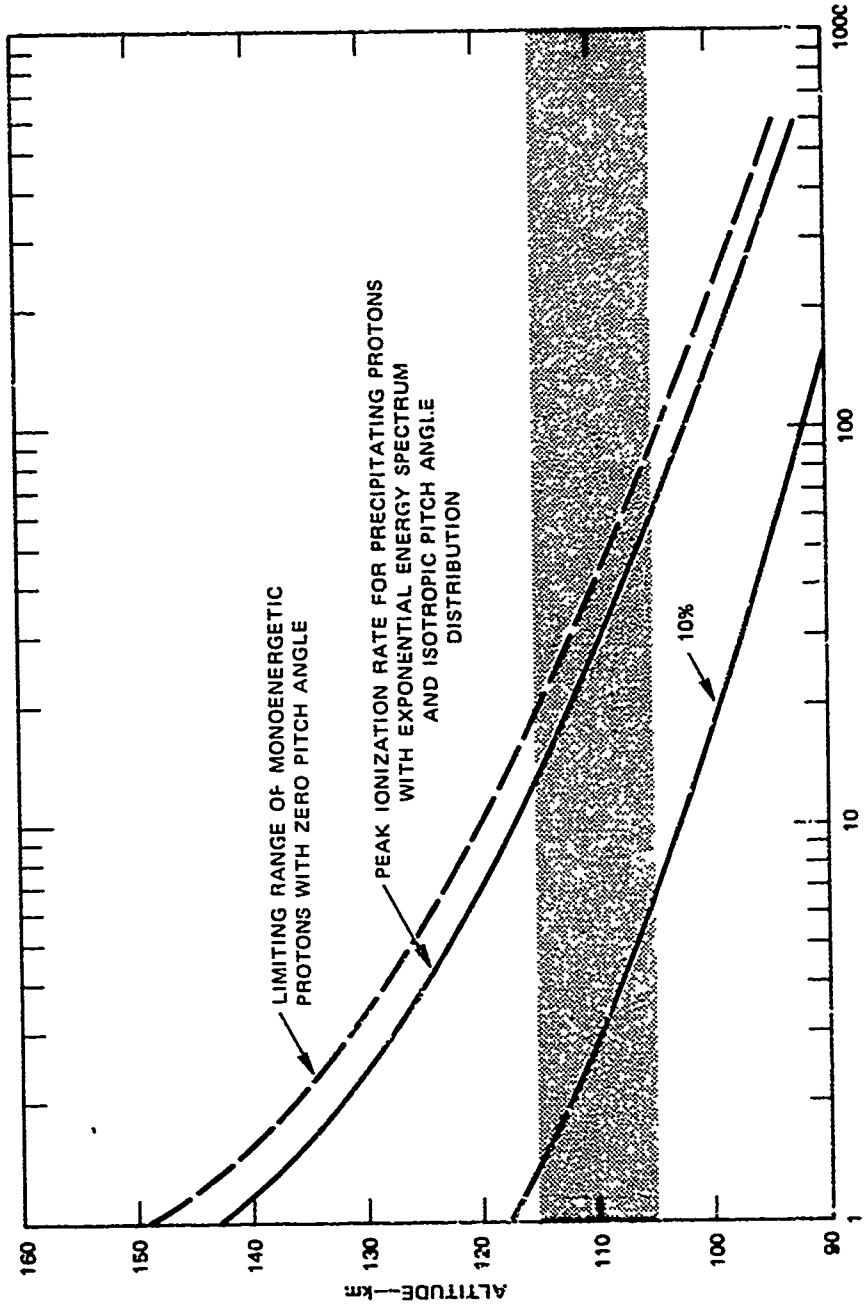

FIGURE 6.4 ALTITUDE OF MAXIMUM RATE OF PRODUCTION OF IONIZATION versus MEAN PROTON ENERGY FOR AN EXPONENTIAL PROTON SPECTRUM, ISOTROPIC ANGULAR DISTRIBUTION OVER DOWNWARD HEMISPHERE

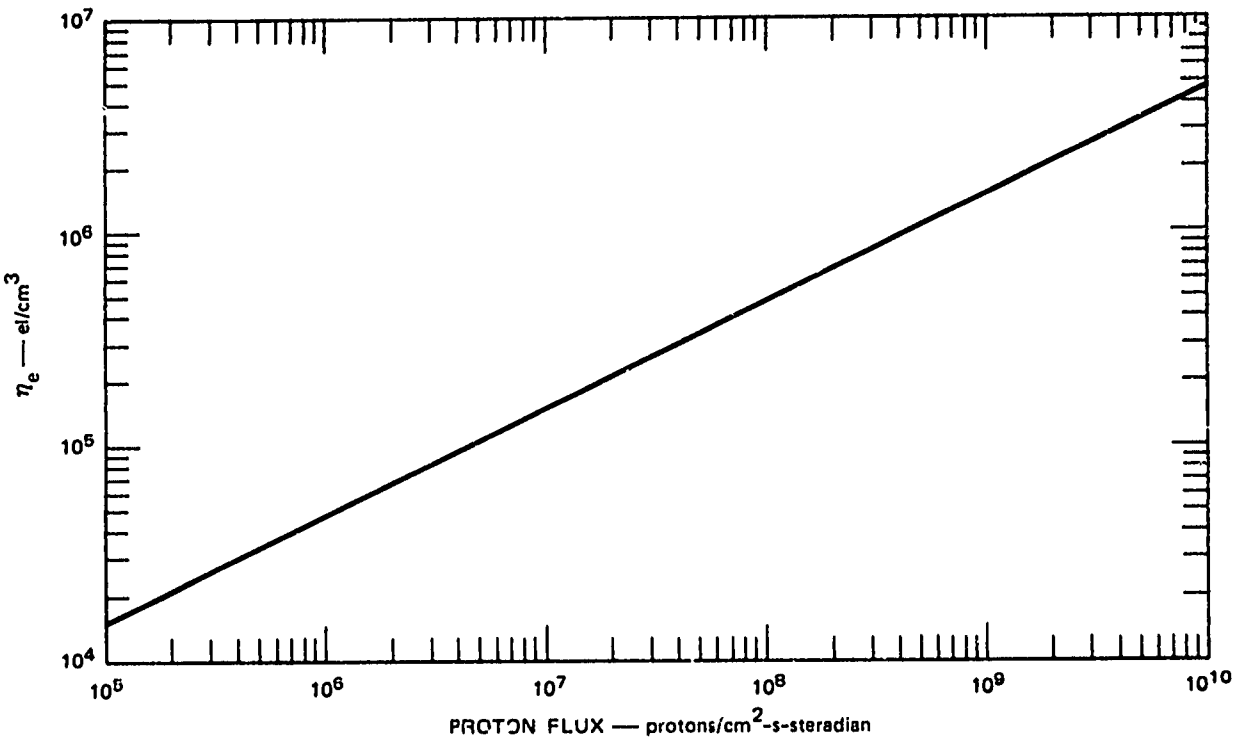

FIGURE 6.5 ELECTRON DENSITY AT 109 km ALTITUDE versus PROTON FLUX. Proton spectrum — exponential with $\bar{E}$ = 32 keV. Pitch-angle distribution is isotropic over downward hemisphere.

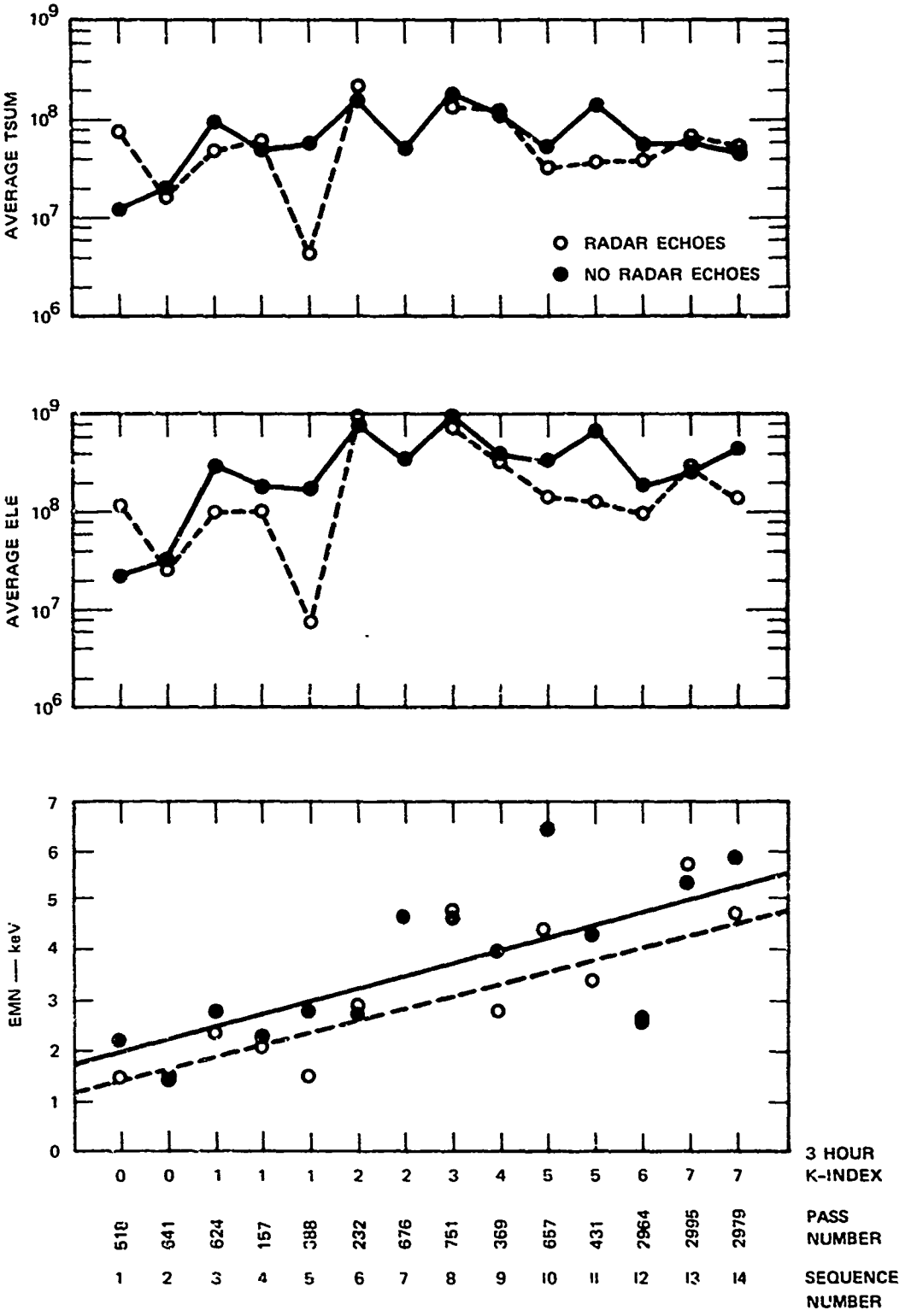

FIGURE 6.6 AVERAGE PROPERTIES OF PRECIPITATING ELECTRONS versus SATELLITE PASS SEQUENCE NUMBER ARRANGED ACCORDING TO ASCENDING THREE-HOUR MAGNETIC K-INDEX

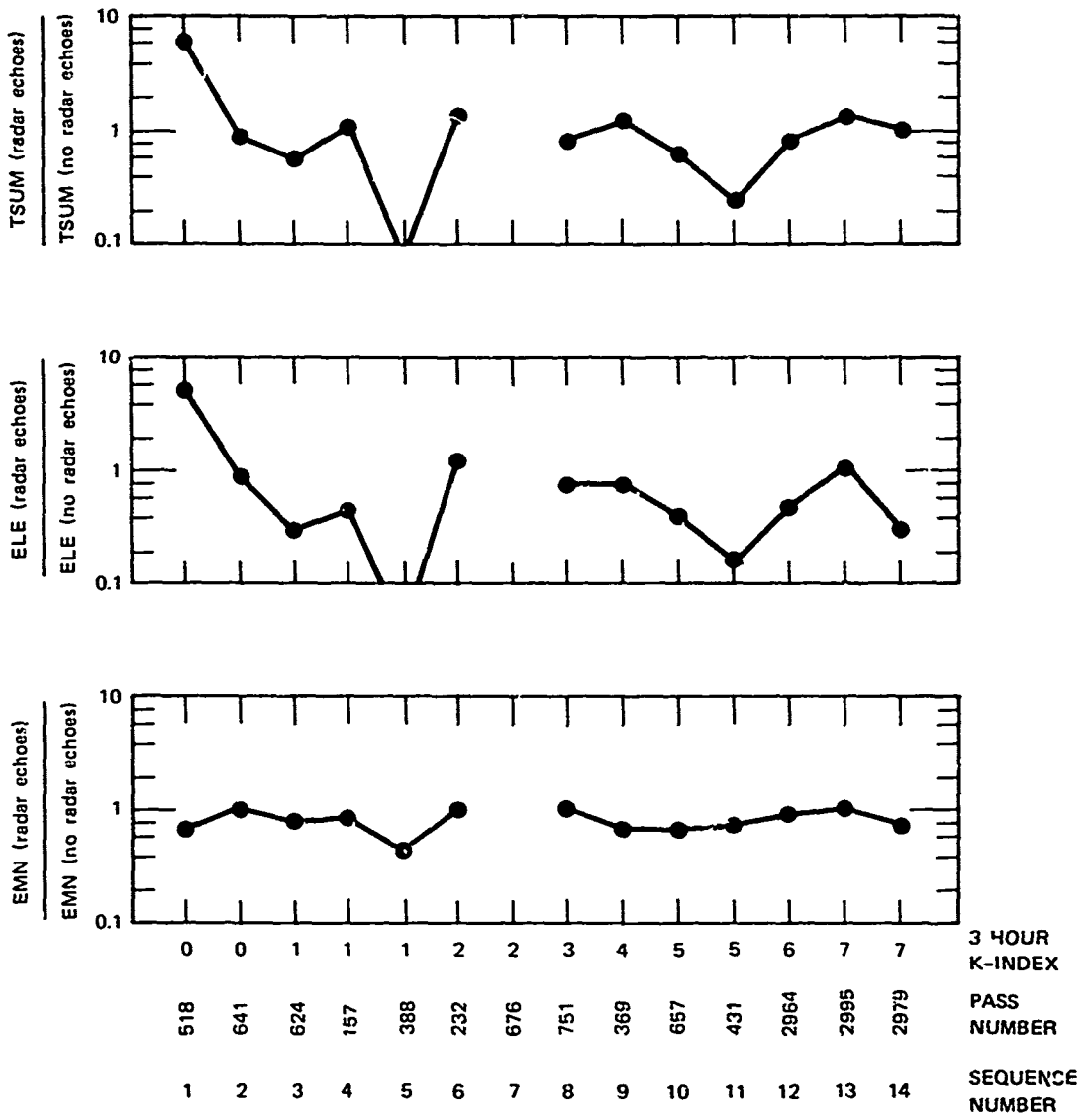

FIGURE 6.7 RATIO OF THE AVERAGE PROPERTIES OF PRECIPITATING ELECTRONS IN REGIONS WHERE RADAR AURORA WAS OBSERVED, TO THOSE PROPERTIES IN REGIONS WHERE NO RADAR AURORA WAS OBSERVED, versus SATELLITE-PASS SEQUENCE NUMBER ARRANGED ACCORDING TO ASCENDING THREE-HOUR MAGNETIC K-INDEX

7. CONCLUSIONS

This section summarizes what this research effort has revealed.

Comparison of the location of peak precipitation energy and number density of electrons as given in Figures 4.C.1 through 4.C.14, with similar quantities for protons in Figures 4.D.1 through 4.D.14 shows that, with the exception of Passes A2964, A2995, and A2979, protons precipitate to the south of electrons. This was the case for the eleven passes at lower K indices without exception. For the three passes that took place during high magnetic activity, the satellite precipitation data were not provided far enough south to verify that this behavior was also present during these three passes.

The data on these 14 satellite passes indicate that the electron density in the nighttime E-region that is necessary for radar scattering is probably produced by electron precipitation.

With the exception of the three passes that took place during very intense magnetic activity, radar aurora was never observed to be collocated with regions of peak proton-number flux or proton-energy-flux precipitation. On the three passes that took place during high magnetic activity, as we indicated above, satellite data at more southerly latitudes were not available, so that it is not known whether the proton data that were obtained for these three passes contain the most significant proton precipitation. Thus, it cannot be said with certainty that the coincidences between proton precipitation and radar aurora on these three passes contradicts the conclusions that have been drawn from the eleven other passes. We believe that this anticorrelation between proton precipitation and radar aurora is significant.

Attempts to find some deterministic relationship between the detailed characteristics of the precipitating electrons and the regions from which radar aurora is present have not produced any unique relationship. There appear to be some statistical trends, though these are subtle. These trends are as follows:

(1) There may be a tendency for regions of locally more intense electron-energy flux to anticorrelate with radar aurora, though this is not an absolute tendency.

(2) There may be a slight tendency for the average particle number flux--TSUM--to be less in regions of radar scattering than in other regions where measurable electron precipitation is taking place.

(3) There is a high statistical likelihood that the average electron precipitation energy flux (ELE) is less in regions from which radar echoes are obtained.

(4) The average energy of the precipitating electron is, on the average, less in regions of radar aurora.

8. SUGGESTIONS FOR FURTHER WORK

Radar data for 54 additional satellite passes have been reduced at SRI. Comparative studies must await delivery of Lockheed particle data which appears unlikely to occur due to Lockheed funding limitations.* Comparison between these additional 54 satellite passes would certainly be helpful in understanding aurora phenomena, in that the statistics of the phenomena will be greatly improved. Data from input-output experiments are still very rare.

The fourteen satellite passes that have been reduced have not been as thoroughly analyzed as is possible. The radar data that are presented in this report were reduced for the time period corresponding to the predicted satellite ephemeris data. As a result, the simultaneity of the radar data that we have analyzed, and the satellite pass data, is in some cases very poor. This lack of good simultaneity can be corrected for much of the data.

Many data correlations involving radar auroral locations, radar auroral signal strength, precipitation-particle energies, particle fluxes, etc., that could be performed have not received attention. In order to do an adequate job on future correlations, the radar data must be digitized and then recompared with the digitized satellite data. We believe such a rerun and a second analysis is more important than would be additional work on the 54 satellite passes for which Lockheed has not supplied us with precipitation data. For our comparison work, the data that

*In order to obtain the Lockheed data for 14 passes analyzed here it was necessary for SRI to fund Lockheed directly.

Lockheed delivers to us in the future should give, if possible, the individual electron channeltron counter rates rather than the summary value EMN. This would help us more accurately determine from the satellite data the altitudes at which the electron-precipitation energy is converted to ambient E-region ionization. For our comparison work we need to extend the work of Rees[6,7] and Chamberlain[9] to better meet the needs of this program. In particular, we need to compute deposition for particle spectra and pitch-angle distributions that are more like those that the satellites actually measure. Furthermore, we must look into the effects of proton-charge-exchange scattering in order to do a better job of making spatial comparisons between aurora and proton precipitation.

REFERENCES

1. R. L. Leadabrand and J. C. Hodges, "Correlation of Radar Echoes From the Aurora with Satellite-Measures Auroral Particle Precipitation," J. Geophys. Res., Vol. 72, No. 21, pp. 5311-5317 (1 November 1967).

2. W. G. Chesnut, J. C. Hodges, and R. L. Leadabrand, "Auroral Backscatter Wavelength Dependence Studies," Final Report, Contract AF 30 (602)-3734, SRI Project 5535, Stanford Research Institute, Menlo Park, California (June 1968).

3. T. Hagfors, R. G. Johnson, and R. A. Powers, "Simultaneous Observation of Proton Precipitation and Auroral Radar Echoes," J. Geophys. Res., Vol. 76, No. 25, pp. 6093-6098 (1 September 1971).

4. J. E. Evans and R. G. Johnson, "Auroral Input-Output Measurements," Contract Nonr-3398(00), Task No. NR 087-135, Lockheed Missiles and Space Company, Palo Alto, California.

5. G. B. Shook, "A Coordinated Experiment on Radar Clutter and Auroral Particle Fluxes," Final Report, Space Sciences Laboratory, Contract N00014-69-C-0207, Task No. NR 087-170, Lockheed Missiles and Space Company, Palo Alto, California (30 April 1970).

6. M. Rees, "Note on the Penetration of Energetic Electrons into the Earth's Atmosphere," Planet Space Sci., Vol. 12, pp. 722-725 (1964).

7. M. Rees "Auroral Ionization and Excitation by Incident Energetic Electrons," Planet Space Sci., Vol. 11, pp. 1209-1218 (1963).

8. I. G. Poppoff and R. C. Whitten, DASA Reaction Rate Handbook, Chapt. 8, "Reaction Rate Data From Atmospheric Measurements," DASA-1948 (October 1967).

9. J. W. Chamberlain, Physics of the Aurora and Airglow (Academic Press, New York, N. Y., 1961).

10. E. M. Wescott, J. D. Stolarik, and J. P. Heppner, "Electric Fields in the Vicinity of Auroral Forms from Motions of Barium Vapor Releases," J. Geophys. Res., Vol. 74, No. 14, pp. 3469-3487 (July 1, 1969).

11. T. L. Aggson, "Probe Measurement of Electric Fields in Space," in Atmospheric Emissions, B. M. McCormac and A. Omholt, Eds., p. 305 (Van Nostrand Reinhold Co., New York, N.Y., 1969).